

REVIEWS OF TOPICAL PROBLEMS

PACS numbers: **52.35.–g**, **96.60.–j**, 97.10.Sj

Coronal magnetic loops

V V Zaitsev, A V Stepanov

DOI: 10.1070/PU2008v051n11ABEH006657

Contents

Abstract. The goal of this review is to outline some new ideas in the physics of coronal magnetic loops, the fundamental structural elements of the atmospheres of the Sun and flaring stars, which are involved in phenomena such as stellar coronal heating, flare energy release, charged particle acceleration, and the modulation of optical, radio, and X-ray emissions. The Alfvén – Carlqvist view of a coronal loop as an equivalent electric circuit allows a good physical understanding of loop processes. Describing coronal loops as MHD-resonators explains various ways in which flaring emissions from the Sun and stars are modulated, whereas modeling them by magnetic mirror traps allows one to describe the dynamics and emission of high-energy particles. Based on these approaches, loop plasma and fast particle parameters are obtained and models for flare energy release and stellar corona heating are developed.

V V Zaitsev Institute of Applied Physics, Russian Academy of Sciences
ul. Ul'yanova 46, Nizhny Novgorod, Russian Federation
Tel. (7-831) 416 06 59. Fax (7-831) 436 06 16
E-mail: za130@appl.sci-nnov.ru
A V Stepanov Central Astronomical Observatory at Pulkovo, Russian Academy of Sciences
Pulkovskoe shosse 65/1, 196140 St.-Petersburg, Russian Federation
Tel. (7-812) 723 44 00. Fax (7-812) 388 22 44
E-mail: stepanov@gao.spb.ru

Received 16 May 2008, revised 28 June 2008
Uspekhi Fizicheskikh Nauk **178** (11) 1165 – 1204 (2008)
DOI: 10.3367/UFNr.0178.200811b.1165
Translated by S D Danilov; edited by A Radzig

1. Introduction

1.1 Magnetic loops as a fundamental structure of solar and stellar atmospheres

Magnetic loops (arches) constitute the basic structural elements of the coronae of the Sun and late type stars [1 – 3]. They play an important role in solar activity. Observation results from the space missions Skylab, SOHO (Solar and Helispheric Observatory), Yohkoh, RHESSI (Reuven Ramaty High Energy Solar Spectroscopic Imager), TRACE (Transition Region and Coronal Explorer), and Hinode, as well as large optical telescopes (SVTT — Surface Vessel Torpedo Tube), and the radio telescopes VLA (Very Large Array), SSRT (Siberian Solar Radio Telescope), and NoRH (Nobeyama Radioheliograph) have shown that solar flares arise in coronal loops [4, 5]. Eruptive prominences and coronal transients — giant coronal mass ejections (CMEs) — frequently have a loop shape, too [6]. The flaring activity of red dwarfs and close binary systems is also spawned by energy release in magnetic loops [1, 7, 8]. In addition, the loops exemplify a typical magnetic structure encountered in atmospheres of accretion disks and young stellar objects [9, 10]. Progress in the physics of coronal loops to a large degree rests on the following ideas:

I. A coronal loop is an equivalent electric (*RLC*) circuit:

II. A coronal loop is a resonator for magnetohydrodynamic (MHD) oscillations.

III. A coronal loop is a magnetic trap for high-energy charged particles.

1.2 Observational data, types of magnetic loops, and their parameters

The corona of the Sun (a main sequence star G2) in its active phase consists predominantly of hot, dense magnetic loops shining in soft X-rays and making up an essential part of the total corona mass. The magnetic loops point to a complex character of the subphotospheric magnetic field, which is most likely linked to convective motions of the photospheric matter.

Observations suggest that there are five morphologically distinct types of loops in the solar atmosphere [11].

1. *Loops connecting different active regions*. Their length reaches 700,000 km, the plasma temperature in such loops runs to $(2-3)\times10^6$ K, and the density is about 10^9 cm^{-3}. Loop footpoints are located at islands of a strong magnetic field on the periphery of active regions. The characteristic existence time of such loops is about one day.

2. *Loops in quiet regions*. They connect active regions and have the same length as in the previous case, but their temperature is somewhat lower, ranging $(1.5-2.1)\times10^6$ K, while the density lies in the range $(2-10)\times10^8$ cm^{-3}.

3. *Loops of active regions*. Their lengths span 10,000–100,000 km, their temperature and density are in the ranges $10^4-2.5\times10^6$ K and $(0.5-5.0)\times10^9$ cm^{-3}, respectively.

4. *Post-flare loops*. They commonly connect footpoints of two-ribbon flares, and have a length of 10,000–100,000 km, temperature of $10^4-4\times10^6$ K, and density up to 10^{11} cm^{-3}.

5. *Single flare loops*. These are separate loops in which flare energy is released. Bursts of hard X-ray emission lasting about one minute are the most pertinent feature of such flares. In soft X-rays, these loops are characterized by small volumes and low heights. The loops are 5000–50,000 km in length, their temperature is less than 4×10^7 K, and their plasma density reaches 10^{12} cm^{-3}.

Closed magnetic structures resembling coronal loops exist on stars of other types as well. Data collected with the satellites Einstein, RoSAT (from German Röntgensatellit), and XMM-Newton (XMM stands for X-ray Multi-Mirror Mission) [12–14] indicate that practically all stars on the Hertzsprung–Russell diagram possess hot coronae with temperatures in the range of 10^7-10^8 K. They are not confined gravitationally, hence the existence of a magnetic field confining them is implied. Of special interest are the stars of late spectral classes, in particular dMe-stars — red dwarfs exhibiting a high flare activity and representing nearly 80% of stars in the Galaxy and its close neighborhood. Despite the morphological similarity between emissions of the Sun and red dwarfs, specifically in the radio band (the presence of a slowly varying component, rapidly drifting bursts, sudden reductions, spike bursts, and quasiperiodic pulsations [7, 15, 16]), there exist a number of essential differences stemming from the high activity of the coronae of these stars.

First, mention should be made of a high brightness temperature of 'quiet' radio emission of dMe-stars (up to 10^{10} K), which cannot be furnished by a thermal coronal plasma with temperatures ranging 10^7-10^8 K. This component is commonly interpreted as gyro-synchrotron emission of nonthermal electrons present in coronae of red dwarfs, together with a hot plasma. The coexistence of the hot plasma and subrelativistic particles is also suggested by the correlation between radio and soft X-ray emissions over six orders of magnitude in intensity [17]. This phenomenon is absent in the solar corona. In a quiet state, it does not host a sufficient amount of high-energy particles and the brightness temperature of solar radio emission does not exceed 10^6 K.

Second, the difference lies in the extremely high brightness temperature of flare radio emissions of red dwarfs, sometimes in excess of 10^{16} K, which is 3–4 orders of magnitude higher than that of the most powerful radio bursts on the Sun. This hints at the presence of effective maser (coherent) mechanisms of emission from stellar coronae. Moreover, radio flares on red dwarfs can rather frequently arise independently of optical flares.

Third, the sizes of loops on the Sun and red dwarfs are different [1, 3]. The length of loops on the Sun, excluding the transequatorial ones, is as a rule much smaller than the solar radius (Fig. 1a). On red dwarfs, the size of magnetic loops can be comparable to stellar radii or can even exceed them by several times (Fig. 1b). The magnetic field intensity in stellar loops can be in excess of that in solar loops by an order of magnitude.

Table 1 presents parameters of flare loops on the Sun and late type stars (from published sources), which were obtained on the basis of multiband observations (encompassing optical, radio, and X-ray ranges) and methods of diagnostics relying on approaches I–III mentioned above.

This review describes electrodynamic processes in coronal magnetic loops, mostly flare loops, invoking magnetohydrodynamic and kinetic approaches and analogies with an electric circuit.

2. The coronal loop as an equivalent electric (*RLC*) circuit

A well-developed solar flare has a complex magnetic configuration consisting of a bundle of loops. Nevertheless, it rather often happens that flares are observed in single loops located relatively far from sunspots [5]. Let us consider electrodynamic processes taking place in a single loop flare. This is important for both interpreting single loops and understanding processes active in flares with a more complex magnetic structure.

Questions pertaining to the generation of electric current and the formation of magnetic loops in a weakly ionized plasma of the solar photosphere are considered in Refs [18–22]. Questions on the interaction of flare loops are illuminated in the reviews by Priest [23] and Sakai and de Jager [5], as well as in works by Khodachenko and Zaitsev [24, 25].

2.1 A physical model of the single flare loop

Microwave and X-ray emissions from single flare loops indicate that the acceleration of charged particles and plasma heating take place inside the loops. The source of free energy for the acceleration and heating is the nonpotential part of the

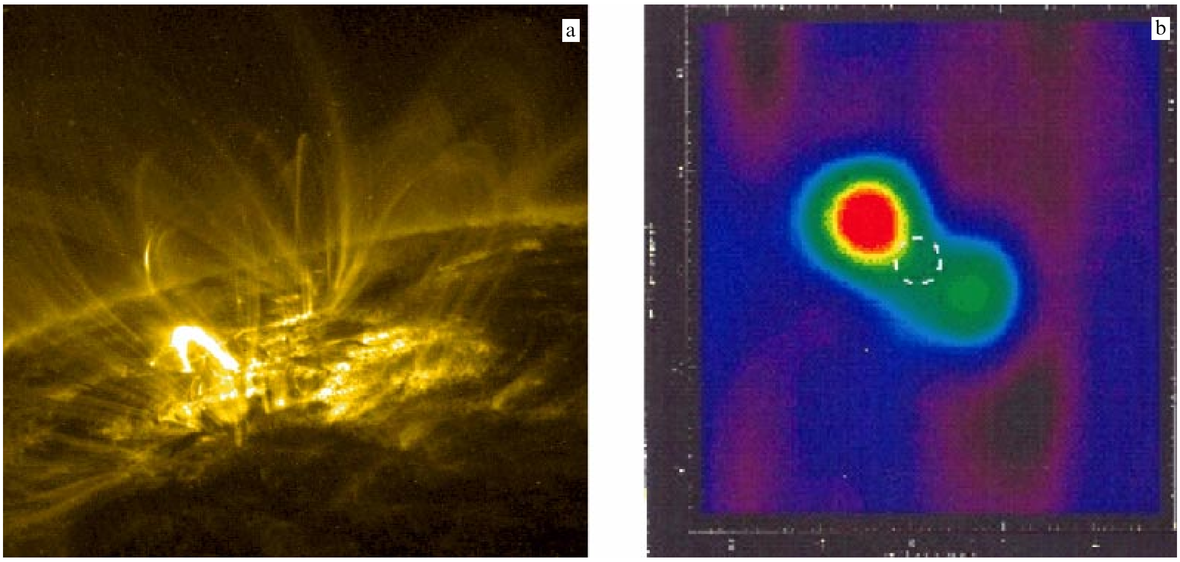

Figure 1. (a) Coronal magnetic loops of an active region on the Sun observed with the space laboratory TRACE in the ultraviolet range ($\lambda = 171$ Å) [2]. A hot flare loop stands out sharply. (b) Radio map of the star UV Ceti B on a wavelength of 3.6 cm based on data obtained with VLBA (Very Long Baseline Array) and VLA (Very Large Array). The dashed line marks the optical disk of the star [3].

Table 1. Parameters of coronal flare loops.

Parameter	Sun	Red dwarf UV Ceti	Close binary stars	
			RS CVn	Algol
Length, cm	$(1-10)\times10^9$	$2\times10^9-3\times10^{11}$	$(5-10)\times10^{10}$	$(2-6)\times10^{11}$
Lateral size, cm	$(1-5)\times10^8$	$10^8-3\times10^9$		
Plasma density n, cm^{-3}	10^9-10^{12}	$10^{10}-10^{12}$	10^8-10^{12}	10^9-10^{12}
Plasma temperature T, K	10^6-10^7	$3\times10^6-10^8$	$(3-9)\times10^7$	$(3-7)\times10^7$
Magnetic field induction B, G	10^2-10^3	$3\times10^2-10^3$	$(0.3-6)\times10^2$	$(1-5)\times10^2$
Emission measure (EM), cm^{-3}	$10^{47}-10^{50}$	$10^{50}-10^{53}$	$10^{53}-10^{55}$	$10^{52}-10^{54}$

magnetic field related to intense electric currents flowing within the magnetic loop, which are generated at loop footpoints by the convective motions of the photospheric plasma. This idea, rooted in works by Alfvén and Carlquist [26] and Sen and White [27], is illustrated in Fig. 2 displaying a magnetic loop. Its footpoints, immersed in the photosphere, are formed by horizontally converging streams of photospheric matter. Such a configuration can be realized, for instance, when loop footpoints are located at nodes of several supergranulation cells. The existence of strong electric currents in coronal loops is indirectly supported by the observations made by Klimchuk et al. [28] and TRACE data which point to a practically invariable loop cross section along the whole loop length, which would hardly be possible for a potential magnetic field. We will distinguish three important regions in the magnetic structure presented in Fig. 2.

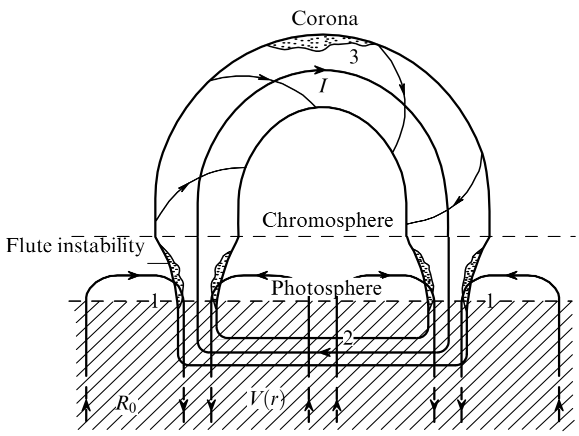

Figure 2. Schematic of a coronal magnetic loop formed by converging convective fluxes of photospheric plasma.

Region 1 is located in the photosphere and occupies the place where the magnetic field and the electric current matched to it are generated. In this region, $\omega_e/\nu_{ea} \gg 1$ and $\omega_i/\nu_{ia} \ll 1$, where ω_e and ω_i are the gyrofrequencies of electrons and ions, and ν_{ea} and ν_{ia} are the frequencies of electron–atom and ion–atom collisions, respectively. Thus, the electrons are magnetized, and the ions are dragged by a neutral plasma component, which leads to generating a radial electric field E_r of charge separation [27]. The electric field E_r, together with the initial magnetic field B_z, generate a Hall current j_φ strengthening the initial magnetic field B_z [21, 22]. Strengthening of the magnetic field proceeds until the 'raking up' of the background magnetic field is compensated by magnetic field diffusion due to the anisotropic conductivity of the plasma. As a result, a stationary magnetic flux tube forms. The magnetic field inside it is determined by total energy input from the convective plasma flux in a time of the tube formation (estimated as R_0/V_r, where $R_0 \sim 30{,}000$ km is the spatial scale of the supergranulation cell, and $V_r \sim 0.1-0.5$ km s^{-1} is the horizontal velocity of convective motion). The energy density of the magnetic field inside the tube can substantially exceed the kinetic energy density of convective motion. In the stationary state, the radial gradient of the magnetic field and magnetic tension within the tube are balanced by the gradient of gas-kinetic pressure, while the kinetic energy of convective flux is spent to sustain the radial electric field E_r of charge separation and the Hall current j_φ.

Region 2 is located in the lower photosphere or directly below the photosphere. It is assumed that in this region the electric current I passing through the magnetic loop gets closed. The distribution of electric currents in the photosphere, found on the basis of magnetic field measurements [29, 30], gives evidence in favor of the existence of non-compensated electric currents [31 – 33]. From these data it follows that the electric current in the magnetic flux tube flows through the coronal part of the loop from one footpoint to the other one with no manifestations of a reverse current. The current gets closed in the region below the photosphere, where plasma conductivity becomes isotropic and the current follows the shortest path connecting the loop footpoints. For a magnetic field $B = 1000$ G in a tube and temperature $T = 5\times10^3$ K, the conductivity is isotropic for plasma concentration $n = 5\times10^{16}$ cm^{-3}, which approximately corresponds to the level $\tau_{5000} = 1$ (optical thickness of radiation at the wavelength $\lambda = 5000$ Å) to which the base of the solar photosphere is referenced. Calculations done in Refs [21, 22] demonstrate that for convective motion velocity $V_r = 0.1$ km s^{-1} the radius of the flux tube formed reaches $r \approx 3.3\times10^7$ cm at an altitude of 500 km above the level $\tau_{5000} = 1$, while the along-tube current is $I_z \approx 3\times10^{11}$ A for the magnetic field $B = 1000$ G on the loop axis.

Region 3 occupies the coronal part of the loop. The gas-kinetic pressure here is smaller than the magnetic field pressure (plasma parameter $\beta \ll 1$) and the structure of the loop is close to force-free, i.e., the lines of electric current are nearly aligned with magnetic field lines.

We note that according to Stenflo [34] the kinetic energy of rotational motion of a sunspot with velocity ~ 0.1 km s^{-1} can serve as the source of electromagnetic energy for the flare loop current. Such a situation is, in principle, plausible if footpoints of the flare loop are located within the spot area. For loops formed outside the spots, it is the photospheric convection which serves as the generator of electric current.

The above-considered magnetic loop with current may be conceived as an equivalent electric circuit. This idea was first formulated by Alfvén and Carlquist [26] for a circuit model of a flare. The model of Ref. [26] is based on the measurements made by Severny [35], who discovered electric currents $I \geqslant 10^{11}$ A in the vicinities of sunspots, and on the analogy with a circuit containing a mercury rectifier which can exhibit sharp transitions from a state with high conductivity to a state with high resistivity. The energy is explosively released when the current in the circuit is abruptly interrupted. Mechanisms underlying the current interruption can vary. One of them is related to developing the flute instability near the top or footpoints of the loop and switching on the Cowling conductivity [36]. The latter is linked to ion – atom collisions, and augments the electric resistance of the magnetic loop by 8 – 9 orders of magnitude [37, 38]. It is accompanied by effective plasma heating and acceleration of particles in the loop. These processes will be considered in detail in Sections 4 and 5.

2.2 Formation of magnetic flux tubes in nodes of supergranulation cells

Photospheric footpoints of coronal magnetic loops can be approximated by vertical magnetic flux tubes. We illustrate the possibility of their formation through 'raking' the background magnetic field by photospheric convection. For simplicity, consider the formation of an axisymmetric magnetic flux tube $\mathbf{B}(0, B_\varphi, B_z)$ with the current $\mathbf{j}(0, j_\varphi, j_z)$ in the case of stationary axisymmetric flux of photospheric matter with the velocity $\mathbf{V}(V_r, 0, V_z)$, $V_r < 0$. Here, r, φ, z are the coordinates of a cylindrical frame of reference with the vertical z-axis. Assume the magnetic flux tube to be located vertically at a node of several supergranules and the velocity of the converging convective stream to be much less than the speed of sound and the Alfvén and free fall velocities. In this case, the evolution of the magnetic field in the tube proceeds quasistationary, implying that the following system of equation can be used:

$$\rho\mathbf{g} - \nabla p + \frac{1}{c}\,\mathbf{j}\times\mathbf{B} = 0\,, \tag{2.1}$$

$$\operatorname{div}\rho\mathbf{V} = 0\,, \tag{2.2}$$

$$\mathbf{E} + \frac{1}{c}\,\mathbf{V}\times\mathbf{B} = \frac{j}{\sigma} + \frac{\mathbf{j}\times\mathbf{B}}{enc} - \frac{\nabla p_{\mathrm{e}}}{en} + \frac{F^2}{(2-F)\,c^2 n m_{\mathrm{i}} v'_{\mathrm{ia}}}\,[\mathbf{j}\times\mathbf{B}]\times\mathbf{B}\,, \tag{2.3}$$

$$\operatorname{rot}\mathbf{E} = \frac{1}{c}\,\frac{\partial\mathbf{B}}{\partial t}\,. \tag{2.4}$$

Here, $\rho = n_{\mathrm{a}}m_{\mathrm{a}} + n_{\mathrm{e}}m_{\mathrm{e}} + n_{\mathrm{i}}m_{\mathrm{i}}$ is the density of a partly ionized photospheric plasma, $p = p_{\mathrm{a}} + p_{\mathrm{e}} + p_{\mathrm{i}}$ is the pressure, $\mathbf{V} = (\sum_k n_k m_k \mathbf{V}_k)/(\sum_k n_k m_k)$ is the mean velocity of plasma motion, $k = \mathrm{a, i, e}$ (a stands for atoms, i for ions, and e for electrons), $\sigma = ne^2/[m_{\mathrm{e}}(v'_{\mathrm{ei}} + v'_{\mathrm{ea}})]$ is the Coulomb conductivity, $F = \rho_{\mathrm{a}}/\rho$ is the relative density of neutral particles, v_{kl} is the collision frequency between particles of sorts k and l, $v'_{kl} = [m_l/(m_k+m_l)]\,v_{kl}$ is the effective collision frequency, and $n_{\mathrm{i}} = n_{\mathrm{e}} = n$. The generalized Ohm's law (2.3) is written out with account for the quasistationary character of the process. Since the degree of ionization in region 1 in Fig. 2 (the height $h \leqslant 500$ km above the level $\tau_{5000} = 1$) is sufficiently small, one can further assume that $F \approx 1$, and $p \approx p_{\mathrm{a}}$. Projecting Eqn (2.3) on the φ- and z-axes and taking into account Eqn (2.4) and the relationships

$$j_\varphi = -\frac{c}{4\pi}\,\frac{\partial B_z}{\partial r}\,,\quad j_z = \frac{c}{4\pi}\,\frac{1}{r}\,\frac{\partial(rB_r)}{\partial r}\,, \tag{2.5}$$

we arrive at the equations describing the slow evolution of magnetic field components in a vertical magnetic flux tube [39]:

$$\frac{\partial B_z}{\partial t} = \frac{1}{r}\,\frac{\partial}{\partial r}\left\{r\left[\frac{c^2}{4\pi\sigma}\,(1+\alpha B_z^2)\,\frac{\partial B_z}{\partial r} + \frac{c^2}{4\pi\sigma}\,\alpha B_\varphi B_z\,\frac{1}{r}\,\frac{\partial(rB_\varphi)}{\partial r} - V_r B_z\right]\right\}, \tag{2.6}$$

$$\frac{\partial B_\varphi}{\partial t} = \frac{\partial}{\partial r}\left[\frac{c^2}{4\pi\sigma}\,(1+\alpha B_\varphi^2)\,\frac{1}{r}\,\frac{\partial(rB_\varphi)}{\partial r} + \frac{c^2}{4\pi\sigma}\,\alpha B_\varphi B_z\,\frac{\partial B_z}{\partial r} - V_r B_\varphi\right]. \qquad (2.7)$$

Here, $\alpha = \sigma F^2 [c^2 n m_\mathrm{i} v'_\mathrm{ia}(2-F)]^{-1}$. Notice that Eqns (2.6) and (2.7) incorporate anisotropic conductivity.

At the initial stage of magnetic flux tube evolution, the diffusion of a magnetic field due to conductivity can be neglected as it is small compared to the effect of field strengthening provided by the convective motion of the plasma. Assuming for simplicity $V_r = V_0 r/R_0$, where $V_0 < 0$ (converging flux), and R_0 is the scale at which the horizontal convection velocity varies, we obtain from Eqns (2.6) and (2.7) the following solution for the components of the magnetic field:

$$B_\varphi(r,t) = \exp\left(-\frac{V_0}{R_0}\,t\right) B_{\varphi 0}\left[r\exp\left(-\frac{V_0}{R_0}\,t\right)\right],$$
$$B_z(r,t) = \exp\left(-\frac{2V_0}{R_0}\,t\right) B_{z0}\left[r\exp\left(-\frac{V_0}{R_0}\,t\right)\right], \qquad (2.8)$$

where $B_{\varphi 0}(r)$ and $B_{z0}(r)$ are the magnetic field components at $t=0$. From expressions (2.8) it follows that the magnetic field grows near the magnetic flux tube axis $(r=0)$ on a characteristic time scale $t_0 = R_0/|V_0|$ comparable to the existence time of the supergranule.

The growth in the magnetic field intensity in the flux tube is accompanied by an increase in the importance of magnetic field diffusion. In a stationary flux tube, the strengthening of the field through raking by the convective flux is compensated by magnetic field diffusion attributed to conductivity. In this case, the magnetic field components are described by the following equations [21]:

$$\frac{\partial B_z}{\partial r} = \frac{4\pi\sigma V_r}{c^2}\,\frac{B_z}{1+\alpha(B_z^2+B_\varphi^2)},$$
$$\frac{1}{r}\,\frac{\partial(rB_\varphi)}{\partial r} = \frac{4\pi\sigma V_r}{c^2}\,\frac{B_\varphi}{1+\alpha(B_z^2+B_\varphi^2)}. \qquad (2.9)$$

To be specific, let the velocity of plasma convective motion be of the form

$$V_r(r) = \begin{cases} -\dfrac{V_0 r}{r_1}, \quad V_z(r) = V_{z0} = \mathrm{const} \quad \text{for} \quad r < r_1, \\[2ex] -\dfrac{V_0 r_1^2}{r^2}, \quad V_z(r) = \dfrac{\mathrm{const}}{r^3} \quad \text{for} \quad r > r_1 \end{cases}$$

in the vicinity of a magnetic flux tube. Here, r_1 is the radius of the magnetic flux tube, and the values of V_{z0} and the constants follow from the continuity equation under the assumption that density is an exponential function of z. System of equations (2.9) has the integral

$$rB_\varphi(r) = \mathrm{const}\,B_z(r). \qquad (2.10)$$

Moreover, the form of the system does not change on making substitutions

$$B_\varphi \to B'_\varphi = B_\varphi + \frac{\mathrm{const}_1}{r}, \quad B_z \to B'_z = B_z + B_0$$

in its right-hand sides because the left-hand sides of the equations are also invariant with respect to this substitution. As follows from Eqns (2.5), this substitution does not influence components of the electric current governing the structure of the magnetic field in the flux tube. In other words, this implies that the system of equations (2.9) defines the magnetic field in the loop up to some potential field. Accordingly, the general expression for the component B_φ can be written out as

$$B_\varphi = C_1\,\frac{B_z(r)}{r} + C_2\,\frac{1}{r}.$$

We select the constant C_2 so that for $r \to 0$ the field $B_\varphi(0)$ is finite. This is possible when $C_2 = -C_1 B_z(0)$. The constant C_1 is determined from the condition that at $r = r_1$ the components of the magnetic field are equal to $B_\varphi(r_1)$ and $B_z(r_1)$. The result is as follows:

$$B_\varphi(r) = b\,\frac{r_1}{r}\,\big(B_z(r) - B_z(0)\big), \quad b = \frac{B_\varphi(r_1)}{B_z(r_1) - B_z(0)}. \qquad (2.11)$$

An expression for $B_z(r)$ can readily be found from the first equation of system (2.9) in the approximation were $\alpha(B_z^2 + B_\varphi^2) \gg 1$, $B_z^2 \gg B_\varphi^2$:

$$B_z^2(r) = B_z^2(0) - \frac{4\pi\sigma V_0}{c^2 r_1 \alpha}\,r^2, \quad r \leqslant r_1,$$
$$B_z^2(r) = B_z^2(\infty) + \frac{8\pi\sigma V_0}{c^2 r\alpha}\,r_1^2, \quad r \geqslant r_1. \qquad (2.12)$$

The flux tube radius is expressed through boundary values of the magnetic field induction:

$$r_1 = \frac{\left[B_z^2(0) - B_z^2(\infty)\right] c^2\alpha}{12\pi V_0\sigma}. \qquad (2.13)$$

The radius r_1 grows with an increase in the magnetic field induction on the tube axis and with a decrease in the convection velocity. For the height $h \approx 500$ km above the level $\tau_{5000} = 1$, where $n \approx 10^{11}$ cm^{-3}, $n_\mathrm{a} \approx 10^{15}$ cm^{-3}, and $T \approx 10^4$ K, one obtains $r_1 \approx 2.7\times 10^7$ cm, assuming that $B_z(0) = 10^3$ G and that the convection velocity $V_0 = 0.1$ km s^{-1}.

2.3 Electric current in the magnetic flux tube

Equations (2.5) and (2.11) allow determining the total electric current I_z passing through the magnetic flux tube cross section parallel to its axis:

$$I_z = \int_0^\infty j_z\,2\pi r\,\mathrm{d}r = \frac{bcr_1}{2}\,\left[B_z(\infty) - B_z(0)\right], \qquad (2.14)$$

which depends on the magnitudes of the magnetic field on the tube axis and infinity, and also on the tube radius and the degree b of magnetic field twisting [see formulas (2.11)]. The current can be expressed in terms of plasma parameters and convection velocity by substituting expression (2.13) for the tube radius in Eqn (2.14):

$$I_z = -\frac{cbF^2\left[B_z(0) - B_z(\infty)\right]^2\left[B_z(0) + B_z(\infty)\right]}{24\pi(2-F)\,nm_\mathrm{i}v'_\mathrm{ia}V_0}. \qquad (2.15)$$

Assuming, for definiteness, $b \approx 1$, we estimate the longitudinal current as $I_z \approx 10^{11} - 10^{12}$ A for convection velocities $|V_0| = 0.1 - 1.0$ km s^{-1} and typical parameters of the photosphere at an altitude of 500 km above the level $\tau_{5000} = 1$, and prescribing $B_z(0) = 2 \times 10^3$ G for the magnetic field induction on the tube axis.

As is seen, the total electric current through the cross section of the magnetic flux tube is distinct from zero and can even be fairly high under coronal conditions. Solution of magnetohydrodynamical equations with due account for anisotropy of conductivity does not reveal a reverse current outside the magnetic flux tube. Indeed, as follows from formulas (2.5) and (2.11), the current through a cross section of radius r equals $I_z(r) = (bcr_1/2)/[B_z(r) - B_z(\infty)]$ and for $B_z(r)$ monotonically varying across the tube cross section the current direction does not change to the opposite one. This result is the consequence of the character of the electromotive force confined to photospheric footpoints of the magnetic flux tube and forming its structure. The electromotive force $(1/c)\,\mathbf{V}_r \times \mathbf{B}_\varphi$ creating the current j_z changes its sign neither in the tube cross section nor at the tube periphery. It is noteworthy that the tube magnetic field, as follows from expressions (2.11) and (2.12), penetrates over several radii r_1 outside the tube, which renders possible inductive interaction in an ensemble of magnetic loops. From the induction equation (2.6) it follows that the characteristic diffusion time of the magnetic field, with account for the Cowling conductivity, is expressed as

$$t_\text{d} \approx \frac{4\pi\sigma r_1^2}{c^2\,(1 + \alpha B^2)} .$$

Time interval t_d for coronal magnetic loops can fall in the range 0.05 – 500 s, i.e., it is approximately 8 – 10 orders of magnitude smaller than the time scale of diffusion solely related to the classical conductivity σ. This circumstance stems from the large magnitude of the parameter $\alpha B^2 \approx 10^8 - 10^{10}$ in the Cowling conductivity, the latter being linked to the presence in the corona of only a small number of neutral atoms (on the order of 10^{-5} in mass fraction with account for the incomplete ionization of helium). The short diffusion time enables participation of coronal magnetic loops in fast dynamic processes.

Kadomtsev [40] considered torsional oscillations of an ideally conducting cylinder in a uniform magnetic field B_z. In this case, the electromotive force originating from the bending of magnetic field lines and generating the current j_z is distributed over the whole cylinder volume. The condition $\operatorname{div}\mathbf{j} = 0$ of current continuity then demands that an oppositely directed current flow over the cylinder surface, so that the total current through the cylinder cross section equals zero. The case of coronal magnetic loops behaves differently and compensation for the current does not happen. Here, the electromotive force $(1/c)\,\mathbf{V} \times \mathbf{B}$ is 'pointwise'. It is confined to photospheric footpoints of the magnetic loop, and the condition $\operatorname{div}\mathbf{j} = 0$ of current continuity is realized through the current flowing from one leg of the magnetic loop to the other along the coronal part of the loop and closing in layers below the photosphere, where the conductivity is isotropic and the current between the two legs follows the shortest path.

2.4 Equivalent electric circuit. Eigenfrequency

In Section 2.3 it was shown that convective motion of photospheric matter leads to the generation of thin magnetic flux tubes $10^7 - 10^8$ cm in radius with an electric current of $10^{11} - 10^{12}$ A inside them. The current flows from one loop footpoint toward the other one through the coronal part and closes below the photosphere. The depth where this closing occurs has to be determined from the condition that the conductivity is isotropic. The electric current density in a plasma embedded in a magnetic field can be represented as

$$\mathbf{j} = \sigma\mathbf{E}_{\parallel} + \sigma_\text{P}\mathbf{E}_{\perp} + \frac{\sigma_\text{H}}{B}\,\mathbf{B} \times \mathbf{E}_{\perp} . \tag{2.16}$$

Here, σ is the conductivity in the absence of the magnetic field. The Pedersen conductivity is expressed in the form

$$\sigma_\text{P} = \sigma\,\frac{1 + F\omega_\text{e}\omega_\text{i}\tau_\text{e}\tau_\text{ia}}{1 + \omega_\text{e}^2\tau_\text{e}^2 + 2F^2\omega_\text{e}\omega_\text{i}\tau_\text{e}\tau_\text{ia} + (F^2\omega_\text{e}\omega_\text{i}\tau_\text{e}\tau_\text{ia})^2} , \tag{2.17}$$

whereas the Hall conductivity is given by

$$\sigma_\text{H} = \sigma_\text{P}\,\frac{\omega_\text{e}\tau_\text{e}}{1 + F^2\omega_\text{e}\omega_\text{i}\tau_\text{e}\tau_\text{ia}} , \tag{2.18}$$

where $\tau_\text{e} = (\nu'_\text{ea} + \nu'_\text{ei})^{-1}$, and $\tau_\text{ia} = \nu'^{-1}_\text{ia}$. In the coronal part of the loop, where $\omega_\text{e}\tau_\text{e} \gg 1$, $F \approx 0$, the condition $\sigma \gg \sigma_\text{H} \gg \sigma_\text{P}$ holds true, i.e., the conductivity is strongly anisotropic. The relationship between the current and the electric field has the form $\mathbf{j} = \sigma\mathbf{E}_{\parallel}$ and the dominant part of the current follows the magnetic field lines. Below the photosphere one lands in a different regime. Here, $\omega_\text{e}\tau_\text{e} \ll 1$, $F^2\omega_\text{e}\omega_\text{i}\tau_\text{e}\tau_\text{ia} \ll 1$, and conditions $\sigma \approx \sigma_\text{P}$, $\sigma_\text{H} \ll \sigma$ hold true. Thus, Ohm's law assumes the same form as in the absence of magnetic field: $\mathbf{j} = \sigma\mathbf{E}$, and the current starts flowing from one loop footpoint to the other one along the path with the smallest electrical resistance, and not along the magnetic flux tube, as happens in the corona and chromosphere. For a loop magnetic field of $\sim 10^3$ G in the photosphere, the isotropization of conductivity and current closure take place, according to the well-known model of the solar atmosphere, at a depth of about 75 km below the photosphere [41]. Thus, the supergranular convection generates magnetic loops, the footpoints of which do not penetrate deep into the layers below the photosphere. Correspondingly, the loop, together with the current channel below the photosphere, is similar to a turn with an electric current for which an equation of an equivalent electric circuit can be written down.

A phenomenological approach resting on the analogy between magnetic loops in solar and stellar atmospheres and an electric network and *RLC* circuit proved to be fairly fruitful for describing not only flare processes on the Sun and stars [26], but also the heating of stellar coronae, the electrodynamics of hot stars [42], and accretion disks of magnetic neutron stars [43]. Considering an electric analog of the coronal magnetic loop, Ionson [44] analyzed a case where the magnetic field of the loop is potential, being created by a generator of a static field located deep below the photosphere. Here, we are considering a magnetic loop carrying a current generated by photospheric convection. In this case, the loop magnetic field is essentially nonpotential. This results in the effective resistance and capacitance of the circuit being functions of the current amplitude through self-consistent values of ω_e and ω_i.

Slow variation of the current for a time interval much in excess of the period of circuit natural oscillations obeys the equation [45]

$$\frac{1}{c}\,\frac{\text{d}(LI)}{\text{d}t} + RI = \varXi , \tag{2.19}$$

where I is the total current passing through the loop cross section parallel to its axis, and

$$R(I) = \frac{l_1}{\pi r_1^2 \sigma_1} + \frac{l_2}{\pi r_2^2 \sigma_2} + \frac{l_3}{\pi r_3^2 \sigma_3} + \frac{3\xi l_1 F^2 I^2}{\pi r_1^2 (2-F)\, c^4 m_{\mathrm{i}} v'_{\mathrm{ia}}} \left[1 + \frac{c^2 r_1^2 B_z^2(0)}{4I^2}\right], \tag{2.20}$$

l_1, l_2, and l_3 are the respective lengths of the electric circuit segments in the regions of action of photospheric electromotive force (EMF), closing the current below the photosphere, and in the corona (see Fig. 2), r_1, r_2, and r_3 are the radii of current channels in the respective regions, σ_1, σ_2, and σ_3 are the related isotropic conductivities, and $\xi \approx 0.5$ is the form factor arising from integration over the loop volume. The EMF provided by the photospheric convection at a footpoint of the loop stays on the right-hand side of Eqn (2.19):

$$\Xi = \frac{l_1}{\pi c r_1^2} \int_0^{r_1} V_r B_\varphi 2\pi r \,\mathrm{d}r \approx \frac{|\bar{V}_r| I l_1}{c^2 r_1}, \tag{2.21}$$

where $|\bar{V}_r|$ is the mean amplitude of the radial component of convective flow rate inside the flux tube in the dynamo-region of the photosphere. The main contribution to the resistance of the circuit is due to the last term on the right-hand side of Eqn (2.20), which is connected with the dynamo-region of the loop. In this region, according to Eqns (2.16) and (2.18), the electric current density is practically perpendicular to the magnetic field vector, whereas the plasma is partly ionized. Relatedly, a governing role is played by the Cowling conductivity [36]

$$\sigma_{\mathrm{K}} = \frac{\sigma_1}{1 + F^2 \omega_{\mathrm{e}} \omega_{\mathrm{i}} / \left[(2-F)\, v'_{\mathrm{ei}} v'_{\mathrm{ia}}\right]}, \tag{2.22}$$

which for $F^2 \omega_{\mathrm{e}} \omega_{\mathrm{i}} / [(2-F)\, v'_{\mathrm{ei}} v'_{\mathrm{ia}}] \gg 1$ is much smaller than the isotropic conductivity σ_1. Since ω_{e} and ω_{i} depend on the self-consistent magnetic field of the loop, the circuit resistance proves to be a function of the current I. If the current-carrying loop is approximated by a thin wire with radius r, its inductance can be represented as [46]

$$L = 2l\left(\ln \frac{4l}{\pi r} - \frac{7}{4}\right), \tag{2.23}$$

where r and l can be substituted by the values taken for the coronal part of the loop.

The characteristic time for the current in the loop to reach its maximum value is set by the smallest of two time scales:

$$t_R = \frac{L}{c^2 R}, \quad t_L = \left(\frac{1}{L} \frac{\mathrm{d}L}{\mathrm{d}t}\right)^{-1}. \tag{2.24}$$

The time scale t_R pertains to the current growth in a stationary loop. If the loop inductance varies with time, for instance, because of the magnetic loop expansion in size, and if simultaneously $t_L < t_R$, the time scale of current growth becomes t_L. The characteristic time t_L spans several hours, i.e., it is comparable to the lifetime of the supergranulation cell. The time scale t_R is of a similar order of magnitude if it is estimated by characteristic sizes ($l \approx 5 \times 10^9$ cm) of single flare loops on the Sun and parameters of the dynamo-region in the photosphere.

According to equation (2.19), the steady-state current is determined from the relationship

$$R(I)\, I = \Xi(I) \tag{2.25}$$

which, as can readily be seen, coincides with formula (2.15) if one ignores a negligible contribution from the coronal loop part and the region of current closure to the total circuit resistance.

To derive an equation for natural oscillations of the loop as an equivalent RLC circuit, it is necessary to exclude velocity variations from the equation of plasma motion as a whole, viz.

$$\rho \frac{\mathrm{d}\mathbf{V}}{\mathrm{d}t} = \rho \mathbf{g} - \nabla p + \frac{1}{c} \mathbf{j} \times \mathbf{B}, \tag{2.26}$$

and the generalized Ohm's equation in its nonstationary form

$$\mathbf{E} + \frac{1}{c} \mathbf{V} \times \mathbf{B} = \frac{\mathbf{j}}{\sigma} + \frac{\mathbf{j} \times \mathbf{B}}{enc} - \frac{\nabla p_{\mathrm{e}}}{en} - \frac{F^2}{(2-F)\, cnm_{\mathrm{i}} v'_{\mathrm{ia}}} [\mathbf{j} \times \mathbf{B}] \times \mathbf{B} + \frac{(1-F)\, F^2}{(2-F)\, cnm_{\mathrm{i}} v'_{\mathrm{ia}}} \rho \frac{\mathrm{d}\mathbf{V}}{\mathrm{d}t} \times \mathbf{B}, \tag{2.27}$$

and express the electric field strength through the variations in electric current. Concurrently, it is necessary to carry out integration over the magnetic loop volume with due regard for the equation

$$\oint \frac{\partial E_z}{\partial t} \,\mathrm{d}l = -\frac{L}{c^2} \frac{\partial^2 I}{\partial t^2}. \tag{2.28}$$

As a result, the following equation is obtained for small-amplitude current oscillations $|I_\sim| \ll I$ [45]:

$$\frac{1}{c^2} L \frac{\partial^2 I_\sim}{\partial t^2} + \left(R(I) - \frac{|\bar{V}_r|\, l_1}{c^2 r_1}\right) \frac{\partial I_\sim}{\partial t} + \frac{1}{C(I)} I_\sim = 0. \tag{2.29}$$

The effective circuit capacitance is defined from the relationship

$$\frac{1}{C(I)} = \frac{I^2}{\pi c^4} \left(\frac{l_1}{\rho_1 r_1^4} + \frac{l_2}{\rho_2 r_2^4}\right) \left(1 + \frac{c^2 r_1^2 B_z^2(0)}{4I^2}\right). \tag{2.30}$$

Since $l_1/\rho_1 \ll l_2/\rho_2$, the main contribution to the capacitance is made by the coronal part of the loop of length l_2. From equation (2.29) it follows that circuit oscillations are enhanced if $R(I) < |V_r|\, l_1/c^2 r_1$, i.e., when the current in the circuit is less than its steady-state value, and that they decay if the photospheric EMF ceases to act, for example, as a result of a decrease in the convection velocity due to plasma heating during a flare. The decay in this case is fairly slow because the circuit Q-factor $\left\{Q = [1/cR(I)]^{-1} \sqrt{L/C(I)}\right\}$ is rather large, reaching values of $10^3 - 10^4$ for typical parameters of flare loops.

The oscillation frequency of an RLC circuit is defined by the formula

$$v_{RLC} \approx \frac{1}{2\pi\sqrt{2\pi\Lambda}} \left(1 + \frac{c^2 r_2^2 B_z^2(0)}{4I^2}\right)^{1/2} \frac{I}{c r_2^2 \sqrt{n_2 m_{\mathrm{i}}}}, \tag{2.31}$$

where $\Lambda = \ln 4l/(\pi r_2) - 7/4$, and the values of r_2 and n_2 are related to the coronal part of the loop. The dependence of frequency on the current in formula (2.31) stems from the fact that the equivalent capacitance of the loop is determined by the Alfvén velocity which depends not only on the z-component, but also on the φ-component of the magnetic field in the loop.

The frequency does not depend on the current magnitude if the latter is sufficiently small:

$$v_{RLC} \approx \frac{1}{4\pi} \frac{B_z(0)}{r_2\sqrt{2\pi\Lambda n_2 m_i}}, \quad I \ll \frac{cr_2 B_z(0)}{2}, \tag{2.32}$$

and is proportional to the electric current if it is large:

$$v_{RLC} \approx \frac{I}{2\pi c r_2^2\sqrt{2\pi\Lambda n_2 m_i}}, \quad I \gg \frac{cr_2 B_z(0)}{2}. \tag{2.33}$$

This circumstance can be used to diagnose electric currents in coronal magnetic loops by temporal fluctuations in flare emission from the Sun and stars [16, 45].

2.5 Accumulation and dissipation of electric current energy in coronal loops. Diagnostics of electric currents

From relationships (2.32) and (2.33) it follows that the loop as an equivalent electric circuit has a period of eigen oscillations which, provided the current in the loop is large, $I \gg cr_2 B_z(0)/2$, is inversely proportional to the current amplitude:

$$P = \frac{2\pi}{c}\sqrt{LC(I)} \approx \frac{10 S_{17}}{I_{11}} \text{ [s]}, \tag{2.34}$$

where S_{17} is the cross-section area of the coronal part of the loop on the Sun in units of 10^{17} cm^2, and I_{11} is the current in the loop in units of 10^{11} A. This dependence arises from the circuit capacitance being dependent on the Alfvén velocity within the loop, i.e., the magnetic field whose magnitude, in turn, is a function of current in the loop. Indeed, since the capacitance is determined by the coronal part of the loop, namely

$$C(I) = \frac{c^4 \rho_2 S^2}{2\pi l_2 I^2}, \tag{2.35}$$

and the Biot – Savart law links the current and magnetic field intensity as $I \propto B\sqrt{S}$, formula (2.35) is equivalent to the expression for the capacitance of a capacitor, $C = \varepsilon_A S/l_2$, with l_2 being the distance between its plates, S their area, and $\varepsilon_A = c^2/V_A^2$ the permittivity of the medium with respect to Alfvén waves.

2.5.1 Modulation of microwave emissions from solar flares by *RLC* oscillations. *RLC* oscillations of a magnetic loop modulate its microwave emission of both thermal and nonthermal origin. Reference [45] reports on determining the magnitude of electric current based on the pulsation period of solar flare radiation in millimeter wave range, observed with the radio telescope in Metsähovi (Finland) in 1989 – 1993. Table 2 lists characteristics pertaining to a set of bursts with pulsations for flare loops on the Sun of typical sizes $S_{17} = 1$ and $l_2 = 5 \times 10^9$ cm. Spectral analysis revealed the modulation of radiation with the periods P ranging from 0.7 to 17 s, which yields the magnitudes of electric current $I \approx 6 \times 10^{10}$ – 1.4×10^{12} A. Table 2 also gives total energies of electric current, stored in respective circuits: $LI^2/2 \approx 10^{30}$ – 5×10^{32} erg.

Table 2. Bursts of solar emission in millimeter wave range characterized by pulsations with a high Q-factor, and parameters of the *RLC* circuit. F_{max} is the maximum value of the emission flux in millimeter wave range expressed in SFU (1 SFU = 10^{-22} W m^{-2} Hz^{-1}).

Date	Burst in millimeter band, UT	F_{max}, SFU	P, s	I, 10^{11} A	$LI^2/2$, 10^{31} erg
22.06.89	14:47 – 14:59	< 150	5.2	2.0	1.0
19.05.90	13:15 – 13:40	10	0.7	14.2	50.0
01.09.90	7:06 – 7:30	27	1.1	9.1	20.9
24.03.91	14:11 – 14:17	< 700	10.0	1.0	0.25
16.02.92	12:36 – 13:20	≈ 2000	5.0	2.0	1.0
08.07.92	9:48 – 10:10	≈ 2500	3.3	3.0	2.3
08.07.92	10:15 – 11:00	15	16.7	0.6	0.08
27.06.93	11:22 – 12:00	40	3.5	2.8	2.0

For some events it was possible to compare the energy stored in the magnetic loop with the flare energy. For instance, for the flare on 22 June 1989, formula (2.34) gives $I = 2 \times 10^{11}$ A and $LI^2/2 = 10^{31}$ erg. On the other hand, an estimate of thermal energy in the evaporating chromospheric plasma for this flare, derived from microwave and soft X-ray emission data [47], gives $E_{th} = (1.0 - 4.5) \times 10^{29}$ erg. The thermal energy of hot plasmas, as is known, makes up a marked part of flare energy. Thus, a conclusion can be drawn that in flaring less than 5 – 10% of electric current energy stored in the magnetic loop is released. This seems plausible for cases when the flare magnetic structure is not destroyed in the process of energy release.

Since a solar flare is accompanied by dissipation of current in the magnetic loop, the frequency of *RLC* oscillations should decrease as the flare develops. In contrast, if the loop current increases by the action of photospheric EMF, the frequency of *RLC* oscillations grows with time. The search for linearly frequency-modulated (LFM) signals (i.e., signals with a frequency obeying the expression $\omega = \omega_0 + Kt$, where K is a constant, and t is the time) with positive and negative frequency drifts in the spectrum of low-frequency modulation of microwave emissions from solar flares was carried out in Refs [48, 49]. To perform it, the Wigner – Ville transform [50 – 52] was applied to the analysis of microwave emission from solar flares observed at 37 GHz in Metsähovi. Several bursts were found with LFM peculiarities related to strong dissipation of electric current in the burst source — the coronal magnetic loop — during solar flares. Cases of modulation by LFM signals with the frequency growing with time were discovered too. They correspond to the process of electric current energy accumulation in the loop.

Reference [48] applied the Wigner – Ville transform to the analysis of low-frequency modulation of an intensity of four microwave bursts observed in 1991 at the radio observatory Metsähovi at 37 GHz. For all the explored events, a modulation of the radio emission flux with LFM signals of a characteristic frequency from 0.075 Hz to 0.9 Hz was discovered showing both positive and negative frequency drifts, which bears witness to the accumulation or dissipation of electric current energy in coronal magnetic loops. The magnitude of frequency drift was confined in the range

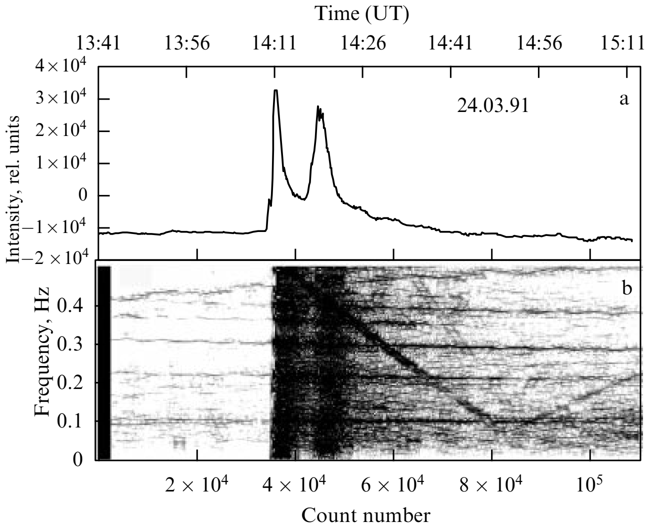

Figure 3. (a) Time profile of a radio emission burst from the Sun at a frequency of 22 GHz, recorded by radio observatory Metsähovi (Finland). (b) Dynamic spectrum of low-frequency modulation of radio emission flux.

$|(1/f)(\,\mathrm{d}f/\mathrm{d}t)| = 2.5\times10^{-5} - 1.4\times10^{-3}\ \mathrm{s}^{-1}$ for different events.

Figure 3 presents an example of such an analysis. A time profile (Fig. 3a) of the microwave burst on 24 March 1991 (14:05 UT) in an active region (S25W03) is shown. The maximum radio emission flux in the impulsive phase amounted to 70 SFU (Solar Flux Unit, $1\,\mathrm{SFU} = 10^{-22}\,\mathrm{W\,m^{-2}\,Hz^{-1}}$) with a total radio burst duration of about 30 min. Figure 3b displays the lower part of the dynamic spectrum of low-frequency modulation of radio emission flux. It embraces all phases of the burst. Taken as a whole, the dynamic spectrum represents an LFM signal with a frequency drifting from 0.5 Hz to 0.1 Hz at a characteristic velocity of $-2\times10^{-4}\ \mathrm{s}^{-1}$ in the initial phase of the event, which corresponds to the dissipation phase of electric current energy in the coronal magnetic loop. In the final burst phase, the drift velocity turns to zero and then changes sign, reaching $+1.4\times10^{-3}\ \mathrm{s}^{-1}$. The sign change in the frequency drift velocity of the LFM signal happened at 14:50 UT when the radio emission burst has practically decayed. It corresponds to the beginning of the phase of electric current energy accumulation in the coronal magnetic loop.

The data analysis performed for the four radio bursts yielded values of currents in coronal magnetic loops falling in the range $(0.75-9)\times10^{11}$ A and stored electric current energies lying within the range $1.4\times10^{30} - 2\times10^{32}$ erg. They agree with the results of Ref. [45] having applied the Fourier analysis to determine the period of low-frequency modulation in microwave bursts. For the event of 24 March 1991, the loop current decreased from 9×10^{11} A at the beginning of the burst to 10^{11} A at its final stage, i.e., by almost one order of magnitude. The energy release rate reached 10^{28} erg s^{-1}. After the flare, the frequency drift velocity of the LFM signal became positive, which corresponds to the renewal of the energy accumulation process in the coronal magnetic loop.

The examples given here can be considered as fairly important experimental evidence of the presence of dissipation and accumulation of the electric current energy in coronal loops. Estimates of electric current, stored energy, and the rate of its dissipation satisfactorily agree with respective values characteristic for flare processes on the Sun and obtained from other data. This demonstrates the efficiency of applying 'circuit' flare models based on the analogy between a flare and an electric circuit with a large inductance, in which the energy is stored in the form of electric current and is released at some instant of time following a drastic increase in the resistance.

2.5.2 Pulsating radio bursts from the star AD Leo. Radio emission from the active red dwarf AD Leo (Gliese 388, dM3.5e) located 4.85 pc apart has been repeatedly observed with large radio telescopes in the range 1.3 – 5.0 GHz. Observations have revealed the existence of quasiperiodic pulsations with periods in the range 1 – 10 s at the continuum background [7, 15, 53, 54]. The modulation depth in pulsations can reach 50% and the brightness temperatures of radio emission are in the range of $10^{10} - 10^{13}$ K, which hints at coherent mechanisms of radio emission. Phenomenologically, the pulsations resemble to a degree those of type IV solar radio emission [7]. Nevertheless, there are distinctions between stellar and solar radio pulsations, inviting separate research. The pulsations of AD Leo bursts exhibit a frequency drift of 100 – 400 MHz s^{-1} and possess a high degree of circular polarization (50 – 100%). The presence of frequency drift in radio bursts from AD Leo bursts and the high degree of polarization testify in favor of a periodic regime of particle acceleration in the stellar atmosphere, as well as the plasma mechanism of pulsating radio emission in the inhomogeneous atmosphere of the star. In Section 5 it is shown that the acceleration of electrons can be caused by electric fields brought about by convective motions at footpoints of magnetic loops in the stellar atmosphere, whereas the modulation of the accelerating process comes from oscillations in the loop magnetic field.

Reference [16] explored the dynamic spectrum of radio pulsations from a burst on the red dwarf AD Leo, recorded on 19 May 1997 (18:45 UT) in the frequency range 4.6 – 5.1 GHz with the help of a 100-meter radio telescope in Effelsberg (Germany). Figure 4a displays the time profile of radio emission at 4.85 GHz near the instant of the burst with a total duration of about 100 s. The emission with the flux at the burst maximum on the order of 300 mJy is present only in right polarization. The total duration of the burst phase equals about 50 s. The temporal resolution of digital recording is 1 ms. The time profile exhibits fluctuations in the radio emission flux, which have a character of pulsations in the dynamic burst spectrum in the range of 4.61 – 5.09 GHz. A preliminary analysis [15] revealed a component with a period of 2 s (0.5 Hz) in the pulsation spectrum, which is apparently different from the natural oscillation period of the telescope (Fig. 4b).

Figure 4c presents the spectrum of low-frequency pulsations in the range of 0 – 9 Hz, obtained through the Wigner – Ville transform for instants of time belonging to the descending part of the time profile of the first radio emission pulse. Apart from the noisy component, one can see here nearly equidistant narrow-band signals drifting over the frequency and exhibiting frequency splitting. The pulsation spectrum indicates that the emission source is simultaneously affected by two types of modulation: (1) short periodic pulses with repetition frequency $\nu_1 = 2$ Hz, and (2) a sinusoidal wave with frequency $\nu_2 = 0.5$ Hz.

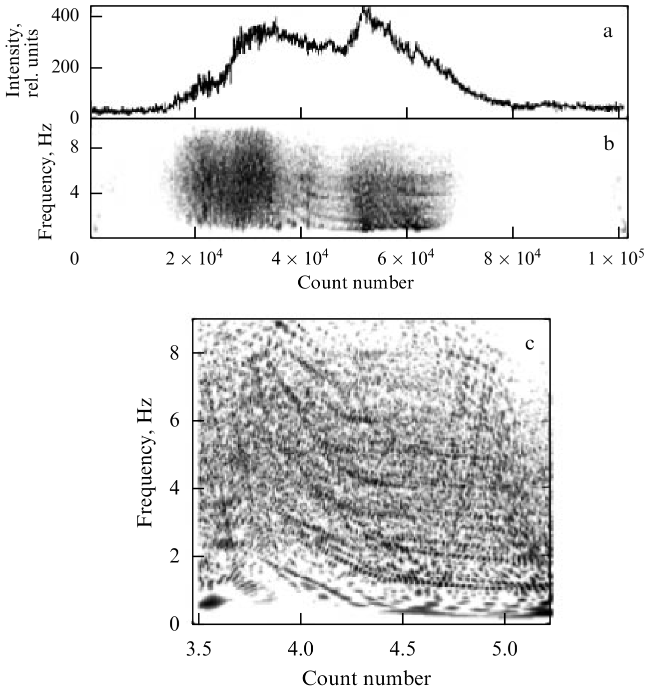

Figure 4. Flare on the red dwarf AD Leo on 19 May 1997 in the 5 GHz range. (a) Light curve with the duration of the impulsive phase of about 50 s. (b) Dynamic spectrum of low-frequency pulsations, obtained with the Wigner – Ville transform. (c) A portion of the dynamic spectrum corresponding to the descending branch of the first pulse in this radio flare.

Analysis of a radio flare from AD Leo on 19 May 1997 [15] revealed that of two coherent mechanisms — the plasma and cyclotronic maser ones — the most probable is the plasma mechanism of radio emission from a coronal magnetic loop with the plasma number density $n \approx 2.3 \times 10^{11}$ cm^{-3}, temperature $T = 3 \times 10^7$ K, and magnetic induction $B = 730 - 810$ G. Proceeding from these data, it is possible to assume that low-frequency modulation of emission is linked with natural oscillations of the coronal magnetic loop (see Section 3) on the red dwarf. In agreement with this assumption, the pulse modulation comes from fast magnetoacoustic oscillations (sausage modes) of a magnetic loop with frequency $\nu_1 \approx V_A/a$, where $V_A = B/\sqrt{4\pi m_i n}$ is the Alfvén velocity, and a is the loop radius. Setting then $\nu_1 = 2$ Hz (which follows from the analysis of the pulsation spectrum) and $V_A = 7 \times 10^8 (\omega_e/\omega_p) = 3.5 \times 10^8$ cm s^{-1} ($\omega_e/\omega_p \approx 0.5$, which follows from the radio emission mechanism analysis of Ref. [15]), one arrives at a magnetic loop radius estimate $a \approx 1.8 \times 10^8$ cm, which is comparable to the radius of flare magnetic loops on the Sun.

As concerns the sinusoidal modulation, it, most likely, is caused by eigen modes of the magnetic loop as an equivalent electric circuit with a frequency obeying formula (2.31). This frequency depends on the strength of current flowing along the loop and decreases as the current dissipates during the flare, which explains the observed negative frequency drift of the modulating signal. Using the value of $\nu_2 = 0.5$ Hz (corresponding to the instant of 'slope break' in the spectrum in Fig. 4c) and the relationship $I = caB_z/2$, from the formula $\nu_2 = V_A/(a\sqrt{\pi \Lambda})$ we find the loop length $l \approx 4 \times 10^{10}$ cm, which proves to be of the same order as the radius of the star (3.5×10^{10} cm). It should be noted that the first VLBI observations of red dwarfs [3] supported the existence of large coronal loops whose size is on the order or larger than stellar radii (Fig. 1b). Adopting further a maximum value of $\nu_2^{\max} \approx 2$ Hz (the lower track in Fig. 4c), an opportunity appears to estimate the following quantities: the magnitude of electric current at the instant of time corresponding to the maximum of the first pulse in the radio burst, $I^{\max} \approx 4.5 \times 10^{12}$ A; the amount of electric current energy stored in the loop, $W \approx LI^2/c^2 \approx 5.5 \times 10^{33}$ erg, and the energy release rate, $\dot{W} \approx 10^{32}$ erg s^{-1}. The last value exceeds the power of a typical solar flare by 2 – 3 orders. This results from large strengths of the magnetic field on red dwarf surfaces and the augmented activity of photospheric convection.

2.6 Explosive Joule energy release. The role of flute instability and Cowling conductivity

Analysis shows that neither the classic (Spitzer) resistance nor the strongest plasma microinstabilities (for instance, the Buneman instability) provides the needed value for the flare loop resistance. The authors of this review drew attention [37, 38] to the possibility of augmented current dissipation in a coronal loop if the neutral plasma component and nonstationarity of the process are taken into account. In this case, the Cowling conductivity [36], which is by many orders of magnitude lower than the classical Spitzer conductivity, becomes important. The effect of the significant increase in the Joule dissipation in partly ionized gas was first exposed by Schlüter and Biermann [55]. This effect springs from large energy losses of ions moving through a gas of neutral particles under the action of Ampère force $\mathbf{j} \times \mathbf{B}$. By way of example, in interstellar clouds the Cowling conductivity is smaller than the Spitzer conductivity by 10 – 12 orders of magnitude [56].

References [37, 38, 57] revealed that the generalized Ohm's law, written with account for process nonstationarity, viz.

$$\mathbf{E}^* = \frac{\mathbf{j}}{\sigma} + \frac{\mathbf{j} \times \mathbf{B}}{enc} - \frac{\nabla p_e}{en} + \frac{F}{cnm_i \nu'_{ia}} \left[(n_a m_a \mathbf{g} - \nabla p_a) \times \mathbf{B} \right] - \frac{F^2}{cnm_i \nu_{ia}} \rho \frac{d\mathbf{V}}{dt} \times \mathbf{B}, \tag{2.36}$$

together with Maxwell's equations, the equation of plasma motion as a whole, viz.

$$\rho \frac{d\mathbf{V}}{dt} = \rho \mathbf{g} - \nabla p + \frac{1}{c} \mathbf{j} \times \mathbf{B}, \tag{2.37}$$

and the continuity equation

$$\frac{\partial \rho}{\partial t} + \mathrm{div}(\rho \mathbf{V}) = 0, \tag{2.38}$$

describe in a self-consistent way the behavior of plasma and electromagnetic fields in the process of flare energy release in a coronal magnetic loop. It should be recalled that here $\mathbf{E}^* = \mathbf{E} + \mathbf{V} \times \mathbf{B}/c$ is the electric field in a coordinate system co-moving with the plasma, $\rho = n_a m_a + n_e m_e + n_i m_i$ is the density of partly ionized plasma, $p = p_a + p_e + p_i$ is the pressure, $\sigma = ne^2/[m_e(\nu_{ei} + \nu_{ea})]$ is the Spitzer conductivity, and $F = \rho_a/\rho$ is the relative density of neutrals.

The Joule current dissipation is characterized by the quantity $q = \mathbf{E}^* \mathbf{j}$ which, taking into account relationships (2.36) – (2.38), can be represented as [37, 38, 57]

$$q = \frac{j^2}{\sigma} + \frac{F^2}{c^2 n m_i \nu'_{ia}} (\mathbf{j} \times \mathbf{B})^2. \tag{2.39}$$

It is apparent that in force-free field ($\mathbf{j} \parallel \mathbf{B}$) the second term on the right-hand side of formula (2.39) disappears and the current dissipation is defined by the Spitzer conductivity. The dissipation is highest at $\mathbf{j} \perp \mathbf{B}$. The cause of augmented dissipation in a coronal loop can be a ballooning instability of the chromosphere [57] or a prominence [58] located above the loop (see Fig. 2). A 'tongue' of partly ionized plasma, penetrating into the current channel, deforms the magnetic field according to the equation

$$\frac{\partial \mathbf{B}}{\partial t} = \nabla \times \left[\left(\mathbf{V} + \frac{F^2}{cnm_{\mathrm{i}}v_{\mathrm{ia}}}\, \rho\, \frac{\mathrm{d}\mathbf{V}}{\mathrm{d}t} \right) \times \mathbf{B} \right]. \tag{2.40}$$

As a result, the Ampère force appears, which does furnish the augmented dissipation of the current. Integrating expression (2.39) over the loop volume, one obtains the energy release power [37]

$$\frac{\mathrm{d}W}{\mathrm{d}t} = \left[\frac{m_{\mathrm{e}}(v_{\mathrm{ei}} + v_{\mathrm{ea}})\, d}{e^2 nS} + \frac{2\pi F^2 I^2 d}{c^4 nm_{\mathrm{i}} v_{\mathrm{ia}} S^2} \right] I^2$$

$$= \left[R_{\mathrm{c}} + R_{\mathrm{nl}}(I) \right] I^2 , \tag{2.41}$$

where d is the characteristic size of the tongue of partly ionized plasma penetrating into the current channel, R_{c} is the classical (according to Spitzer) resistance, and R_{nl} is the Cowling resistance proportional to the current I squared. Supposing that $d \approx 5 \times 10^7$ cm, $S \approx 3 \times 10^{16}$ cm^2, $I \approx 3 \times 10^{11}$ A, $n \approx 10^{11}$ cm^{-3}, $T \approx 10^4$ K, and $F \approx 0.5$, from equation (2.41) it follows that $R_{\mathrm{nl}} \approx 10^{-3}$ Ohm, which provides the power of flare energy release equal to 10^{27} erg s^{-1}. For currents $I \approx 10^{12}$ A, the energy release power increases to 10^{29} erg s^{-1}.

Wheatland and Melrose [59] argue that flare magnetic loops are force-free, so that the above-given estimate of the power of energy release can prove to be too high. They, however, did not take into account the process of penetration of partly ionized plasma into the loop as a consequence of existing the ballooning mode of flute instability, which changes the magnetic field in agreement with equation (2.40). Analysis of regimes of plasma tongue penetration into the current channel [57] demonstrated that the dynamics of Joule plasma heating depend on both the parameters of the tongue and flare plasma characteristics, in particular, the distribution of gas pressure over the loop radius.

Let us illustrate these positions by the example of a magnetic flux tube with a force-free magnetic field ($\mathbf{j} \times \mathbf{B} = 0$) specified as [11]

$$B_{\varphi 0} = \frac{r}{r_0}\, \frac{B_0}{1 + r^2/r_0^2} , \quad B_{z0} = \frac{B_0}{1 + r^2/r_0^2} . \tag{2.42}$$

To be specific, let us adopt the following approximation for the velocity of plasma flowing into the current channel [19]: $V_r(r, t) = V_0(t)\, r/r_0$, $r \leqslant r_0$. Then, the components B_φ and B_z of magnetic field will evolve as

$$B_\varphi(r, t) = \exp(y)\, B_{\varphi 0}[r \exp(y)] ,$$

$$B_z(r, t) = \exp(2y)\, B_{z0}[r \exp(y)] ,$$

$$y = -\frac{1}{r_0} \int_0^t \left(V_0(t') + \frac{F^2 \rho}{nm_{\mathrm{i}} v'_{\mathrm{ia}}}\, \frac{\mathrm{d}V_0}{\mathrm{d}t'} \right) \mathrm{d}t' . \tag{2.43}$$

Equations (2.39), (2.40), and (2.43) allow one to explore the dependence of energy release rate in the magnetic flux tube on time and coordinate as the flute instability develops. This can most easily be performed in the vicinity of the tube axis, where the dependence of pressure on radius is quadratic, $p(r, t) = p_{00}(t) + p_0(t)\, r^2/r_0^2$, and function y can be considered small compared to unity. Physically, this implies that the amplitude of oscillations of the plasma tongue penetrating into the tube is small compared to the tube radius. In this case, with account for equation (2.37) we arrive at the following system of equations for V_0, p_0, and y:

$$\frac{\partial V_0}{\partial t} = -\frac{2p_0}{r_0} + \frac{B_0^2}{\pi r_0}\, y , \tag{2.44}$$

$$\frac{\partial p_0}{\partial t} = \frac{(\gamma - 1)\, F^2 B_0^4}{nm_{\mathrm{i}} v'_{\mathrm{ia}} \pi^2 r_0^2}\, \frac{\partial V_0}{\partial t}\, y^2 , \tag{2.45}$$

$$\frac{\partial y}{\partial t} = -\frac{V_0}{r_0} - \frac{F^2 \rho}{nm_{\mathrm{i}} v'_{\mathrm{ia}} r_0}\, \frac{\partial V_0}{\partial t} . \tag{2.46}$$

In the general case, the system of equations (2.44)–(2.46) describes pulsating regimes of energy release when a flute of outer plasma penetrates into the loop by virtue of a series of oscillations. Moreover, an explosive regime occurs when the plasma pressure increases from the loop axis toward its periphery, i.e., $p_0 > 0$, and balances the Ampère force accompanying the development of flute instability, i.e., $p_0 = B_0^2 y/2\pi$. In this case, it follows from equations (2.44) and (2.45) that

$$y = \frac{y_0}{1 - (t/t_0)} , \quad t_0 = \frac{nm_{\mathrm{i}} v'_{\mathrm{ia}} \pi r_0^2}{2(\gamma - 1)\, F^2 B_0^2 y_0} , \tag{2.47}$$

i.e., the ratio of gas pressure to the magnetic field pressure in the loop, $\beta = 8\pi p/B^2 \approx 4y$, grows in an explosive manner with the growth of y from a value of $y_0 \ll 1$ up to the values when effects unaccounted for and limiting energy release come into play. They include, for example, an increase in the degree of ionization as the plasma gets heated, which reduces energy release caused by ion–atom collisions.

2.7 Inductive interaction of coronal magnetic loops

Equations (2.19) and (2.29) for slow and fast variations of the electric current in a coronal magnetic loop are valid for a loop which is magnetically shielded from the neighboring loops, i.e., these equations do not describe mutual induction effects connected with variations in external magnetic flux through the loop contour. These effects can be taken into account in the integration of the generalized Ohm's law by augmenting the quantity

$$\frac{\partial}{\partial t} \oint E_z\, \mathrm{d}z$$

with the electromotive force of mutual induction:

$$\frac{1}{c^2}\, \frac{\partial^2}{\partial t^2} \left[\sum_j^N M_j I_j \right] ,$$

where I_j is the current in the jth loop, and M_j is the coefficient of mutual induction between loop j and the loop under consideration, whereas summation is taken over all loops surrounding the given one. For slowly varying currents in the surrounding loops (on a time scale much longer than the period of *RLC* oscillations, $1/\nu_{RLC} \ll t_{\rm curr}$, where $t_{\rm curr}$ is a characteristic time scale of current variability), mutual induction will only affect slow variations in the equilibrium current I_{z0} in the given loop. Thus, exploring fairly fast *RLC* oscillations of electric current in the loop, one can discard the effects from surrounding loops. In particular, these effects will not modify the functional dependence of the frequency ν_{RLC} on the magnitude of the current I_{z0} flowing through the loop. At the same time, slow variations in I_{z0} coming from inductive interaction with the surrounding loops will lead to a certain drift of the *RLC*-oscillation frequency ν_{RLC}, oscillations which, in turn, modulate microwave emission and thus can be detected in low-frequency spectra. In this respect, we can distinguish two types of electric current dynamics in magnetic loops: 'fast processes', i.e., *RLC* oscillations of

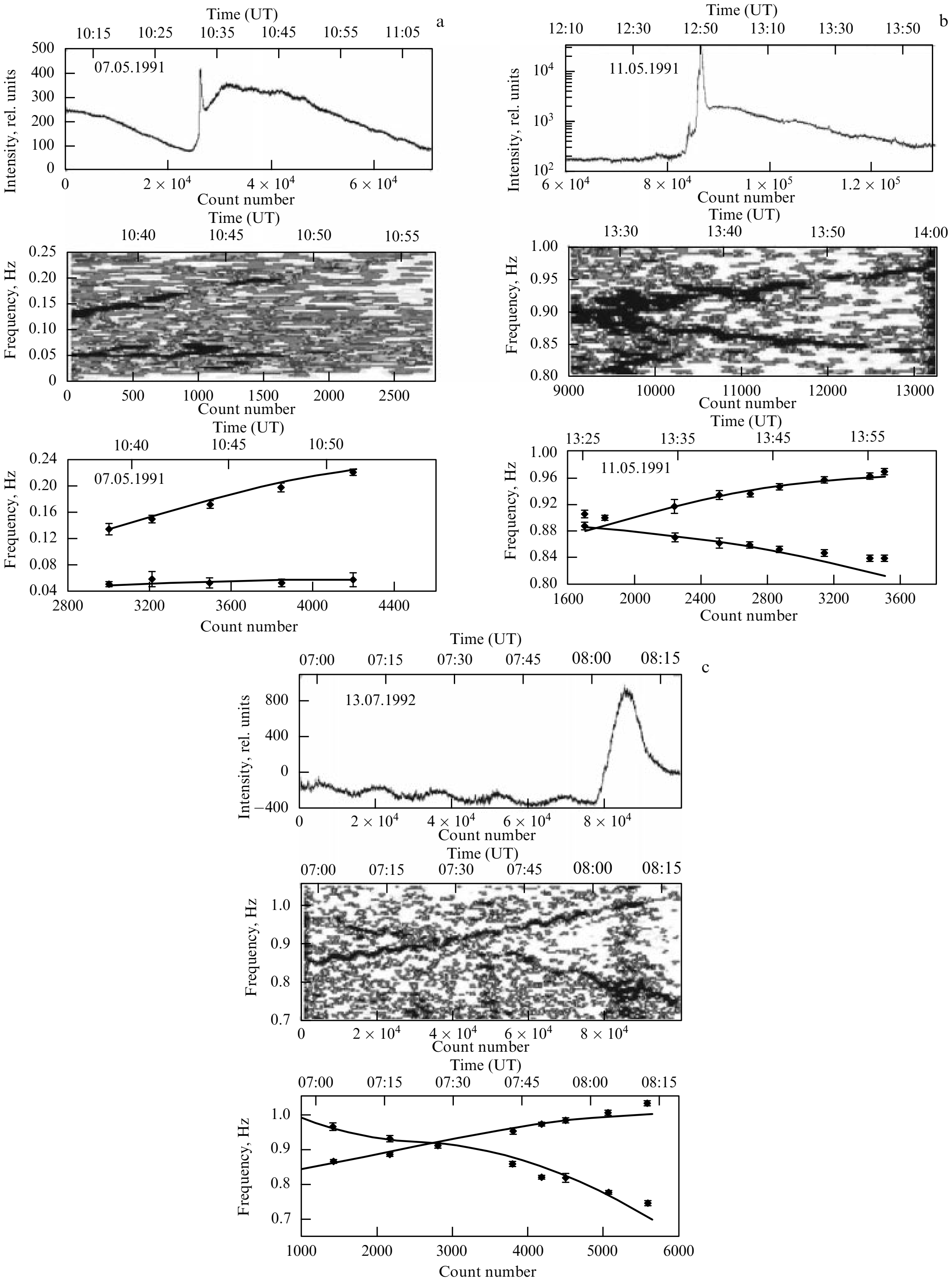

Figure 5. Inductive interaction between two current-carrying loops pertaining to their emersion or relative motion. Slow variations in the current stemming from inductive interaction with a neighboring loop lead to a drift in the modulation frequency of microwave emission.

electric current around its equilibrium value I_{z0}, and 'slow processes', i.e., changes in the equilibrium current leading to the drift of the *RLC*-oscillation frequency. One of the causes of the slow variability of I_{z0} is the increase in current under the action of photospheric EMF, already considered in Section 2.5, or its dissipation following the development of a flaring process in the coronal magnetic loop. The other reason can be the induction EMF brought about by the interaction of the magnetic loop with other loops during their emersion or relative motion [21, 22, 25]. In the latter case, the system of equations for slow current variations in two inductively interacting magnetic loops is written out in the following way [25]:

$$\frac{1}{c^2}\frac{\partial}{\partial t}\left(L_1 I_1 + M_{12} I_2\right) + I_1 R_1(I_1) = \Xi_1\,, \tag{2.48}$$

$$\frac{1}{c^2}\frac{\partial}{\partial t}\left(L_2 I_2 + M_{21} I_1\right) + I_2 R_2(I_2) = \Xi_2\,. \tag{2.49}$$

Here, $L_{1,2}$ are the loop inductances described by formula (2.23) with a due set of parameters for each loop, $R_{1,2}(I_{1,2})$ are the loop impedances given by formula (2.20), and $\Xi_{1,2}$ are the EMFs (2.21) in the photospheric loop footpoints. For loops approximated by thin toroids with their principal radii $R^{(i)}_{\rm loop} \gg r_i$ (r_i are the small radii of toroids), the mutual inductance coefficients can be approximated as [60, 61]

$$M_{12} = M_{21} = 8(L_1 L_2)^{1/2}\left[\frac{R^{(1)}_{\rm loop} R^{(2)}_{\rm loop}}{\left(R^{(1)}_{\rm loop} + R^{(2)}_{\rm loop}\right)^2 + d^2_{1,2}}\right]\cos\varphi\,, \tag{2.50}$$

Table 3. Parameters of coronal loops for the three flares presented in Fig. 5. Listed are the large ($R_{\rm loop}$) and small (r_0) loop radii, velocities v of loop emersion, temperature T, magnetic field B, and plasma density in the loops.

Parameter	Date of event		
	7 May1991	11 May 1991	13 July 1992
$r_0^{(1)}$	600 km	600 km	590 km
$r_0^{(2)}$	550 km	700 km	510 km
$R^{(1)}_{\rm loop\,0}$	20,000 km	20,000 km	20,000 km
$R^{(2)}_{\rm loop\,0}$	1000 km	1000 km	3000 km
v_1	0.5 km s^{-1}	1.2 km s^{-1}	0.5 km s^{-1}
v_2	4.5 km s^{-1}	4.9 km s^{-1}	2.5 km s^{-1}
T_{01}	10^7 K	10^7 K	2×10^6 K
T_{02}	10^7 K	5.0×10^6 K	1.0×10^6 K
n_1	1.3×10^9 cm^{-3}	2.0×10^9 cm^{-3}	3.5×10^9 cm^{-3}
n_2	2.4×10^9 cm^{-3}	4.5×10^9 cm^{-3}	5.0×10^9 cm^{-3}
I_{01}	1.7×10^8 A	-1.58×10^{10} A	-1.8×10^{10} A
I_{02}	1.7×10^8 A	1.58×10^{10} A	2.3×10^{10} A
B_1	85 G	120 G	170 G
B_2	85 G	120 G	100 G
d_{12}	2500 km	2500 km	2500 km
φ_{12}	$\pi/20$	$\pi/4$	$\pi/4$

where $R^{(1,2)}_{\rm loop}$ are the principal radii of the loops, $d_{1,2}$ is the distance between the toroid centers, and φ is the angle between the normals drawn to the toroid planes.

Equations (2.48), (2.49) were used in Ref. [25] to model double tracks appearing sometimes in the spectra of low-frequency modulation of microwave emission from flares.

Figure 5 shows time profiles of microwave radio emission at 37 GHz from three flares, their dynamic spectra of low-frequency modulation obtained with the Wigner–Ville transform, and the results of modeling these spectra numerically with *RLC* oscillations of two inductively interacting coronal magnetic loops. The parameters of the loops and their emersion velocities and mutual orientation for which numerical results agree best with observational data are given in Table 3.

3. The coronal loop as a resonator for MHD oscillations

An important event in the astrophysics of the 1960's was the discovery of five-minute oscillations on the Sun, which gave birth to a new branch in solar physics — *helioseismology*. Five-minute oscillations represent acoustic type waves (p-modes). Their spectrum contains extremely valuable information on the internal structure of the Sun. Later on, the methods of helioseismology were applied to explore oscillations of local structures such as sunspots and prominences. Advances in helioseismology and the studies of stellar oscillations have led to the establishment of *asteroseismology* [62].

Observations of ultraviolet (UV) solar radiation by TRACE with high spatial resolution revealed oscillations of coronal loops [63], which gave impetus to a new promising avenue of astrophysics — *coronal seismology* studying wave and oscillatory processes in stellar coronae. The Dutch astrophysicist Rosenberg [64] can be considered a founder of coronal seismology. He was the first to attribute second pulsations of type IV solar radio emission (Fig. 6a) to magnetohydrodynamic oscillations of coronal loops. Later this idea was further developed by many researchers (see reviews [65–67]). Methods of coronal seismology were exploited as well to interpret pulsations of emissions from red dwarfs in various bands of the spectrum of electromagnetic radiation [7, 15, 68–71].

Interest in loop oscillations is connected not only with the possibility of explaining the origin of coronal heating and stellar wind acceleration, but also with improvement in the methods used to diagnose the parameters and physical processes in coronal loops and, in particular, in flare loops.

3.1 Natural oscillations of loops and the diagnostics of flare plasma

Magnetic hydrodynamics occupies an important place in interpreting the wave and oscillatory phenomena in stellar coronae. An impedance for MHD oscillations experiences jump at the 'loop–ambient medium' interface, so that the coronal loop can be considered as a resonator.

In the first approximation, the oscillations of coronal magnetic loops can be explored considering a homogeneous magnetized plasma column of radius a and length l, the ends of which are 'frozen' in a superconducting plasma. The plasma inside the cylinder has the density $\rho_{\rm i}$ and temperature $T_{\rm i}$, and the magnetic field induction $B_{\rm i}$ is aligned with the cylinder axis. Outside the cylinder, the respective parameters

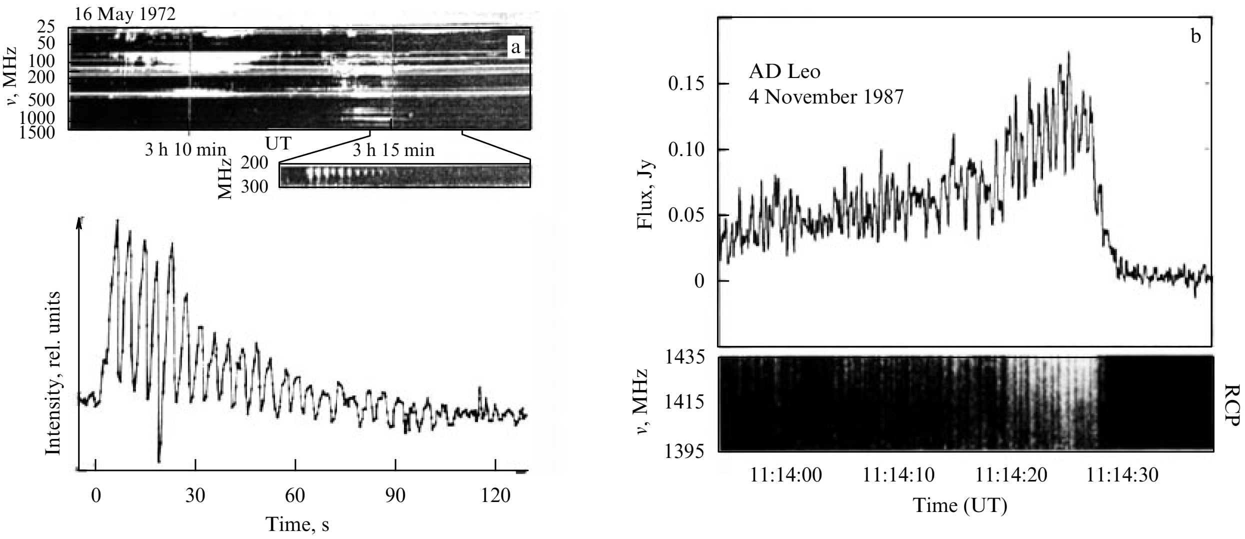

Figure 6. Examples of quasiperiodic pulsations of radio emission from (a) the Sun [72], and (b) the flaring star AD Leo [7]; RCP stands for right circular polarization.

are ρ_e, T_e, and B_e. The dispersion relation linking the frequency ω of natural oscillations of a cylinder with the components of wave vectors $k_\perp$ and $k_\parallel$ takes the form [73, 74]

$$\frac{J_m'(\varkappa_i a)}{J_m(\varkappa_i a)} = \alpha\, \frac{H_m^{(1)'}(\varkappa_e a)}{H_m^{(1)}(\varkappa_e a)}\,. \tag{3.1}$$

Here,

$$\varkappa^2 = \frac{\omega^4}{\omega^2(c_s^2 + c_A^2) - k_\parallel^2 c_s^2 c_A^2} - k_\parallel^2\,,$$

$$\alpha = \frac{\varkappa_i \rho_i}{\varkappa_e \rho_e}\, \frac{\omega^2 - k_\parallel^2 c_{Ai}^2}{\omega^2 - k_\parallel^2 c_{Ae}^2}\,,$$

c_s is the speed of sound, c_A is the Alfvén velocity, J_m and $H_m^{(1)}$ are the Bessel and Hankel functions of the first kind, $k_\parallel = \pi s/l$, and $s = 1, 2, 3, \ldots$. For a thin ($r/l \ll 1$) and dense ($\rho_e/\rho_i \ll 1$) cylinder at $m = 0$, Eqn (3.1) allows one to determine the frequency of fast magneto-acoustic (sausage) oscillations:

$$\omega_+ = (k_\perp^2 + k_\parallel^2)^{1/2} (c_{si}^2 + c_{Ai}^2)^{1/2}\,. \tag{3.2}$$

The wave number perpendicular to the magnetic field, $k_\perp = \lambda_i/a$, where λ_i are the zeros of the Bessel function $J_0(\lambda) = 0$. Fast magneto-acoustic waves (the sausage mode) contributing most to modulation of loop emission can suffer marked damping related to their emission into the surrounding medium [73, 75]:

$$\gamma_a = \frac{\pi}{2}\,\omega_+ \left(\frac{\rho_e}{\rho_i} - \frac{k_\parallel^2}{k_\perp^2}\right), \quad \frac{\rho_e}{\rho_i} > \frac{k_\parallel^2}{k_\perp^2}\,. \tag{3.3}$$

The physical mechanism of acoustic damping is clear: sausage oscillations of the loop are accompanied by excitation of waves in the surrounding medium, which is achieved with an expenditure of the oscillation energy. The acoustic damping is absent if $\rho_e/\rho_i < k_\parallel^2/k_\perp^2$, which corresponds to total internal reflection, i.e., a sufficiently dense and 'thick' loop represents an ideal resonator for sausage waves. A similar result was obtained by Nakariakov et al. [76] for the global sausage mode without radiation: $l/a < 1.3(\rho_i/\rho_e)^{1/2}$. Oscillations in the global sausage mode were observed in the solar flare on 28 August 1999, recorded by the Radioheliograph Nobeyama at a frequency of 17 GHz [76]. In this case, all parts of the loop were oscillating in phase with a period of $P \approx l/c_{Ai} \approx 14-17$ s.

The $m = 1$ case corresponds to kink oscillations of loops first recorded by the space observatory TRACE [63] during the solar flare on 14 July 1998. The frequency of kink oscillations is expressed as

$$\omega_k = k_\parallel \left(\frac{\rho_i V_{Ai}^2 + \rho_e V_{Ae}^2}{\rho_i + \rho_e}\right)^{1/2}\,. \tag{3.4}$$

Analyzing similar oscillations, Nakariakov and coauthors [77] drew attention to their low Q-factors ($Q = \omega/\gamma \leqslant 10$), and came to a conclusion about anomalous damping of kink loop oscillations. In particular, the dissipation of waves in the loop due to viscosity and conductivity should exceed the classical one by 8–9 orders of magnitude, i.e., the Reynolds number should have the magnitude of $\mathrm{Re} \sim 10^{5-6}$ instead of the classical value $\mathrm{Re} = 10^{14}$, whereas the Lundquist number takes the value $\mathcal{L} \sim 10^5$ instead of $\mathcal{L} = 10^{13}$. Reference [77] triggered a series of publications devoted to studies of oscillations in solar coronal loops and clarifying the origin of their low Q-factors. Uralov [78] suggested that the character of loop oscillations is determined by the medium, i.e., the dispersion properties of the corona. Oscillations of a corona excited by an external perturbation (flare or filament eruption) also draw into oscillations the coronal magnetic loops. Low Q-factors of kink loop oscillations were explained in Refs [78, 79] by dispersive spreading of fast magneto-acoustic waves, produced by a flare. Reference [80] took into account the inhomogeneity of coronal loops and proposed a mechanism of resonant decay of the kink mode through its interaction with Alfvén waves. A physically transparent mechanism for the observed strong decay of loop oscillations was recently suggested in Ref. [81]: an oscillating loop expends its energy on overcoming the drag of ambient medium.

The curvature of the magnetic field and fairly large magnitude of the plasma parameter $\beta = 8\pi nk_B T/B^2 > 0.1-0.3$ in coronal loops create favorable conditions for the excitation of a ballooning mode of flute instability. Ballooning oscillations arise as a result of the joint action of a destabilizing force $F_1 \sim p/R_{\text{loop}}$ linked to the pressure gradient and curvature of the magnetic field and a restoring force $F_2 \sim B^2/R_{\text{loop}}$ come about from the tension of magnetic field lines. The dispersion relation of the ballooning mode has the form [82]

$$\omega^2 - k_\parallel^2 V_A^2 = -\frac{p}{R_{\text{loop}}\rho d}, \quad d = \begin{cases} b, & b \gg \lambda_\perp, \\ \lambda_\perp, & b \ll \lambda_\perp. \end{cases} \tag{3.5}$$

Here, $b = n(\partial n/\partial x)^{-1}$, and $\lambda_\perp$ is the lateral size of the plasma tongue. Since the loop footpoints are frozen in the photosphere, one has $k_\parallel = N\pi/l$, where N is a natural number equal to the number of oscillating regions along the loop length l, and for the oscillation period it is readily found that

$$P_1 = \frac{2l}{V_A}\left(N^2 - \frac{l\beta}{2\pi d}\right)^{-1/2} \approx \frac{2l}{V_A N}. \tag{3.6}$$

3.2 Mechanisms of loop oscillation excitation. Parametric resonance

The most common mechanism underlying the generation of loop oscillations is their excitation by an external source (flare, filament eruption) or by an electrodynamically connected neighboring loop-trigger [78, 83]. If flare energy release happens in the coronal loop proper, then the generation of sausage oscillations is possible in the loop, provided the flare unfolds sufficiently fast (impulsively) [84]. FMA oscillations of loops can also be excited by high-energy protons at bounce resonance, $\omega = s\Omega$, $s = 1, 2, \ldots$, where Ω is the oscillation frequency of high-energy protons between magnetic 'mirrors' of the coronal loop. In this case, the pressure of energetic trapped protons is rather high: $\beta_{\text{pr}} > 0.2$ [75]. Taroyan et al. [85] have discovered excitation of slow magneto-acoustic waves ($\omega \approx k_\parallel c_s$) in a solar coronal loop as a consequence of heating in one of the loop footpoints during a microflare.

Exploring kink-oscillations of coronal loops with periods of about 300 s, Aschwanden et al. [61] conjectured that such oscillations can be initiated by five-minute oscillations of the photosphere (p-modes). Kislyakov et al. [86] demonstrated that under the action of five-minute oscillations of photospheric convection velocity on the footpoints of a coronal magnetic loop a parametric resonance is possible between photospheric p-modes and acoustic oscillations of coronal magnetic loops (Fig. 7).

If the coronal loop has an appropriate length, i.e., it is resonant with respect to the pumping frequency ν_0, the effect shows itself as the simultaneous excitation of oscillations with periods of 5, 10, and 3 min in the coronal magnetic loop, which correspond to ν_0, its subharmonic $\nu_0/2$, and the first upper frequency of the parametric resonance $3\nu_0/2$ (Fig. 8).

Since photospheric p-modes cannot directly penetrate the corona, the parametric resonance represents an effective channel for transferring the energy of photospheric oscillations to the upper layers of the solar atmosphere and opens important vistas for explaining the mechanisms of coronal plasma heating [87]. A recent paper by Hindman and Jain [88] considers the 'buffeting' excitation of five-minute oscillations

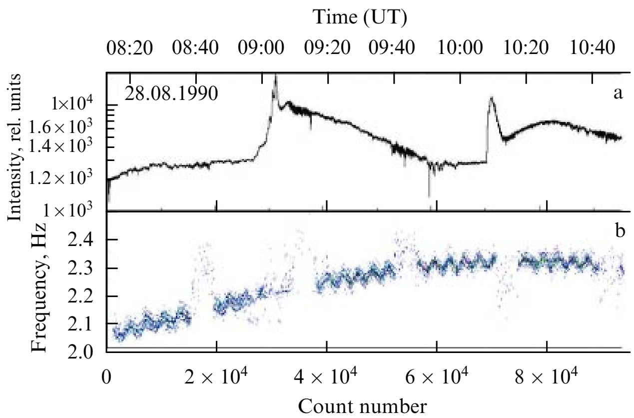

Figure 7. (a) Light curve for the solar flare on 28.08.1990 at a frequency of 22 GHz (Metsähovi). (b) Dynamic spectrum of 5-minute oscillations [86].

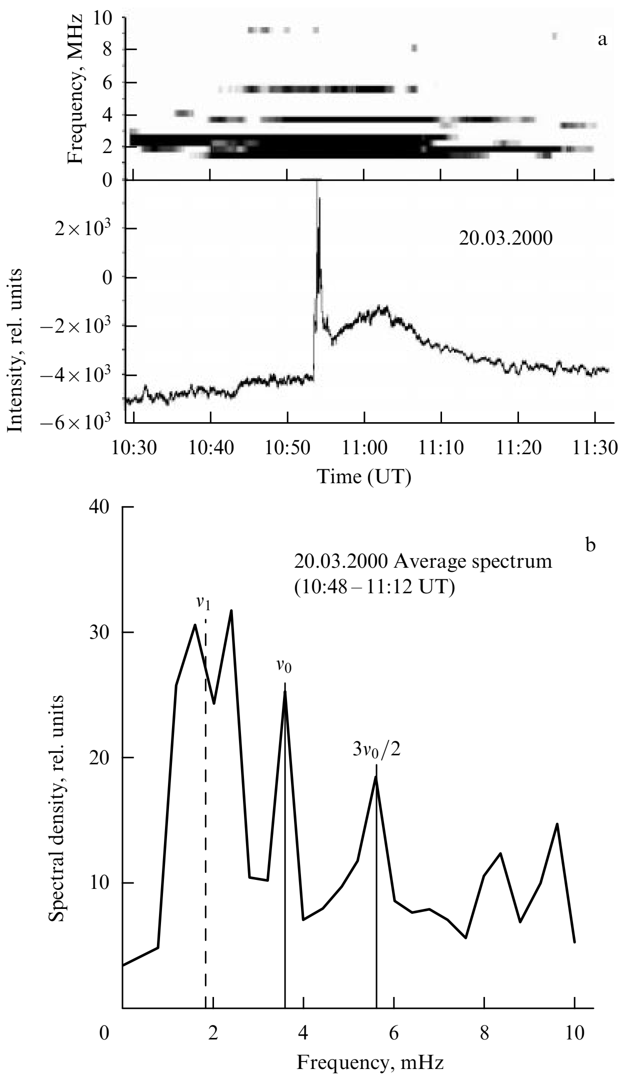

Figure 8. (a) Dynamic spectrum of the modulation of solar radio emission intensity at a frequency of 37 GHz and the light curve for the burst on 20.03.2000 [87]. (b) Section of the dynamic spectrum for the event of 20.03.2000. The dashed straight line marks the frequency of subharmonic $\nu_1 = \nu_0/2 \approx 1.8$ mHz, and full vertical straight lines mark frequencies of 5-minute ($\nu_0 \approx 3.6$ mHz) and 3-minute ($\nu_2 = 3\nu_0/2 \approx 5.6$ mHz) oscillations.

Table 4. Formulas for determining flare parameters from emission pulsations caused by ballooning and radial oscillations of a magnetic loop. Here $\chi = 10\varepsilon/3 + 2$, $\tilde{r} = 2.62\,a$, and $\varepsilon = \Delta/\zeta$.

Ballooning oscillations	Sausage (radial) oscillations
$T = 2.42 \times 10^{-8}\,\dfrac{l^2\varepsilon_1}{N^2 P_1^2}$ [K]	$T = 1.2 \times 10^{-8}\,\dfrac{\tilde{r}^2\varepsilon}{P^2\chi}$ [K]
$n = 5.76 \times 10^{-11}\,\dfrac{Q_1 l^3 \varepsilon_1^{7/2}}{N^3 P_1^4}\sin^2 2\theta\,[\text{cm}^{-3}]$	$n = 2 \times 10^{-11}\,\dfrac{Q\tilde{r}^3\varepsilon^{7/2}}{P^4\chi^{3/2}}\sin^2 2\theta\,[\text{cm}^{-3}]$
$B = 6.79 \times 10^{-17}\,\dfrac{Q_1^{1/2} l^{5/2}\varepsilon_1^{7/4}}{N^{5/2}P_1^3}\sin 2\theta$ [G]	$B = 2.9 \times 10^{-17}\,\dfrac{Q^{1/2}\tilde{r}^{5/2}\varepsilon^{7/4}}{P^3\chi^{5/4}}\sin 2\theta$ [G]

in magnetic loops by p-modes. They, however, assume that the loop magnetic field is potential and that the electric current in the loop is absent. The most likely mechanisms of interactions between p-modes and eigen modes of loops are, in our opinion, the heating of loop footpoints caused by dissipation of electric currents and the interaction of five-minute photospheric oscillations with the electric current flowing along the coronal magnetic loop.

3.3 Coronal seismology and the diagnostics of flare plasma

If the impedance jump across the boundary of a magnetic loop is sufficiently large, acoustic damping can be neglected. In this case, damping mechanisms attributed to dissipative processes within the loops are dominating. Estimates [89] indicate that the most essential factor for the decay of sausage and ballooning modes in solar loops is electron heat conductivity of plasma. Accordingly, their Q-factors can be expressed as

$$Q = \frac{\omega}{\gamma_c} \approx \frac{2m_e}{m_i}\,\frac{P\nu_{ei}}{\beta^2\sin^2 2\theta}\,, \qquad (3.7)$$

with $\theta = \text{arctg}(k_\perp/k_\parallel)$, and $P = 2\pi/\omega$ being the period of oscillations. Modulation of the flux of gyrosynchrotron emission with high-energy electrons with the spectral index δ of the power-law energy spectrum for an optically thin source — the coronal loop — emitting at a frequency above 10 GHz assumes the form

$$\Delta = 2\xi\,\frac{\delta B}{B} = \xi\beta\,, \quad \xi = 0.9\delta - 1.22 \qquad (3.8)$$

for sausage oscillations [89]. Equations (3.2) and (3.6) for the oscillation frequency, combined with Eqns (3.7) for the Q-factor and (3.8) for the radiation modulation depth allow the temperature, plasma density, and the magnetic field induction in the loop to be determined (Table 4).

Let us illustrate the potential of this diagnostic method with several examples.

3.3.1 Solar flare on 8 May 1998. Observations of the solar flare on 8 May 1998, belonging to class M 3.1 and occurring as a single loop, made at a frequency of 17 GHz with the Radioheliograph Nobeyama, and of hard X-rays with the satellite Yohkoh (Fig. 9) are indicative of ballooning oscillations with the period $P_1 = 16$ s and parameters $l = 8 \times 10^9$ cm, $N = 4$, $\theta = 66°$, $\Delta_1 \approx 0.3$, $Q_1 \approx 25$, and $\delta = 3.5$ [89]. Applying the formulas given in Table 4, we find the temperature $T \approx 5.9 \times 10^7$ K, number density $n \approx 1.4 \times 10^{11}$ cm^{-3}, and magnetic field induction $B \approx 425$ G in the flare loop and, consequently, the plasma parameter $\beta \approx 0.16$. For this value of β, the ballooning instability did not go into the aperiodic regime.

3.3.2 Flare on 28 August 1999. The solar flare on 28 August 1999, belonging to class M 2.8, illustrates the interaction

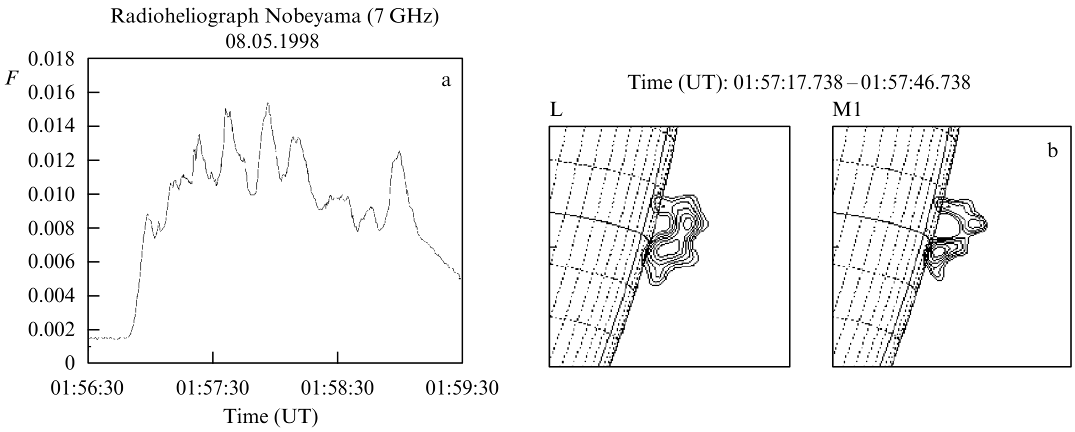

Figure 9. (a) Light curve for the flare on 8 May 1998, obtained with the Radioheliograph Nobeyama (17 GHz). (b) Patterns of X-ray emission sources in channels L (14 – 23 keV) and M_1 (23 – 33 keV), obtained with the satellite Yohkoh.

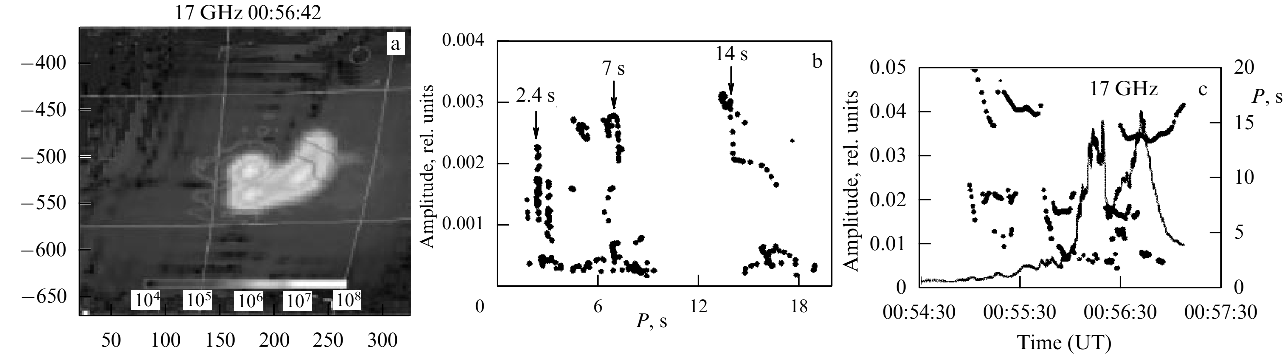

Figure 10. Image of two interacting loops in the flare on 28 August 1999, obtained with Radioheliograph Nobeyama (17 GHz) (axes give the source coordinates in angular seconds). (b) Spectrum of loop oscillations obtained with the help of wavelet-analysis. (c) Time profile of emission at 17 GHz and a change in oscillation periods with time.

between two loops (Fig. 10). Observations with the Radioheliograph Nobeyama (17 and 34 GHz) demonstrated that the flare consisted of two sources: a compact one ($\leqslant 10''$), and an extended one ($> 70''$). Wavelet analysis revealed characteristic pulsation periods of 14.7 and 2.4 s.

The event unfolded as follows. The flare energy release was accompanied by the development of ballooning oscillations in the compact source with $P_1 = 14$ s, $Q_1 \approx 10$, and $\Delta_1 = 0.4$. Oscillations with a period of 7 s can naturally be attributed to the harmonic of ballooning oscillations. The increase in the gas pressure (the growth in β) led to the development of the aperiodic mode of ballooning instability and interaction of the compact source with a neighboring loop, which was accompanied by injection of hot plasma and high-energy particles into the loop. Since oscillations with the period $P = 2.4$ s, $Q \approx 15$, and $\Delta = 0.1$ arose after the injection, the sausage modes of the extended source are most likely responsible for them. Using the formulas of Table 4 and the observed parameters of the pulsation sources, we obtain the following plasma characteristics of the compact and extended loops, respectively:

$$T \approx 4.6 \times 10^7 \text{ K}, \ n \approx 10^{11} \text{ cm}^{-3}, \ B \approx 300 \text{ G}, \ \beta \approx 0.18,$$

$$T \approx 2.1 \times 10^7 \text{ K}, \ n \approx 10^{10} \text{ cm}^{-3}, \ B \approx 120 \text{ G}, \ \beta \approx 0.06.$$

It is seen that the compact loop connected with the source of primary energy release has higher values of temperature, plasma density, and magnetic field.

It should be noted that the magnitudes of temperature, plasma concentration, and the magnetic field for the solar flares on 8 May 1998 and 28 August 1999, found by the method of coronal seismology, do not contradict the results of independent diagnostics with the use of optical and soft X-ray emissions [89].

3.3.3 Diagnostics of the flare on the star EV Lac by pulsations in the optical radiation. Observations of the flare on EV Lac on 11 September 1998 simultaneously with several geographically separated optical telescopes [90] revealed quasiperiodic oscillations in U and B bands with a characteristic period $P \approx 13$ s (Fig. 11). The Q-factor of pulsations was estimated as $Q \approx 50$, and the modulation depth of optical radiation as $\Delta \approx 0.2$.

Reference [91] suggests a model for pulsations of optical emission from EV Lac. According to it, the emission from

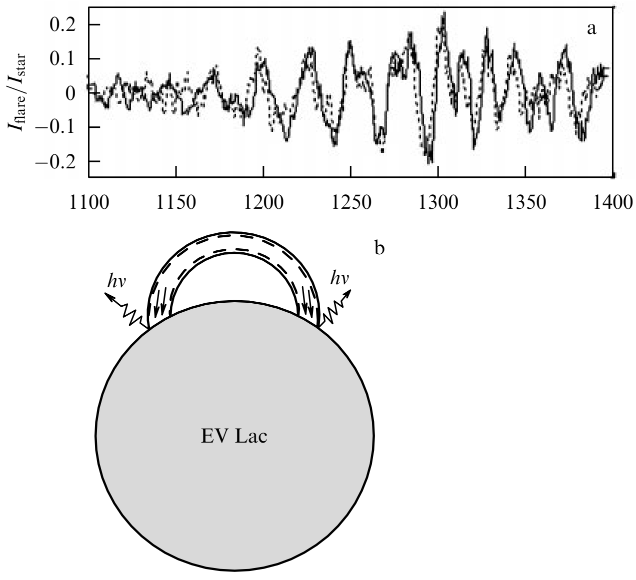

Figure 11. Oscillations of emission in the U-band (solid curve) and B-band (dotted curve) with a period $P \approx 13$ s in the flare on EV Lac on 11 September 1998 [90]. (b) Model of bremsstrahlung pulsations on EV Lac [91].

the loop footpoints is enforced by fluxes of high-energy electrons hitting the photosphere of the star. Given the presence of sausage oscillations in the loop, its loss cone varies periodically. This modulates electron fluxes precipitated towards the loop legs and, as a consequence, leads to oscillations in the emission from the loop footpoints [84]. From the model of the coronal magnetic mirror trap [84] one finds the relationship of the modulation depth with the parameter β: $\Delta \approx \beta$. Typical values of coronal loop lengths on red dwarfs vary from several stellar radii R_* to $l < 0.1 R_*$ [3, 92]. The radius of EV Lac equals $R_* = 0.39\, R_\odot$. Specifying the ratio $a/l = 0.1$, we get $\theta \approx \arctan(2.6 l/\pi a) \approx 76°$. Applying the method of coronal seismology, which was used above for solar flares, and taking $\tilde{r} \approx 2.6 \times 10^9$ cm, one gets the estimates of plasma temperature $T \approx 3.7 \times 10^7$ K, particle concentration $n \approx 1.6 \times 10^{11}$ cm^{-3}, and magnetic field induction $B \approx 320$ G for the flare loop of EV Lac.

3.3.4 Pulsations of X-ray emission and diagnostics of the flare on the star AT Mic. Based on data from the space observatory XMM-Newton, Mitra-Kraev et al. [93] succeeded in detecting quasiperiodic pulsations in the 0.2 – 12-keV X-ray band during a flare on 16 October 2000 on one of the components of binary red dwarf AT Mic (dM4.5e + dM4.5e). The pulsations had a period of about 750 s, relative modulation depth $\Delta \approx 0.15$, and a decay time of about 2000 s. Raassen et al. [94] have determined the plasma temperature for this flare on AT Mic to be $T = 2.4 \times 10^7$ K, based on data from XMM-Newton. Reference [94] proposed linking the detected emission pulsations with slow magneto-acoustic (SMA) oscillations of the flare loop, which have frequency $\omega \approx k_{||} c_s$ for $\beta \ll 1$. This allowed the characteristic loop length to be estimated as $l \approx 2.5 \times 10^{10}$ cm, which is comparable to the stellar radius $R_* = 3.3 \times 10^{10}$ cm. Reference [95] showed that the damping of SMA oscillations which modulate thermal X-ray emission of the flare loop was defined by the electron heat conductivity. Departing from this result, one finds an estimate of 3.2×10^{10} cm^{-3} for the number density of emitting plasma in the flare loop, whereas condition $\beta \ll 1$ sets the minimum magnitude of the flare magnetic field, $B > 100$ G. The excitation of loop SMA oscillations most likely follows a piston mechanism.

4. Plasma heating in coronal magnetic loops

4.1 Plasma heating in loops in the vicinity of sunspots

The problem of stellar corona heating remains a challenging one in astrophysics [96 – 99]. To heat the corona of the Sun to 10^6 K, a specific power of order 10^{-3} erg cm^{-3} s^{-1} is needed. X-ray data from RoSAT [14] indicate that coronae on late type stars have temperatures of $\approx 10^7 – 10^8$ K, which requires even more powerful sources of heating. With respect to coronal magnetic loops that permeate the entire space around sunspots, the proposed heating mechanisms can be subdivided into internal and external ones. The internal mechanisms transform the free energy of a magnetic loop into plasma heat content, as with Ohmic dissipation of currents flowing along the magnetic field inside the loops [100], tearing-instability [101], or magnetic energy dissipation in multiple microbursts that accompany reconnections of the magnetic field lines in the loops [102].

Ohmic dissipation of longitudinal currents requires anomalous resistance and, as a consequence, strong current filamentation, with current sheets about 5×10^2 cm thick. One can attribute evaporation of hot chromospheric plasma into the corona [103], resonant dissipation of Alfvén waves [104, 105], and cyclotron absorption of electromagnetic waves generated during flares [106] to external heating mechanisms relying on free energy supplied from outside.

Several years ago a stereoscopic analysis was undertaken of coronal magnetic loops observed with the aid of the Extreme Ultraviolet Imaging Telescope (EIT) aboard SOHO in the temperature range of 1.0 – 2.5 MK [107]. It was found that these loops have nearly invariable temperature over several height scales. A similar result was obtained in Ref. [108] by analyzing data coming from TRACE. Small temperature gradients lead to the result that radiative losses cannot be compensated by the electron heat conductivity. Accordingly, over the entire loop length the heating source has to be balanced with radiative losses, providing loop quasistationarity for at least several hours, as appears from observations. The plasma density in such loops drops exponentially with height. This indicates that the loops are approximately in hydrostatic equilibrium over several (1 – 3) height scales for the observation time interval. The heating function (the power of energy release per unit volume, going into plasma heating) must in this case also decrease exponentially with height, with the characteristic scale being one-half of the barometric scale for the plasma density. This happens because the radiative losses are proportional to the plasma concentration squared. The observational data did not reveal a correlation between the magnetic field and plasma heating function in the vicinity of loop footpoints. However, they permitted the detection of the quadratic dependence of heating function on the plasma gas pressure.

In this section we call attention to the fact that the quadratic dependence of heating rate on the pressure appears in dissipating diamagnetic currents in a plasma. We consider dissipation of diamagnetic currents in magnetic flux tubes, assuming that the plasma contains a small number of neutral atoms. In this case, a significant role is played by the Cowling dissipation [36] stemming from ion – atom collisions. The rate of Cowling dissipation is larger by many orders of magnitude than the dissipation rate due to classical conductivity linked to electron – ion collisions. This occurs because the Ampère force appearing in the presence of electric (in this case diamagnetic) currents sets the plasma in motion with respect to the neutral gas at a velocity which can be essentially higher than the relative velocity between electrons and ions in the current. Since the mass of ions exceeds by manyfold the mass of electrons, it becomes clear that the kinetic energy of plasma exceeds by many orders of magnitude that of electrons moving relative to ions. For ions and atoms with comparable masses, a significant part of the arriving energy is transformed into a chaotic one upon a single collision. The plasma is then heated as a result of slow dissipation of the loop magnetic field. If the gas-to-magnetic field pressure ratio $\beta = 8\pi p/B^2 \ll 1$, the rate of magnetic field dissipation proves to be $\beta^{-1} \gg 1$ times smaller than the plasma heating rate, i.e., heating proceeds without noticeably changing the magnetic field.

Under the high temperatures of a solar corona, a small fraction of neutral atoms is maintained owing to the presence of helium. It has a higher ionization potential than hydrogen and participate in an unforbidden, in contrast to hydrogen, dielectronic recombination, sustaining a relative mass of neutral helium atoms at the level of 10^{-5} for a temperature of 0.1 MK. This proves sufficient for maintaining a necessary plasma heating rate in coronal magnetic loops. The heating function turns out in this case to be dependent on altitude, with the characteristic scale being approximately one-half of that for the mean pressure, as the characteristic height scales for the helium partial pressure and mean plasma pressure differ approximately two-fold in hydrostatic equilibrium. As a mechanism filling the coronal loops with a dense plasma, Refs [57, 109] suggest the ballooning mode of flute instability developing in the chromospheric footpoints of coronal magnetic loops. The instability yields additional filamentation of plasma in the magnetic loop, which augments heating efficiency.

4.2 Basic equations

Consider a vertical, axisymmetric magnetic flux tube being in magnetohydrostatic equilibrium with the solar atmosphere. The equation of magnetohydrostatic balance between the pressure gradient, Ampère force, and gravity force takes the form (2.1) which is valid when the plasma velocity V is much less than the speed of sound, Alfvén velocity, and free-fall velocity.

A description of plasma heating and magnetic field dissipation in the tube is obtained starting from the generalized Ohm's law which, in the presence of neutral atoms in a plasma, is written out as [36, 55]

$$\mathbf{E} + \frac{1}{c}\,\mathbf{V}\times\mathbf{B} = \frac{c}{4\pi\sigma}\,\nabla\times\mathbf{B} - \frac{1}{4\pi en}\,\mathbf{B}\times(\nabla\times\mathbf{B}) - \frac{\nabla p_{\mathrm{e}}}{en} + \frac{F^2}{cnm_{\mathrm{i}}v'_{\mathrm{ia}}}\,\mathbf{B}\times\left[\frac{1}{8\pi}\times\left(\nabla\,\frac{m_{\mathrm{i}}}{m_{\mathrm{a}}}\,\mathbf{B}\times\mathbf{B}\right) - \left(1-\frac{m_{\mathrm{i}}}{2m_{\mathrm{a}}}\right)\rho\mathbf{g}\right]. \tag{4.1}$$

Equation (4.1) is based on equations of three-fluid magnetohydrodynamics for electrons, ions, and neutral atoms under the assumption that the relative density of the neutral component $F \ll 1$ and $\partial\mathbf{V}/\partial t = 0$. The variation of magnetic induction $\mathbf{B}$ resulting from the dissipation of currents in the plasma obeys the equation [110–113]

$$\frac{\partial\mathbf{B}}{\partial t} = \nabla\times(\mathbf{V}\times\mathbf{B}) + \frac{c^2}{4\pi\sigma}\,\nabla^2\mathbf{B} + \frac{F^2}{8\pi m_{\mathrm{a}}}\nabla \times\left\{\frac{1}{nv'_{\mathrm{ia}}}\,\mathbf{B}\times\left[\mathbf{B}\times(\nabla\times\mathbf{B})\right]\right\}. \tag{4.2}$$

The system of equations (2.1), (4.1), and (4.2) have to be supplemented with the equation for pressure [11]:

$$\frac{1}{\gamma-1}\,\frac{\partial p}{\partial t} = E_{\mathrm{h}} - E_{\mathrm{r}} - \frac{\partial}{\partial s}\left(kT^{5/2}\,\frac{\partial T}{\partial s}\right), \tag{4.3}$$

where $\gamma = c_p/c_v$ is the specific heat ratio, E_{h} is the plasma heating function, and E_{r} is the function of radiative losses. The last term on the right-hand side of Eqn (4.3) describes the electron heat conductivity, with k being the heat conductivity coefficient equal to

$$k = 0.92\times10^{-6}\ \mathrm{erg\ s^{-1}K^{-7/2}}, \tag{4.4}$$

and s the coordinate along the tube axis.

In principle, two different types of magnetic flux tubes are possible. The first one embraces tubes produced by 'raking' the background magnetic field by convective fluxes of photospheric plasma (see Section 2). The footpoints of such tubes are usually located at the nodes of several supergranulation cells, where converging horizontal convective flows are available. Such tubes are to be found far from sunspots and host large electric currents, up to 10^{12} A, emerging as a result of the interaction of a convective plasma flux with the tube's own magnetic field. In a vertical tube with the magnetic field $\mathbf{B}(0, B_\varphi, B_z)$, the components B_φ and B_z are frequently specified in the form suggested by Gold and Hoyle [114]. Magnetic flux tubes with longitudinal current can carry large nonpotential energy and serve as a source of energetic flares.

The second type consists of numerous magnetic flux tubes arising near sunspots as a result of filling thin, filament-like regions (stretched along lines of the spot's magnetic field) with a dense chromospheric plasma. Only a diamagnetic current arises in such magnetic flux tubes. It tends to weaken the magnetic field inside them by a magnitude corresponding to excessive gas pressure inside the tubes. It is likely that namely this types of magnetic flux tubes was observed in large numbers with TRACE around solar spots.

Assume, for the sake of definiteness, that the plasma pressure inside the vertical axisymmetric magnetic flux tube varies with the radial coordinate r in the following way:

$$p(r) = p_\infty + p_0\exp\left(-\frac{r^2}{a^2}\right), \tag{4.5}$$

where p_∞ is the plasma pressure outside the tube, $p_\infty + p_0$ is the pressure on the tube axis, and a is the tube radius. Projecting equation (2.1) in the radial direction, one obtains the dependence of tube's magnetic field induction on the radius:

$$B_z^2(r) = B_\infty^2 - 8\pi p_0\exp\left(-\frac{r^2}{a^2}\right), \tag{4.6}$$

where B_∞ is the z-component of the magnetic field outside the tube. The total electric current in the tube, which coincides in this case with the diamagnetic current, equals

$$j_\phi = j = \frac{c}{B_z}\,(\nabla p)_r = -\frac{2cp_0 r}{B_z a^2}\exp\left(-\frac{r^2}{a^2}\right), \tag{4.7}$$

where $(\nabla p)_r$ is the radial component of the pressure gradient. The data from SOHO and TRACE [107] show that the pressure within the loops staying in hydrostatic equilibrium is, by order of magnitude, 0.5–1.0 dyn cm^{-2} for loop footpoints, which is markedly higher than the values 6×10^{-2}–2×10^{-1} dyn cm^{-2} in the upper chromosphere [41]. Thus, below it well be assumed that $p_\infty \ll p(r)$. Projecting equation (2.1) on the z-axis and recalling that the density and pressure are linked by the relationship

$$\rho = \frac{\mu m_{\mathrm{H}}p}{k_{\mathrm{B}}T}, \tag{4.8}$$

where μm_{H} is the mean ion mass, and m_{H} is the hydrogen atom mass (for the solar atmosphere $\mu \approx 1.4$ for H : He = 10 : 1), one gets the dependence of pressure on altitude:

$$p = p_0\exp\left(-\int_0^z\frac{\mathrm{d}z}{\Lambda}\right), \tag{4.9}$$

where $\Lambda = k_{\mathrm{B}}T(z)/(\mu m_{\mathrm{H}}g)$ is the height scale for the pressure.

From the generalized Ohm's law (4.1) it follows that the plasma heating rate caused by current dissipation in the magnetic flux tube is given by

$$q_{\mathrm{j}}(r) = \left(\mathbf{E} + \frac{1}{c}\,\mathbf{V}\times\mathbf{B}\right)\mathbf{j} = \frac{c^2}{(4\pi)^2\sigma}\,(\nabla\times\mathbf{B})^2 + \frac{F^2}{32\pi^2 nm_{\mathrm{a}}v'_{\mathrm{ia}}}\,\big(\mathbf{B}\times(\nabla\times\mathbf{B})\big)^2. \tag{4.10}$$

The first term on the right-hand side (rhs) of equation (4.10) describes the dissipation of current $\mathbf{j} = (4\pi/c)\,\nabla\times\mathbf{B}$ in the magnetic flux tube via classical conductivity attributed to collisions of electrons with ions and atoms. The second term on the rhs of Eqn (4.10) exists only when neutral atoms are available in the plasma and describes the dissipation of diamagnetic currents furnished by ion–atom collisions. With regard to Eqns (2.1) and (4.7), the heating rate can be written as

$$q_{\mathrm{j}}(r)=\frac{c^2}{B_z^2\sigma}\,(\nabla p)_r^2+\frac{F^2}{2nm_{\mathrm{a}}\nu'_{\mathrm{ia}}}\,(\nabla p)_r^2\,, \tag{4.11}$$

where $(\nabla p)_r$ is the radial component of the gas pressure gradient. Assuming $p_\infty \ll p(r)$, we introduce the mean pressure inside the tube. Employing formula (4.5), one obtains

$$\bar{p}=\frac{1}{\pi a^2}\int_0^\infty p(r)\,2\pi r\,\mathrm{d}r=p_0\,. \tag{4.12}$$

Similarly, we introduce the mean (over tube cross section) rate of plasma heating:

$$q_{\mathrm{j}}=\frac{1}{\pi a^2}\int_0^\infty q_{\mathrm{j}}(r)\,2\pi r\,\mathrm{d}r\,.$$

Substituting the expression for $(\nabla p)_r$ in Eqn (4.11) and taking into account formula (4.5), one arrives at the expression for the mean rate of heating:

$$q_{\mathrm{j}}=\left(\frac{c^2}{B_z^2a^2\sigma}+\frac{F^2}{2nm_{\mathrm{a}}\nu'_{\mathrm{ia}}a^2}\right)p_0^2\,. \tag{4.13}$$

Relationship (4.13) seemingly reflects the actual dissipation scheme as data from TRACE satellite [115] showed that the heating rate of coronal magnetic loops is indeed proportional to the square of gas pressure within the loops.

Let us compare heating rates resulted from the dissipation of diamagnetic currents through ion-atom collisions (Cowling conductivity) and classical conductivity arising from collisions of electrons with ions and atoms. Setting $\nu'_{\mathrm{ia}}=m_{\mathrm{a}}n_{\mathrm{a}}\sigma_{\mathrm{ia}}V_{\mathrm{Ti}}/(m_{\mathrm{a}}+m_{\mathrm{i}})$, $V_{\mathrm{Ti}}=(k_{\mathrm{B}}T/m_{\mathrm{i}})^{1/2}$, and $n_{\mathrm{a}}=nm_{\mathrm{i}}F/m_{\mathrm{a}}$ and supposing that for temperatures $T\geqslant 5\times10^5$ K the cross section of ion – atom collisions is expressed as [116]

$$\sigma_{\mathrm{ia}}=\frac{3.3\times10^{-10}\,n}{T}\,[\mathrm{cm}^2]\,, \tag{4.14}$$

we infer for the ratio R of the second to first terms on the rhs of Eqn (4.13):

$$R=\frac{F^2\omega_{\mathrm{e}}\omega_{\mathrm{i}}}{8\nu_{\mathrm{ei}}\nu'_{\mathrm{ia}}}=4\times10^{14}\,\frac{FB_z^2T^2}{n^2}\,. \tag{4.15}$$

Here, we presumed that the main contributor to the neutral plasma component at high coronal temperatures is, as will be explained further, ^{4}He for which $m_{\mathrm{a}}=4m_{\mathrm{i}}$. Setting $n=2\times10^9$ cm^{-3} and $B_z=200$ G for loops with temperature $T=(1-2.5)\times10^6$ K, observed with TRACE, we find for the ratio of heating rates: $R=2.8\times10^{13}F$.

As will be shown in Section 4.3, the relative mass of neutral atoms at the temperature of 1.5×10^6 K equals $F=2.6\times10^{-5}$, which gives for the ratio of heating rates $R=10^8$. For $T=5\times10^6$ K, one has $F=0.5\times10^{-5}$ and correspondingly $R=1.4\times10^8$. In other words, even for coronal temperatures $(1-5)\times10^6$ K, the rate of plasma heating mediated by ion – atom collisions exceeds by eight orders of magnitude the heating rate attributed to classical electron conductivity. Neglecting the first term on the rhs of formula (4.13), for plasma heating function, i.e., the amount of heat released in 1 cm^3 of plasma per second via the dissipation of diamagnetic currents, one can write out the relationship

$$E_{\mathrm{h}}=\frac{F^2}{2nm_{\mathrm{a}}\nu'_{\mathrm{ia}}a^2}\,p_0^2\,. \tag{4.16}$$

For chromospheric conditions ($T\leqslant10^5$ K), the number of neutral atoms in the plasma is predominantly determined by the processes of hydrogen ionization and recombination. Hence, $m_{\mathrm{a}}=m_{\mathrm{i}}$ and the effective frequency of ion – atom collisions becomes [116] $\nu'_{\mathrm{ia}}=4.5\times10^{-11}nFT^{1/2}$ [s^{-1}]. Under coronal conditions ($T\geqslant5\times10^5$ K), the number of neutral atoms is governed by the processes of hydrogen ionization and recombination. Thus, $m_{\mathrm{a}}=m_{\mathrm{i}}$ and the effective collision frequency $\nu'_{\mathrm{ia}}=0.75\times10^{-6}nFT^{-1/2}$ [s^{-1}].

4.3 Heating function for coronal plasma

Let us compute the heating function E_{h} with due regard for the specifics of the solar corona. As already mentioned, at sufficiently high temperatures ($T\leqslant10^5$ K) the relative density of neutral atoms in the corona $F=n_{\mathrm{a}}m_{\mathrm{a}}/(n_{\mathrm{a}}m_{\mathrm{a}}+n_{\mathrm{i}}m_{\mathrm{i}})\approx n_{\mathrm{a}}m_{\mathrm{a}}/n_{\mathrm{i}}m_{\mathrm{i}}$ is primarily determined by the processes of helium ionization and recombination. For one thing, the helium ionization potential, $\varepsilon_{\mathrm{i}}(\mathrm{HeI})=24.6$ eV, is almost twice as high as that of hydrogen, $\varepsilon_{\mathrm{i}}(\mathrm{H})=13.6$ eV. Furthermore, in contrast to hydrogen, the dielectron recombination is not forbidden for helium. Its rate exceeds by nearly two orders of magnitude the rate of radiative recombination for hydrogen ions at coronal temperatures [117]. From the equation of ionization balance we get [118]

$$S(T)\,n_{\mathrm{a}}(\mathrm{HeI})\,n_{\mathrm{e}}=\alpha(T)\,n_{\mathrm{i}}(\mathrm{HeII})\,n_{\mathrm{e}}\,, \tag{4.17}$$

where $n_{\mathrm{a}}(\mathrm{HeI})$ is the concentration of atoms of nonionized helium, $n_{\mathrm{i}}(\mathrm{HeII})$ is the concentration of singly ionized helium, $S(T)$ is the rate of ionization, $\alpha(T)$ is the rate of recombination, and n_{e} is the electron concentration. For the ionization rate in the temperature interval $0.02\leqslant k_{\mathrm{B}}T_{\mathrm{e}}/\varepsilon_{\mathrm{i}}\leqslant100$, the following expression can be utilized [119]:

$$S(T)=2.56\times10^{-11}\,\frac{T^{1/2}}{1+T/(1.71\times10^6)}\times\exp\left(-\frac{2.85\times10^5}{T}\right)[\mathrm{cm}^3\,\mathrm{s}^{-1}]\,. \tag{4.18}$$

For the rate of dielectron recombination of singly ionized helium we have [117, 120]

$$\alpha(\mathrm{HeII})=\frac{3.05\times10^{-3}}{T^{3/2}}\exp\left(-\frac{4.74\times10^5}{T}\right)[\mathrm{cm}^3\,\mathrm{s}^{-1}]\,. \tag{4.19}$$

Equations (4.17) – (4.19) yield

$$F=\frac{m_{\mathrm{a}}\alpha(T)\,n_{\mathrm{i}}(\mathrm{HeII})}{m_{\mathrm{i}}S(T)\,n_{\mathrm{e}}}\approx\frac{m_{\mathrm{a}}\alpha(T)\,p(\mathrm{HeII})}{m_{\mathrm{i}}S(T)\,p}\,, \tag{4.20}$$

where in passing to the last equality we took into account that the helium partial pressure $p(\mathrm{HeII})\approx2n_{\mathrm{i}}(\mathrm{HeII})\,k_{\mathrm{B}}T$, and the total pressure $p\approx2n_{\mathrm{e}}k_{\mathrm{B}}T$, because the degree of ionization is high. Recognizing that the helium partial pressure decreases exponentially with altitude on the height scale $\Lambda_{\rm He} = k_{\rm B}T/4m_{\rm i}g$, whereas the total pressure has the height scale $\Lambda = k_{\rm B}T/\mu m_{\rm i}g$, where $\mu \approx 1.4$, we finally arrive at the dependence of relative mass of neutral atoms on the temperature and height in the solar corona:

$$F(T,z) = 4\times10^7\,\frac{1+T/(1.71\times10^6)}{T^2}\times\exp\left(-\frac{1.89\times10^5}{T}\right)\exp\left(-\frac{1.86z}{\Lambda}\right). \quad (4.21)$$

In formula (4.21) we assumed that at the corona base ($z=0$) the ratio of helium partial pressure to the total pressure equals $p(\mathrm{HeII})/p \approx 0.1$, which does not contradict observational data.

As follows from formula (4.21), for temperatures $T = (0.5-1.0)\times10^5$ K, the fraction of neutral helium atoms in the solar corona reaches $F_{\rm HeI}(z=0) \approx 10^{-2.5}-10^{-4.5}$. The relative content of neutral hydrogen atoms at the same temperatures ranges $F_{\rm H}(z=0) \approx 10^{-3.8}-10^{-4.9}$, i.e., it is essentially smaller.

Thus, helium plays the main role in the dissipation of diamagnetic currents in the coronal plasma at high temperature. The most efficient dissipation channel here operates through ion–atom collisions, delegating the decisive role to Cowling conductivity.

4.3.1 Heating function for coronal loops. Substituting $v'_{\rm ia}$ for $T \geqslant 5\times10^5$ K in formula (4.16) and putting $p_0 = 2n_{\rm e}k_{\rm B}T$, we get the following expression for the function of plasma heating due to dissipation of diamagnetic currents in coronal magnetic loops:

$$E_{\rm h}(T,z) = Q_{\rm ia}(T)\,\exp\left(-\frac{1.86z}{\Lambda(T)}\right), \quad (4.22)$$

where

$$Q_{\rm ia}(T) = \frac{2.8T^{1/2}}{a^2}\left(1+\frac{T}{1.71\times10^6}\right)\exp\left(-\frac{1.79\times10^5}{T}\right). \quad (4.23)$$

The heating function does not depend on the plasma density in the flux tube, but depends on the temperature, the tube radius, and altitude. The scale for the variation of heating function with height is equal to approximately half of the pressure variation scale. Consequently, if the temperature is approximately constant inside the loop (which is confirmed by the TRACE data), the heating function depends on the height nearly in the same manner as the function of radiation losses, which is proportional to the electron density squared. Thus, if the electron heat conductivity is small, which is true for loops with temperatures ranging $(1.0-2.5)\times10^6$ K [106], the heating function can be in equilibrium with the function of radiation losses over a significant height interval, providing quasistationarity of a loop. A slight difference in the height dependences of heating function and radiation loss function can be 'smoothed' by the electron heat conductivity. Over the temperature range $10^{5.75} \leqslant T \leqslant 10^{6.3}$ K, the radiative cooling of plasma because of optical emission can be approximated by the function [121]

$$E_{\rm r} = n_{\rm e}^2 Q(T)\,[\mathrm{erg\ cm^3\ s^{-1}}], \quad (4.24)$$

where $Q(T) = 10^{-21.94}$. The balance between heating and radiation losses, namely

$$Q_{\rm ia}(T)\,\exp\left(-\frac{1.76z}{\Lambda(T)}\right) \approx Q(T)\,n_{\rm e}^2(0)\,\exp\left(-\frac{2z}{\Lambda(T)}\right) \quad (4.25)$$

can be achieved if the tube is sufficiently thin, viz.

$$a^2 \leqslant \frac{2.4\times10^5 T^{1/2}}{n_{\rm e}^2 Q(T)}\left(1+\frac{T}{1.76\times10^6}\right)\times\exp\left(-\frac{1.89\times10^5}{T}\right). \quad (4.26)$$

For mean values of $T = 1.2\times10^6$ K and $n_{\rm e} = 2\times10^9$ cm^{-3}, typical of loops observed by TRACE, condition (4.26) gives $a \leqslant 10^6$ cm. If $T = 5\times10^6$ K, and $n_{\rm e} = 3\times10^9$ cm^{-3}, which is common for hot loops observed by Yohkoh satellite in soft X-rays, formula (4.26) gives $a \leqslant 2\times10^6$ cm.

Accordingly, the dissipation of diamagnetic currents can provide the heating of loops with the observed thickness $(2-5)\times10^8$ cm if they are composed of an ensemble of thin hot 'filaments' $(1-2)\times10^6$ cm thick. It is necessary to note that attempts to interpret the TRACE data led some authors to a similar conclusion that a bundle of hot thin filaments is possibly confined within the observed coronal magnetic loops [107, 108].

In accordance with equation (4.3), the characteristic time $t_{\rm h}$ of plasma heating can be estimated in the following manner:

$$t_{\rm h} = \frac{p}{(\gamma-1)\,E_{\rm h}}\,. \quad (4.27)$$

Putting $\gamma = 5/3$, $T = 1.2\times10^6$ K, $n_{\rm e} = 2\times10^9$ cm^{-3}, and $a = 10^6$ cm, we get $p = 0.8$ dyn cm^{-2}, and $E_{\rm h} = 0.3\times10^{-3}$ erg cm^{-3} s^{-1}, which yields the heating time $t_{\rm h} = 1.9\times10^3$ s (about 32 min), approximately equal to the time of radiation losses, which reaches 40 min on average according to the estimates of Ref. [115] for coronal magnetic loops observed by TRACE.

4.3.2 Dissipation of a magnetic field. Eventually, plasma heating in a coronal magnetic loop owing to diamagnetic current dissipation occurs because the loop magnetic field is dissipated. One may become convinced of this fact by forming a scalar product of equation (4.2) with $\mathbf{B}$ and integrating the result over the tube volume with account for formulas (4.5) and (4.6). Putting in our case $V = 0$, we get as a result:

$$\int_0^\infty \frac{\partial}{\partial t}\,\frac{B_z^2}{8\pi}\,2\pi r\,\mathrm{d}r = -\int_0^\infty q_{\rm j}(r)\,2\pi r\,\mathrm{d}r\,, \quad (4.28)$$

where $q_{\rm j}(r)$ is defined by expression (4.11). In other words, the dissipation rate of the magnetic field in the tube is equal to the plasma heating rate taken with the opposite sign. Although the absolute values of the dissipation and heating rates coincide, the dissipation time of the magnetic field for $\beta = 8\pi p/B^2 \ll 1$ proves to be $\beta^{-1} \gg 1$ times longer than the plasma heating time. As follows from Eqn (4.28), the decay time of the magnetic field owing to the dissipation of diamagnetic currents is given by

$$t_B = \frac{\gamma-1}{\beta}\,t_{\rm h}\,. \quad (4.29)$$

By way of example, at $\beta = 10^{-2}$ formula (4.29) yields $t_B = 35.5$ h for the magnetic field dissipation time, in contrast to the heating time $t_{\rm h} = 32$ min.

4.4 Flute instability and the filamentation of magnetic loops

Filling a region of a potential magnetic field in the vicinity of sunspots with plasma, which brings about the appearance of magnetic loops with enhanced plasma density, can proceed through the build-up of a ballooning mode of flute instability in chromospheric bases of magnetic spots [122]. This instability develops at the boundary between the sunspot penumbra, where $\beta \ll 1$, and the ambient chromosphere, where $\beta \leqslant 1$. In this region, the magnetic field expands so that its field lines become curved, with the curvature directed from the neighboring chromosphere toward the spot. The radius of magnetic field line curvature takes a value on the order of the height scale of the inhomogeneous atmosphere:

$$R_{\rm c} \approx \frac{k_{\rm B} T}{\mu m_{\rm i} g} \,. \tag{4.30}$$

Because of magnetic field curvature, there appears a centrifugal force

$$\mathbf{f}_{\rm c} = \frac{2 n k_{\rm B} T}{R_{\rm c}^2}\, \mathbf{R}_{\rm c} \tag{4.31}$$

acting on a cubic centimeter of plasma with density $\rho \approx (n + n_{\rm a})\, m_{\rm i}$. The effective centrifugal acceleration exerting on the chromospheric plasma around the spot is expressed as

$$\mathbf{g}_{\rm c} = \frac{\mathbf{f}_{\rm c}}{\rho} = \frac{2 k_{\rm B} T}{m_{\rm i} R_{\rm c}^2}\, \frac{n}{n + n_{\rm a}}\, \mathbf{R}_{\rm c} \,. \tag{4.32}$$

Substituting formula (4.30) into Eqn (4.32) we obtain

$$g_{\rm c} = 2g\, \frac{n}{n + n_{\rm a}} \,. \tag{4.33}$$

The condition for developing the ballooning instability has the form

$$g_{\rm c} - g \cos\theta > 0 \,, \tag{4.34}$$

where θ is the angle between the direction of the radius of curvature $\mathbf{R}_{\rm c}$ and the vertical. When $\mathbf{R}_{\rm c}$ and $\mathbf{g}$ are approximately perpendicular, the unfolding time of the ballooning mode of flute instability is as follows:

$$\tau_{\rm b} = \frac{1}{2} \left(\frac{\lambda}{\pi g} \right)^{1/2} \left(\frac{n}{n + n_{\rm a}} \right)^{-1/2} , \tag{4.35}$$

where λ is the perturbation wavelength. Estimate (4.35) corresponds to the most unstable case in which the wave vector of perturbation is perpendicular to the magnetic field direction [11]. In the case of $n_{\rm a} \ll n$, one finds

$$\tau_{\rm b} \approx 2 \times 10^{-3} (\lambda\, [\mathrm{cm}])^{1/2}\, [\mathrm{s}] \tag{4.36}$$

and perturbations with the wavelength $\lambda \approx \Lambda \approx 3 \times 10^8$ cm at $T = 10^5$ K grow for about 35 s. The perturbation wavelength $\lambda \approx \Lambda$ can be regarded as the maximum wavelength for the ballooning mode of flute instability. With it, magnetic loops with a thickness of about $(3-6) \times 10^8$ cm, observed with the help of SOHO/EIT and TRACE, can be associated. It is, however, seen from estimate (4.36) that short-wave perturbations grow faster. This also means that an initial long-wave perturbation has to split up into smaller scales.

A minimum instability scale can be linked with plasma heating within the flutes because of the dissipation of diamagnetic currents with the scale $\lambda_{\min}$. If the heating time $t_{\rm h}$ of a plasma in a flute of thickness $\lambda_{\min}$ is essentially smaller than the instability development time for a flute with wavelength $\lambda_{\min}$, the plasma with augmented pressure will have time to escape from the flute along magnetic field lines under the action of a pressure gradient created due to heating. As a result, the instability on this scale will disappear. Hence, it is possible to assume that the minimum thickness of flutes is determined from the condition that the times of heating and flute instability growth are equal, thus yielding

$$\lambda_{\min} = \left(\frac{F^2 p}{n m_{\rm a} v_{\rm ia} \sqrt{g}} \right)^{2/3} . \tag{4.37}$$

For chromospheric regions with the parameters $T = 8 \times 10^3$ K, $n = 1.25 \times 10^{10}$ cm^{-3}, $p = 0.17$ dyn cm^{-2}, $F = 0.75$, and $n_{\rm a} = 4 \times 10^{10}$ cm^{-3} [123], we find that $\lambda_{\min} \geqslant 3 \times 10^5$ cm. Comparing values of maximum, $\lambda_{\max} \approx 3 \times 10^8$ cm, and minimum, $\lambda_{\min} \approx 3 \times 10^5$ cm, thicknesses of flute perturbations and taking into account that in flutes with thickness $\lambda_{\min}$ effective plasma heating occurs, it is possible to assume that the observed coronal magnetic loops $(3-6) \times 10^8$ cm in thickness are filled with thin hot magnetic filaments $3 \times 10^5 - 3 \times 10^6$ cm thick. To observe such structures, a space resolution of $0.1''$ is required.

The assumption about the important role played by filamentation of magnetic structures in heating solar and stellar coronae was formulated by Litwin and Rosner [124]. In addition, Ref. [108] showed that nearly homogeneous temperature distributions along coronal magnetic loops, recorded by the space observatory TRACE, can be explained by the presence of subsecond structures aligned with the magnetic field within the loops. Reference [107] made an analysis of 41 loops observed with TRACE and reported good agreement of the observed isothermality of the loops with the existence of internal filament structure.

5. Acceleration of electrons in current-carrying magnetic loops

5.1 Observational data and possible mechanisms of acceleration

A significant part of the energy in stellar flares is released in the form of high-energy particles. For instance, in solar flares electrons with an energy of 20 – 200 keV carry up to 50% of the flare energy, namely $\sim 5 \times 10^{31}$ erg. The dominant portion of electrons and ions in solar flares is accelerated to energies of 100 keV and 100 MeV, respectively [125], and causes hard X-ray and gamma emission in lines. Furthermore, gamma emission in continuum and sometimes observed emission from neutral pions indicate that the energy of electrons and ions in flares may reach 10 MeV and 1 GeV, respectively. If one conjectures that hard X-ray emission from flares is the result of bremsstraglung from fast electrons in the chromosphere (thick target model [126]), an impulsive solar flare has to produce about 10^{37} electrons per second with an energy in excess of 20 keV for 10 – 100 s. This implies that the energy release rate in the form of accelerated electrons amounts to $\dot{E}_e \approx 3 \times 10^{29}$ erg s^{-1} over 100 s, which adds up to a total energy of $E_e(> 20$ keV$) \approx 3 \times 10^{31}$ erg for the total number $N_e(> 20$ keV$) \approx 10^{39}$ of accelerated electrons.

The requirements for the rate of electron acceleration can be somewhat relaxed if one assumes that the spectrum of hard X-ray radiation with energies less than 30 keV is contributed by hot ($\sim 3 \times 10^7$ K) plasma, and radiation with higher energies is generated by fast electrons having a power-law energy spectrum. This makes up the contents of the hybrid (thermal/nonthermal, T/NT) model [127]. In this paradigm, the necessary rate of producing electrons with energies $E_e > 20$ keV drops to $\dot{N}_e \approx 2 \times 10^{35}$ s^{-1} for a process lasting approximately 100 s. This sums up to $N_e(> 20$ keV$) \approx 2 \times 10^{37}$, $\dot{E}_e(> 20\,\text{keV}) \approx 6 \times 10^{27}\,\text{erg}\,\text{s}^{-1}$, and $E_e(> 20$ keV$) \approx 6 \times 10^{29}$ erg.

A variety of acceleration mechanisms has been proposed to explain the generation of fast particles by flares. Very roughly, they can be split into three major classes: (1) stochastic acceleration by waves (the Fermi mechanism of the second kind); (2) acceleration by shock waves, and (3) direct acceleration in quasistationary electric (DC) fields. Apart from these, a betatron mechanism is sometimes invoked (for example, for collapsing magnetic loops [128, 129]), as is a mechanism of magnetic pumping [130].

Keeping in mind the correlation between flares and coronal magnetic loops, let us consider the acceleration of electrons in large-scale electric fields induced by the convective motions of photospheric plasma at the footpoints of a coronal magnetic loop (it is undoubtedly recognized that other acceleration mechanisms can also be involved in the solar corona). Large-scale electric fields are established in coronal magnetic loops when loop footpoints reside at nodes of several supergranulation cells. In this case, converging plasma fluxes interact with the magnetic field in the loop footpoints and generate an electric field of charge separation, capable of efficiently accelerating particles under certain conditions. A loop may store a fairly large amount of energy, up to $10^{32} – 10^{33}$ erg, and furnish the energy release of an energetic flare. This energy is contained in a nonpotential part of the magnetic field linked to the existence in the loop of an electric current with a magnitude of up to 3×10^{12} A, the current generated by photospheric convection and flowing along the loop [22, 37].

5.2 The region of acceleration: Is it the chromosphere or corona?

In order to provide for the fluxes of fast electrons observed in impulsive flares, a sufficiently large number of accelerated particles should be available. What serves as their pool if they are accelerated in flare magnetic loops? The total number of electrons in a flare loop with a plasma density of 10^{10} cm^{-3}, cross-section area 10^{18} cm^2, and length $(1-5) \times 10^9$ cm amounts to $(1-5) \times 10^{37}$. In view of the fact that any sensible mechanism of acceleration in a plasma provides for the acceleration of only a small fraction of particles, it is clear that the estimated total number of electrons contained in the coronal part of the flare loop is far from sufficient to ensure the necessary supply of particles even in the most favorable case of the hybrid model ($\sim 2 \times 10^{37}$ electrons).

A magnetic loop comprises two important regions which can, in principle, supply particles to be accelerated in necessary numbers. The first region is the neighborhood of loop footpoints located in the chromosphere. In the chromospheric part of the loop, the column extending from the temperature minimum to the transition region between the chromosphere and corona contains about 5×10^{40} particles if the loop cross-section area in this region is assumed to be $\sim 10^{18}$ cm^2. If acceleration takes place in the chromospheric part of the loop, then this number of particles is more than sufficient to cover the needed number of electrons to be accelerated.

The second possibility of enriching the flare magnetic loop with particles occurs when it interacts with a prominence [37, 38]. In this case, the flare process can be triggered by a flute instability developing in the loop top and bringing the dense plasma of the prominence into the current channel of the magnetic loop. The number of particles supplied by the prominence in a flare time $t_f \sim 100$ s can be estimated as $N \approx 2\pi a r_f n_p V_p t_f$, where r_f is the thickness of the prominence tongue penetrating into the current channel, $a \approx 10^8$ cm is the half thickness of the loop, $n_p \approx 10^{12}$ cm^{-3} is the plasma concentration in the protuberance, and $V_p \approx V_{Ti} \approx 2 \times 10^6$ cm s^{-1} is the characteristic velocity of plasma inflow into the loop current channel. It is approximately equal to the thermal velocity of ions at the temperature of prominence matter reaching approximately 5×10^4 K. These values of the parameters yield $N \approx 3 \times 10^{38}$. This number is about one order of magnitude larger than required by T/NT model but remains several times smaller that the number required by the nonthermal model of a thick target. Hence follows the conclusion that the chromospheric part of the coronal loop constitutes the preferred acceleration site capable of satisfying the demand for particles for the most energetic flares. For flares with moderate energy release, the region of acceleration can be confined to the vicinity of the loop top where the necessary pool of particles is furnished by a plasma flux from the protuberance (if any).

It is worth noting that the acceleration region near the coronal loop top is also considered in the model of a collapsing magnetic trap [128, 129]. This model, however, provides only a very limited flux of injected electrons, as a high-temperature current sheet located at the magnetic loop top can accelerate not more than $10^{28} – 10^{30}$ electrons per second.

5.3 Fluxes of electrons accelerated in the loop electric field

One of the most efficient ways to accelerate a particle in the region of flare energy release is achieved through the direct action of an electric field. The large-scale electric field **E** of the flare magnetic loop can play this role. In this case, it is essential that if a magnetic field **B** is present in a plasma, such that $|\mathbf{B}| > |\mathbf{E}|$, the particles will only be accelerated by the projection of the electric field onto the magnetic field, $E_{||} = \mathbf{EB}/B$. If $E_{||}$ is weaker than the Dreicer field $E_D = e\Lambda\omega_p^2/V_T^2$, the process of acceleration (escaping) involves only electrons with velocities $V > (E_D/E_{||})^{1/2} V_T$, where V_T is the thermal velocity of electrons, Λ is the Coulomb logarithm, and ω_p is the Langmuir frequency. The kinetic theory leads to the following formula for the production rate of escaping electrons [131]:

$$\dot{N}_e = 0.35 n \nu_{ei} V_a x^{3/8} \exp\left(-\sqrt{2x} - \frac{x}{4}\right), \tag{5.1}$$

where $x = E_{\rm D}/E_{||}$, $V_{\rm a}$ is the volume of the acceleration region, $\nu_{\rm ei} = (5.5n\Lambda)/T^{3/2}$ is the effective frequency of electron–ion collisions, n is the electron concentration in the plasma, T is the temperature, and Λ is the Coulomb logarithm. In the coronal part of a magnetic loop with rather large electric currents, $I = 10^{12}$ A, and typical parameters $n = 10^{10}$ cm^{-3}, a half thickness $a = 5 \times 10^8$ cm, and $T = 10^6 - 10^7$ K, the electric field resulting from the finite plasma conductivity is too weak to impart any significant acceleration ($x = E_{\rm D}/E_{||} > 200$). The strongest electric fields are generated at footpoints of the magnetic loop through the effective charge separation caused by the convective transport of photospheric matter into the flux tube and the difference in magnetization between electrons and ions. In a vertical cylindrical tube with a radially converging plasma flow (this setup will serve to approximate the part of the actual tube located close to the photospheric footpoints), only a radial component of the electric field of charge separation exists. This component turns out to be perpendicular to the magnetic field of a stationary tube (B_φ, B_z), implying that acceleration by the charge separation field is absent in stationary conditions. Acceleration does appear when the magnetic field in the tube is deformed so that, for instance, a radial component B_r emerges. In this case, the projection of the electric field onto the direction of the magnetic field becomes [21]

$$E_{||} \approx \frac{1-F}{2-F}\,\frac{\sigma V_r B^2}{enc^2(1+\alpha B^2)}\,\frac{B_r}{B}\,. \tag{5.2}$$

Here, the radial component of the magnetic field $B_r \ll B$, $F = n_{\rm a}m_{\rm a}/(n_{\rm a}m_{\rm a} + nm_{\rm i})$ is the relative density of neutral particles, $\sigma = e^2 n/m_{\rm e}(\nu'_{\rm ei} + \nu'_{\rm ea})$ is the Coulomb conductivity, $\alpha = \sigma F^2/(2-F)\,c^2 nm_{\rm i}\nu'_{\rm ia}$, ν'_{jk} is the effective collision frequency of a particle of kind j with a particle of kind k, and V_r is the radial component of the velocity of convective plasma motion at the loop footpoint. Acceleration of particles by the charge separation field can take place, for instance, when flute instability develops at the magnetic flux tube footpoint and a plasma tongue protruding into the current channel with speed V_r is nonuniform with height. In this case, it can be shown that the radial component of the magnetic field, viz.

$$B_r = B\,\frac{\partial}{\partial z}\int_0^t V_r(t')\,{\rm d}t'\,, \tag{5.3}$$

is generated, so that there appears the electric field $E_{||}$ accelerating the particles. The magnitude of $E_{||}$ increases as the magnetic loop footpoints become hotter, as heating leads to an increase in σ and a decrease in α. Simultaneously, the relative density of neutral particles F drops. If warming is so strong that ionization is nearly complete ($F \ll 1$), one can consider that $\alpha B^2 \ll 1$. In this limit, formula (5.2) simplifies as

$$E_{||} \approx \frac{1}{2}\,\frac{V_r}{c}\,B\left(\frac{\omega_{\rm e}}{\nu'_{\rm ei}}\right)\frac{B_r}{B}\,, \quad \alpha B^2 \ll 1\,. \tag{5.4}$$

In the opposite limit, formula (5.2) reduces to

$$E_{||} \approx \frac{1-F}{F^2}\,\frac{m_{\rm i}V_r\nu'_{\rm ia}}{e}\,\frac{B_r}{B}\,, \quad \alpha B^2 \gg 1\,. \tag{5.5}$$

It should be mentioned that for $V_r < 0$ (the convective flux is converging into the tube) the field component $E_{||}$ is directed downwards and accelerates electrons toward the corona, and ions toward the photosphere, i.e., the high-energy electrons and ions are driven to different footpoints of the loops. This leads to an arrangement in which sources of gamma emission, produced by high-energy ions, and sources of hard X-rays, generated by fast electrons, are spatially separated. Such separation of sources of gamma (line 2.223 MeV) and X-ray (150–200 keV) emissions was registered, for example, by the space observatory RHESSI [132] for the flare on 23 July 2003.

In the case of $\alpha B^2 \gg 1$, the ratio $E_{\rm D}/E_{||}$ is expressed by the formula

$$\begin{aligned}\frac{E_{\rm D}}{E_{||}} &= 7.7 \times 10^{-5}\,\frac{n^2}{B^2 V_r T^{5/2}}\left(\frac{\Lambda}{20}\right)^2\frac{B}{B_r}\\ &= 2.6\left(\frac{n}{10^{15}}\right)^2\left(\frac{B}{10^3}\right)^{-2}\left(\frac{V_r}{3\times10^4}\right)^{-1}\\ &\times\left(\frac{T}{10^6}\right)^{-5/2}\left(\frac{\Lambda}{20}\right)^2\frac{B}{B_r}\,.\end{aligned} \tag{5.6}$$

Noteworthy is the strong dependence of the ratio $E_{\rm D}/E_{||}$ on the temperature and magnetic induction, which can vary in wide limits in the acceleration region. From formula (5.6) it follows that at $B_r \approx 0.1B$ the accelerating field can reach the magnitudes of the Dreicer field or even higher if the footpoints are heated to a temperature of 3.5×10^6 K. In this case, all the electrons are involved in the escaping regime and the electric field strength reaches 17 V cm^{-1}. This allows the particles to be accelerated to a limiting energy of about 1 GeV over the length scale of $\sim 10^8$ cm. Particular aspects of electron acceleration in super-Dreicer fields were considered by Litvinenko [133].

Extremal electric fields are only plausible for maximum possible magnetic fields of $\sim 10^3$ G and strongly heated photospheric footpoints of the magnetic loop on the Sun, which is certainly far from realized in all flares. Their feasibility, however, demonstrates the potential of current-carrying magnetic loops in effectively accelerating particles. If acceleration proceeds in the chromospheric loop footpoints, the rate of high-energy electron production will exceed 10^{35} electrons per second. This is sufficient for the T/NT model if we assume that in the acceleration region $n = 10^{11}$ cm^{-3}, the tube radius $a = 10^8$ cm, $T = 10^5$ K, and the vertical size of the acceleration region $h = 10^8$ cm. In this case, $E_{\rm D}/E_{||} = 26$, $E_{||} = 2.15 \times 10^{-3}$ V cm^{-1}, and the energy of the major portion of accelerated electrons reaches 200 keV.

5.4 Pulsed and pulsating regimes of acceleration

The appearance of a radial component of the magnetic field in a loop footpoint, where a strong electric field of charge separation is localized, can be caused, apart from the development of flute instability, also by the excitation of natural oscillations in the magnetic loop. The acceleration process is apparently of a pulsed character in the former case because of the aperiodic nature of the flute instability. In the latter case, a pulsating regime of acceleration is possible. It is often manifested in the form of quasiperiodic sequences of type-III radiobursts developing after flares.

5.4.1 Pulsed acceleration. A magnetic flux tube inflates on leaving the photosphere for the chromosphere to accommodate a drop in the external pressure. The magnetic field lines become curved there with the curvature pointing inside the flux tube. If condition (4.34) is satisfied, a flute instability develops in a ballooning mode with a characteristic time (4.36) of about 35 s. Within this time interval, the plasma surrounding the flux tube penetrates inside it, generating the radial component of the magnetic field. This ensures nonzero projection of the charge separation electric field onto the magnetic field, which serves as the cause of particle acceleration. The time interval given by formula (4.36) can in the first approximation be taken as a characteristic duration of the impulsive phase of acceleration. The factor finally arresting the acceleration process can be a decrease in the radial component of convection velocity resulting from an increase in the gas pressure inside the tube as the flare process develops, or the halt of the flute of external plasma penetrating into the magnetic loop. It should be noted that this time agrees on the order of magnitude with the duration of single impulsive flares (10 – 100 s). For plasma parameters in the acceleration region that were specified in Section 5.3, the total number of electrons accelerated in the footpoints of the current-carrying magnetic flux tube during the time interval τ_b amounts to $N_e(> 200\ \mathrm{keV}) \approx \dot{N}_e \tau_b \approx 3.5 \times 10^{36}$. This is quite sufficient to explain, in the framework of the T/NT model, the observed efficiency of the acceleration mechanism of hard X-ray emission generation in impulsive solar flares [127].

Data on the linear polarization of hard X-ray emission from solar flares, obtained with the satellite KORONAS-F [the Russian abbreviation for complex orbital near-earth observations of solar activity (photon)] also point to the acceleration of electrons in pulsed electric fields rather than to stochastic mechanisms.

5.4.2 Pulsating acceleration. The presence of broadband periodic pulsations in some solar type IV radiobursts indicates that sometimes a pulsating regime of electron acceleration sets in immediately after a flare. It is characterized by noticeably smaller fluxes of fast electrons but usually lasts much longer that the flare proper. An example is offered by the event on 25 October 1994 explored in Ref. [134] which, based on a combined analysis of spectral and heliographic data in the radio band and on optical and X-ray data, recovered the spatial structure of the source of radio pulsations, which proved to be a coronal magnetic loop. Electrons with velocities of about $0.3c$ were periodically injected from the loop footpoint with a stronger magnetic field, and moved further along the trap axis, generating a sequence of type III bursts with a fast frequency drift. The period of pulsations was 1.33 s on average, while the duration of the pulsating phase was about 3.5 min, so that the pulsations had a high Q-factor. Analysis of the efficiency of the acceleration mechanism for this event [135] demonstrated that the mean rate of electron acceleration in pulsations, $3 \times 10^{32}\ \mathrm{s}^{-1}$, is approximately three orders of magnitude smaller than the rate of electron acceleration in a solar flare of moderate importance. Pulsations have also been detected in flare radio emissions from the late type stars. For instance, spectral analysis of low-frequency modulation of microwave emissions from the flare on 19 May 1997 on AD Leo revealed the existence of two regular components in the radio emission spectrum: a periodic modulation with frequency gradually decreasing from ≈ 2 Hz to ≈ 0.2 Hz in the process of the flare, and a periodic sequence of pulses with the repetition rate of about 2 Hz [16]. A fast negative frequency drift of radio pulsations in this flare [15] is indicative of periodic particle acceleration in lower atmospheric layers followed by particle injection into the stellar corona. A detailed analysis of this event led to the conclusion that the source of radio emission in this case is a magnetic loop with current, and the pulsations with gradually decreasing repetition rate stem from the excitation of natural oscillations of the loop as an equivalent electric circuit with the frequency defined by formula (2.31) [16].

Oscillations of the coronal magnetic loop as an equivalent electric circuit were considered in Ref. [136] for a possible cause of appearing pulsations in the solar type IV radiobursts. An argument in favor of this assumption is a high Q-factor of the observed pulsations, which in this case is ensured by the loop parameters. At the same time, the Q-factor of natural MHD loop pulsations is rather low under the conditions of the solar corona. It was mentioned above that the productivity of the pulsating regime of electron acceleration in the postflare phase of active region development, as estimated for the event on 25 October 1994, proved to be approximately 3 – 4 orders of magnitude lower than the mean productivity for the impulsive phase of a solar flare. The energy of electrons (about 40 keV) accelerated in this event approximately matched the characteristic energy of fast electrons accelerated in the impulsive stage. As follows from formulas (5.1) and (5.6), such a situation arises when the geometrical sizes of the acceleration region are essentially decreasing, with the parameters (T, n, B, B_r, V_r) of the acceleration process being approximately constant.

5.5 The current of accelerated electrons. The Colgate paradox

One more important question debated in the astrophysical literature is concerned with heavy electric currents carried by accelerated electrons [32, 33]. If the production rate of the acceleration mechanism is estimated as $\mathrm{d}N_e/\mathrm{d}t \geqslant 10^{35}$ electrons per second, it corresponds to the induced electric current $I = e\dot{N}_e \geqslant 1.6 \times 10^{15}$ A. If such a current flows in a magnetic loop $\sim 10^{18}\ \mathrm{cm}^2$ in cross section, an induced magnetic field $B \geqslant 6 \times 10^6$ G would accompany it, which is in reality never observed in coronal structures. Two common ways of circumventing this contradiction are considered.

The first possibility derives from the assumption that the current of accelerated electrons is filamented, i.e., the current channel is split into a bundle of thin current filaments with opposite current directions in neighboring filaments, so that the total magnetic field of the current channel does not exceed the observed magnitude [137, 138]. It is not clear, however, how a system of filaments with oppositely directed currents can build up in a diverging beam of electrons. As argued by Fadeev et al. [139], the filamentation of current is indeed possible under certain conditions, but it is not accompanied by current inversion in neighboring filaments, so that one cannot eliminate the problem related to generation of strong magnetic fields at the periphery of the current channel.

The second possibility is attributed to the induction of reverse current in plasmas [140 – 143]. Let, for instance, a beam of electrons of radius r_0 be injected into a plasma along the z-axis of the external magnetic field. Then, the field component B_φ at each given point in the plasma will vary with time as the leading front of the beam passes through it. The variation in B_φ leads to the appearance of an electric field E_z at the beam leading front, acting on plasma electrons so as to induce a current directed against the injected current. Subsequently, the beam current gets reduced to its full compensation. If the radius of the fast electron beam exceeds

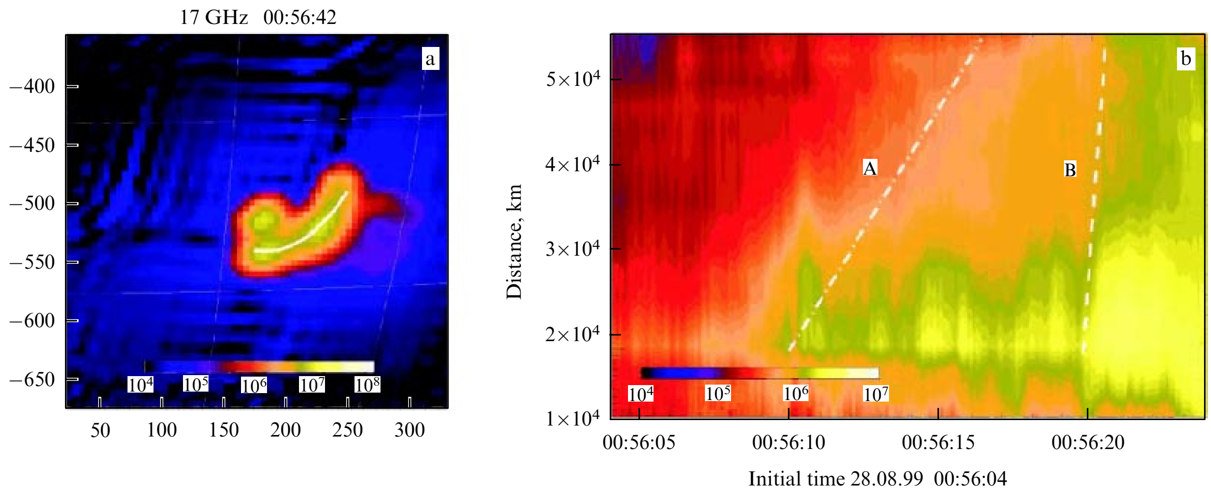

Figure 12. Image of two interacting flare loops (Radioheliograph Nobeyama, 17 GHz). The white line in figure (a) marks trajectories of propagating relativistic electrons (source coordinates in angular seconds are plotted on the axes). In plate (b), line A marks the propagation of particles along the loop at a velocity of $c/30$, and line B at the speed of light [144].

the screening length ($r_0 > c/\omega_p$), the magnetic field is absent for $r > r_0$. The beam current is compensated for by the reverse plasma current which is almost entirely confined inside the beam. The condition of complete neutralization is formulated as $c/\omega_p \ll r_0$, $\nu_{ei} t < 1$, where t is the time elapsed after the electron beam injection. For time instants satisfying the condition $\nu_{ei} t \gg 1$, the reverse current decays and the neutralization gradually disappears. However, the characteristic decay time for the reverse current is determined by the magnetic diffusion time $t_D = \pi\sigma r_0^2/c^2$, which for r_0 on the order of the loop thickness exceeds significantly all time scales intrinsic to flare processes. Thus, it is plausible to suppose that the injection of accelerated electrons does not change the external magnetic field.

5.6 Turbulent regime of high-energy particle propagation

Confirmation of the existence of wave – particle interaction in the solar corona is provided by the unusual character of high-energy particle propagation. Thus, in a flare on 28 August 1999 [144] relativistic electrons generating synchrotron radiation at a frequency of 17 GHz traveled along the coronal magnetic loop at a speed 30 times slower than the speed of light (Fig. 12). This phenomenon can be explained as being a consequence of strong turbulent diffusion, when the output of the high-energy particle accelerator is $J > J_* = cB\sigma/(4\pi e l)$ cm^{-2} s^{-1} [145, 146]. A low-frequency whistler turbulence excited by the electron streams effectively scatters the relativistic particles over the pitch angle. As a result, instead of free propagation, the electrons are affected by an anomalous (turbulent) viscosity and move with a velocity close to the phase velocity of whistlers, $0.03c$ [147].

The second example is offered by the absence of appreciable linear polarization ($< 0.07\%$) in the Hα-emission from flares, generated by streams of energetic protons upon their braking in the chromosphere [148]. The most likely cause of this phenomenon is attributable to isotropization due to scattering on small-scale Alfvén waves excited at ion cyclotron resonance by protons with an energy of $E_{pr} \leqslant 1$ MeV [149]. In this case, the protons are efficiently scattered over the pitch angle (strong diffusion) if the capacity of the accelerator exceeds the threshold value of $J_* = 5 \times 10^{12}$ protons per cm^2 per s. Observational data on high-energy particles in solar flares imply that the generation rate of protons with the energy $E_{pr} \sim 1$ MeV is on the order of $10^{33} - 10^{34}$ protons per s [125]. Assuming that the area in which the streams of protons enter the chromosphere is estimated as $\sim 10^{18}$ cm^2, we find for their flux the following estimate: $J \sim 10^{15} - 10^{16}$ cm^{-2} s^{-1} $\gg J_*$.

The regime of strong diffusion also brings about time delays in gamma emission in lines with respect to hard X-ray emissions in solar flares for simultaneously accelerated electrons and ions, as the front velocity of small-scale Alfvén turbulence created by high-energy ions is lower by an order of magnitude than the velocity of the turbulent whistler 'wall' created by fast electrons [150].

6. The coronal loop as a magnetic trap

The magnitude of a magnetic field at the footpoints of a coronal loop located in the photosphere exceeds its magnitude at the loop top, so that the loop represents a magnetic trap for charged particles. Coronal loops on the Sun and stars are the sources of intense nonthermal radio emission. The emission originates from high-energy electrons which land in magnetic loops owing to acceleration processes and stay there, confined by the magnetic field of the trap. The confinement time of high-energy particles is determined by either Coulomb collisions or wave – particle interaction. In low solar loops having high plasma density, gyrosynchrotron emission of high-energy electrons prevails. Nevertheless, the plasma mechanism of radio emission can play a certain role in some events.

Emissions from high loops (with wavelengths from several decimeters to several dozen meters) exhibit great diversity and a well-developed fine structure and are in most cases of a 'maser' origin. Their observations and analysis are important for diagnosing the coronal plasma and explaining processes proceeding there. A relatively high intensity of emissions is ensured by particle population inversion, leading to instability of small-scale waves which have low generation thresholds in high and less dense loops. These waves, in turn, can change particle distributions or affect their dynamics and propagation. If the pressure exerted by high-energy particles is sufficiently high, large-scale instabilities develop in the magnetic loop, which allow high-energy particles to escape from coronal loops.

6.1 Charged particle distribution in loops

The appearance of accelerated particles in a loop forms the distribution 'equilibrium plasma + high-energy particles with a loss cone' which is unstable with respect to the generation of waves of various types. Indeed, one can readily find that for coronal loops with the parameters listed in Table 1, the mean free path of particles of the background plasma with temperature $T = 10^6 - 10^7$ K is much shorter than the loop size, and that high-energy ($\geqslant 30$ keV) electrons and ions ($\geqslant 1$ MeV) are collisionless. Apart from this, in a magnetic field with induction of about 100 G the gyroradius of high-energy particles is $r_c = v/\omega_c \leqslant 10$ cm $\ll l$. Under these conditions, accelerated charged particles with the momentum components ratio $p_\perp/p_{||} < (\sigma - 1)^{-1/2}$, where $\sigma = B_{\max}/B_{\min}$ is the magnetic mirror ratio, and $B_{\max}$ and $B_{\min}$ are the magnetic field inductions at the footpoint and top of the magnetic loop, respectively, cannot be confined by the loop magnetic field and 'precipitate' to the footpoints. Particles trapped by the loop hence form a loss cone in the momentum space, where the distribution of particles can be represented as

$$f_1(p) = \frac{n_1}{(2\pi)^{3/2} a^3 \cos\theta_0} \exp\left(-\frac{p^2}{2a^2}\right) \times \left[H(\theta - \theta_0) - H(\theta + \theta_0 - \pi)\right], \tag{6.1}$$

where $H(x)$ is the Heaviside function defined as

$$H(x) = \begin{cases} 1, & x \geqslant 0, \\ 0, & x < 0, \end{cases}$$

θ is the angle between the directions of particle momentum and the magnetic field vector, $\cos\theta_0 = \left[(\sigma - 1)/\sigma\right]^{1/2}$, a is the variance, and $n_1 \ll n_0$. From data on X-ray emissions from solar flares it follows that the distribution of accelerated electrons over energy is often characterized by a power-law spectrum:

$$f_1 \propto n_1 E^{-\delta}\left[H(\theta - \theta_0) - H(\theta + \theta_0 - \pi)\right]. \tag{6.2}$$

It cannot be excluded that there are streams of high-energy particles in loops with the distribution described as a 'hollow-beam':

$$f_1 \propto n_1 \exp\left[-\frac{(p_{||} - p_{||0})^2}{a_{||}^2} - \frac{(p_\perp - p_{\perp 0})^2}{a_\perp^2}\right]. \tag{6.3}$$

For some applications, a convenient choice for the particle momentum distribution in a loop is as follows [151]:

$$f_i \propto n_i p_\perp^{2\eta} \exp\left(-\frac{p^2}{a_i^2}\right), \tag{6.4}$$

where $\eta = 0$ for the background equilibrium plasma ($i = 0$), and $\eta = 1, 2, 3, \ldots$ for high-energy particles ($i = 1$, $n_1 \ll n_0$). Various model forms of high-energy particle distributions, typical for magnetic traps, can be found in the monograph by Mikhailovskii [152] and review [153].

6.2 The loop as an electron-cyclotron maser

The instability of ordinary (o) and extraordinary (x) waves at the harmonics of the electron gyrofrequency, also dubbed the electron-cyclotron maser (ECM), was considered as a possible reason for intensive radio emissions from solar and stellar flares [153–160], auroral emission from the Earth in the kilometer wave range [161], and Jovian decameter radio emission [162]. The interaction between waves and energetic particles takes place under conditions of cyclotron resonance:

$$m\omega - s m_0 \omega_c - k_{||} p_{||} = 0, \tag{6.5}$$

where $m = m_0 \Gamma$, m_0 is the electron rest mass, and $\Gamma = (1 - v^2/c^2)^{-1/2}$ is the Lorentz factor. For solar coronal loops, the ECM-related radio emission was first studied in Ref. [155]. The most favorable conditions for ECM emission are realized in rather strong magnetic fields, where the electron gyrofrequency exceeds the plasma frequency, $\omega_c > \omega_p$, i.e., in active regions of the Sun and flaring stars. The wave instability growth rate for the sth harmonic is expressed in the form [163]

$$\gamma_{o,x} = \int \mathrm{d}\mathbf{p}\, A_{o,x}(\mathbf{p}, \mathbf{k})\, \delta\left(\omega - \frac{s\omega_c}{\Gamma} - k_{||} v_{||}\right) \times \left(\frac{s\omega_c}{\Gamma v_\perp} \frac{\partial}{\partial p_\perp} + k_{||} \frac{\partial}{\partial p_{||}}\right) f_1(p_\perp, p_{||}), \tag{6.6}$$

where

$$A_{o,x}(\mathbf{p}, \mathbf{k}) = \frac{4\pi^2 e^2 v_\perp^2}{\omega N_{o,x}\left[\partial(\omega N_{o,x})/\partial\omega\right](1 + T_{o,x}^2)} \times \left|\frac{K_{o,x}\sin\vartheta + (\cos\vartheta - N_{o,x} v_{||}/c)\, T_{o,x}}{N_{o,x}(v_\perp/c)\sin\vartheta} J_s + J_s'\right|^2, \tag{6.7}$$

$J_s(\omega N_{o,x} v_\perp \sin\vartheta/\omega_c c)$ is the Bessel function, ϑ is the angle between the wave vector and the magnetic field vector, $T_{o,x}$ and $K_{o,x}$ are the polarization coefficients, and $N_{o,x}$ is the wave refractive index [163]. The results pertaining to studies of the linear phase of ECM instability [152–159, 161–163], described by formulas (6.6) and (6.7), for various distributions of fast electrons with a loss cone, and different ratios ω_p/ω_c, and also to the quasilinear phase of the ECM [160], can be summarized as follows. The extraordinary wave at the first harmonic of the gyrofrequency is predominantly generated in strong magnetic fields ($\omega_p/\omega_c < 0.24 - 0.4$). Within the interval $0.24 - 0.4 < \omega_p/\omega_c < 1$, it is the ordinary wave at the harmonic with $s = 1$. Maximum growth rates are of the order

$$\gamma_x \approx 10^{-2} \frac{n_1}{n_0} \omega_c, \quad \gamma_o \approx 2 \times 10^{-3} \frac{n_1}{n_0} \omega_c \tag{6.8}$$

and in both cases are realized for waves propagating at $\vartheta_m \approx 70°$ to the magnetic field vector. The angular width of the directivity pattern for the excited waves is $\Delta\vartheta \approx 3°$. If $\omega_p/\omega_c > 1$, the maximum growth rate is found for potential waves with upper hybrid frequency $\omega_{uh} = (\omega_p^2 + \omega_c^2)^{1/2}$, while the growth rate for ECM emission in the form of an x-mode at frequency $\omega \approx 2\omega_c$ is smaller by several orders of magnitude.

6.3 Problem of escape of radio emission from stellar coronae

An electron-cyclotron maser generates electromagnetic waves as such, without losing energy in transformation processes, and at first glance seems to be a rather efficient mechanism. Nevertheless, the escape of ECM emission out of hot ($10^7 - 10^8$ K) stellar coronae presents a problem because of the

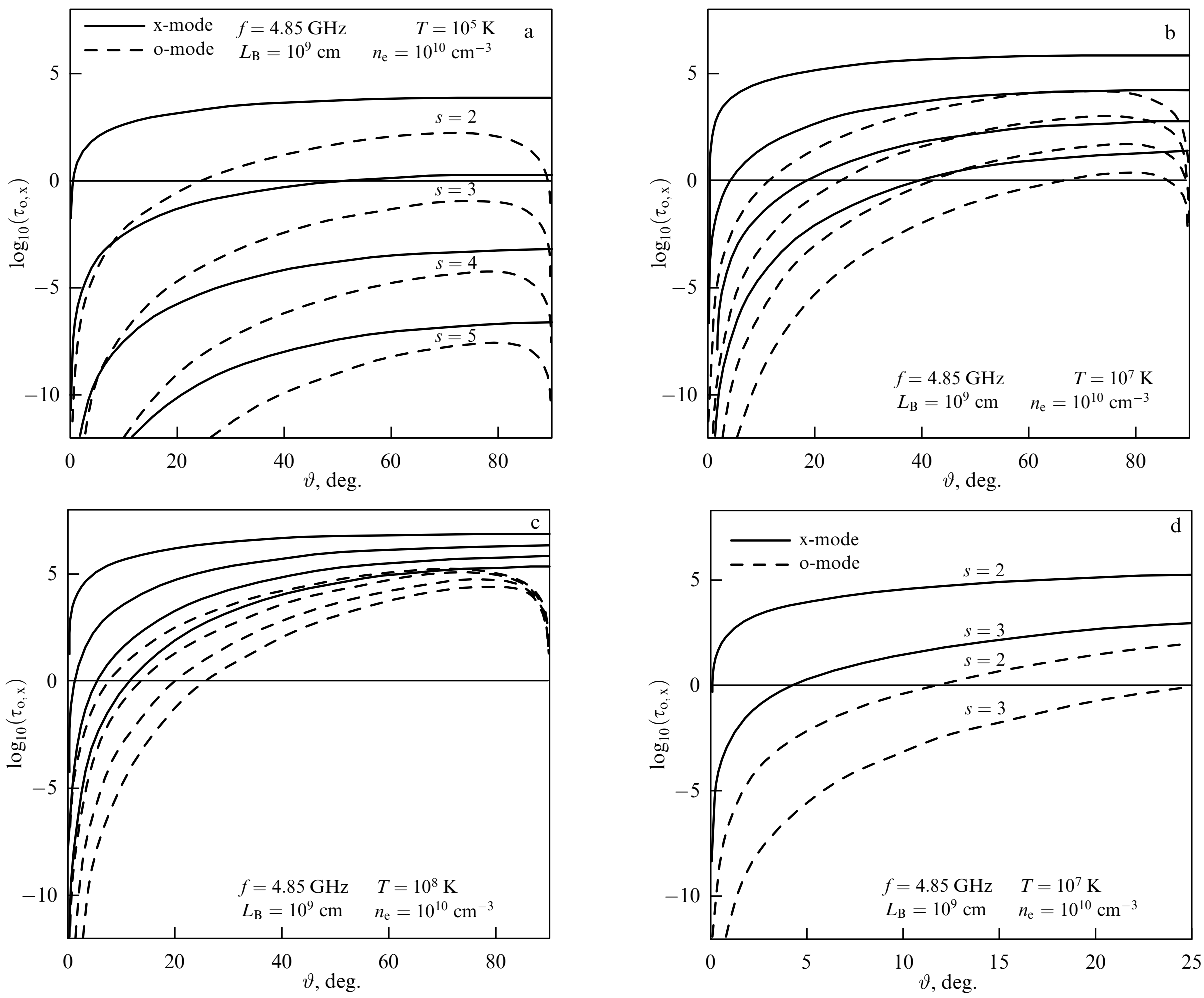

Figure 13. Dependence of the optical thickness of cyclotron absorption for ordinary and extraordinary waves with a frequency of 4.85 GHz on the angle of propagation ϑ in a stellar corona at levels $s = 2, 3, 4, 5$ for typical parameters of red dwarfs in the cases of 'cold' (a) and 'hot' (b, c) coronas. It can be seen (d) that for $T = 10^7$ K the transparency window for the x-mode is virtually absent at the second gyrolevel, whereas it is 11° for the o-mode. The respective values are 4° and 25° at the third gyrolevel.

strong cyclotron absorption of waves by the coronal plasma. Indeed, an ECM conditioned by a loss cone generates preferentially extraordinary waves around the direction perpendicular to the magnetic field vector. Propagating through overlying layers of coronal plasma, the x-waves suffer from strong absorption at the harmonics of the electron gyrofrequency. There exist only narrow 'windows' along the magnetic field that allow the ECM emission to escape [164, 165]. Vlahos et al. [166] attempted to describe cyclotron absorption in the solar corona as a function of the wave propagation angle. However, computations of optical thickness of cyclotron absorption were performed incorrectly in Ref. [166] and gave a rather broad escape window for the x-mode in the direction transverse to the magnetic field. Robinson [167] drew attention to the existence of a window transverse to the magnetic field for the ordinary mode and proposed a mechanism for the escape of extraordinary waves at the gyrofrequency ($s = 1$) through their linear conversion into ordinary waves. In this case, the optical thickness of gyroabsorption decreases by a factor of several hundred. However, as will be shown further (Fig. 13), the wave escape windows in the direction transverse to the magnetic field are much narrower than along it.

The computation of cyclotron absorption at harmonics with $s = 2, 3, 4, 5$ for characteristic frequencies of signals from flaring stars observed with radio telescopes in Arecibo and Effelsberg (1.4–5 GHz) was carried out in Refs [164, 165]. The expression for the optical thickness of the absorption process has the form [163, 168]

$$\tau_{o,x}(s \geqslant 2) = \pi \left(\frac{\omega_p}{\omega_c}\right)^2 \frac{\omega L_B}{c} \frac{1}{s!} \left(\frac{s}{2}\right)^{2s} (\beta_T \sin\vartheta)^{2s-2} C_{o,x}, \tag{6.9}$$

where L_B is the characteristic scale of magnetic field inhomogeneity, $\beta_T = \sqrt{2T/mc^2}$, and

$$C_{o,x} = N_{o,x} \frac{(1 - T_{o,x}\cos\vartheta - K_{o,x}\sin\vartheta)^2}{1 + T_{o,x}^2}. \tag{6.10}$$

Notice that formulas (6.9) and (6.10) hold for $\vartheta \neq \pi/2$. At $\vartheta = \pi/2$, relativistic corrections and singularities in $T_{o,x}$ and $K_{o,x}$ should be taken into account [163, 164].

Figure 13 shows that the most favorable conditions for the escape of radio emission from the corona for o- and x-modes at harmonics with $s \geqslant 2$ exist in the direction along the

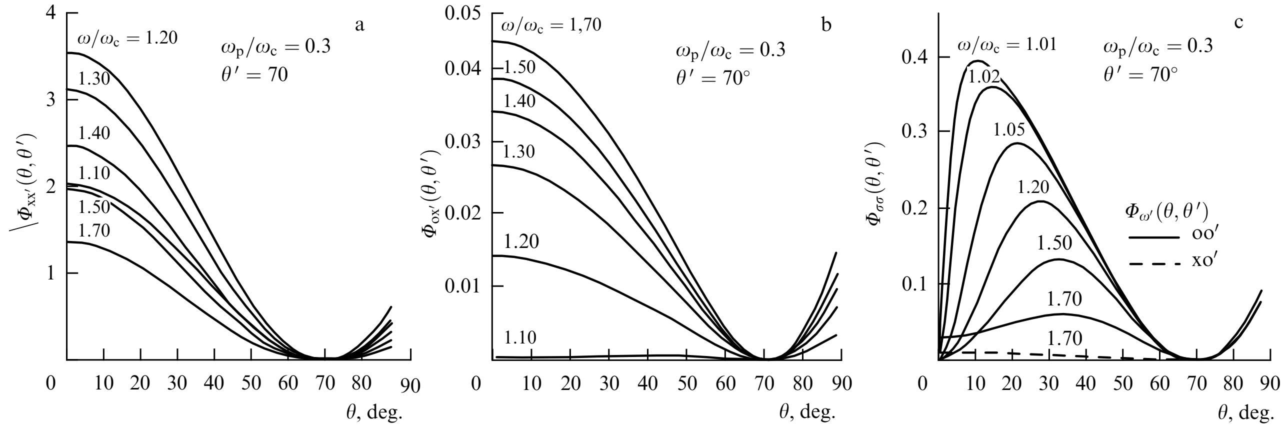

Figure 14. Dependences of the probability of induced xx-scattering (a), xo-scattering (b), and oo-scattering (c) on the angle θ between the wave vector of the scattered wave and the magnetic field vector for various values of scattered wave frequency. $\theta' = 70°$ is the angle between the magnetic field vector and the wave vector of the scattered wave, corresponding to the maximum increment of ECM wave generation. The dashed line in (c) depicts the probability of ox-scattering in the region above the cut-off frequency at $\omega_p = \omega_c$ [169].

magnetic field, with escape windows being much broader for ordinary waves. Thus, solution to the escape problem for radio emission in stellar coronae lies in searching for efficient mechanisms of the ECM emission 'transfer' to the escape windows. The most likely mechanism of transfer over the angle is offered by processes of induced scattering of electromagnetic waves on particles of thermal plasma [169] and small-scale turbulence [164].

Reference [169] explored the possibility for radio emission generated by an ECM at a frequency close to the electron gyrofrequency to escape through scattering on ions of thermal plasma under conditions encountered in coronae on the Sun and red dwarfs. The appropriate computations revealed that the induced wave scattering gives rise to the formation of condensate of ECM emission with wave vectors spanning directions close to that of the magnetic field, which has to facilitate the escape of emission through the escape windows (Fig. 14). Although the efficiency of integral scattering of an extraordinary wave with its transformation into a like wave (xx-scattering) is significantly higher than the efficiency of scattering for an ordinary wave without transformation (oo-scattering), the narrow escape windows for the x-mode drastically reduce the feasibility of its escape from the corona. For instance, only 0.1% of scattered radiation of the x-mode can leave the corona of AD Leo. On the other hand, notwithstanding the lower efficiency of oo-scattering (Fig. 14c), the angular width of the condensate of ordinary waves is narrower than the transparency window width (see Fig. 13). Thus, if the level of excited waves is sufficient, the major part of ECM emission leaves the source by virtue of the induced scattering from the instability domain into the transparency window. Hence, it follows that strong ECM emissions from flares on stars should be polarized as an ordinary wave.

In addition to Langmuir and high-frequency electromagnetic waves, flares on stars are accompanied by excitation of small-scale waves of other types: whistler, ion-acoustic, Alfvén, and fast magneto-acoustic. Estimates based on the formulas of Ref. [170] indicated that induced angular scattering of ECM emission proceeds most efficiently on ion-acoustic turbulence; its level should reach the values of $W_s/n_0T \geqslant 10^{-5}-10^{-4}$ in stellar coronae [164].

6.4 Plasma mechanism of radio emission from coronal loops

In a sufficiently dense plasma of coronal loops, such that $\omega_p/\omega_c > 1$, a plasma mechanism of radio emission dominates. It was first invoked by Ginzburg and Zheleznyakov [171] for explaining type III bursts of solar radio emission. The plasma mechanism supposes that initially the Langmuir waves are excited owing to inverse population of energetic electrons. These waves then transform into electromagnetic waves escaping the corona. The plasma density may reach the values of $n_0 \approx 10^{11}-10^{12}$ cm^{-3} in flare loops on the Sun [172, 173] and most stars of late spectral classes [13], so that the condition $\omega_p/\omega_c > 1$ remains valid even in magnetic fields with induction $B \geqslant 10^3$ G. The authors of this review suggested in Ref. [174] a plasma mechanism for hot flare loops on the Sun, emitting radiation in the frequency range of $1-10$ GHz. Reference [174] deals with the cases of $\omega_p^2/\omega_c^2 \gg 1$ and $k_{\parallel}v_{\parallel} \gg \omega_c$, where emission at frequency ω comprises several harmonics of the gyrofrequency. Under these conditions, the instability growth rate of plasma waves with $\omega \approx \omega_p$ and $k_\perp \gg k_\parallel$ is given by [152]

$$\gamma = \frac{\pi}{n_0}\,\frac{\omega_p^4}{k^3}\int_{-\infty}^{\infty} \mathrm{d}v_\parallel \int_{\omega^2/k^2}^{\infty} \mathrm{d}v_\perp^2\, \frac{\partial f_1/\partial v_\perp^2}{\sqrt{v_\perp^2-\omega^2/k^2}}\,. \tag{6.11}$$

Substituting the distribution function of type (6.1) for high-energy electrons into Eqn (6.11), we find the instability growth rate for the Langmuir waves. Its maximum value for a sufficiently large value of loss cone ($\sigma \approx 2$) is defined as

$$\gamma_{\max} \approx 0.1\,\frac{n_1}{n_0}\,\omega_p\,. \tag{6.12}$$

The damping of plasma waves via electron–ion collisions, $\nu_{ei} \approx 60n_0/T^{3/2}$, sets the lower instability threshold with respect to the density of high-energy particles:

$$\frac{n_1}{n_0} > 10\,\frac{\nu_{ei}}{\omega_p} \approx 5\times10^{-7}\,. \tag{6.13}$$

Besides collisional damping, one has to make allowance for Landau damping in hot coronal loops. The plasma wave instability diagram in relation to the mirror ratio of a compact flare loop is presented in Fig. 15a [174].

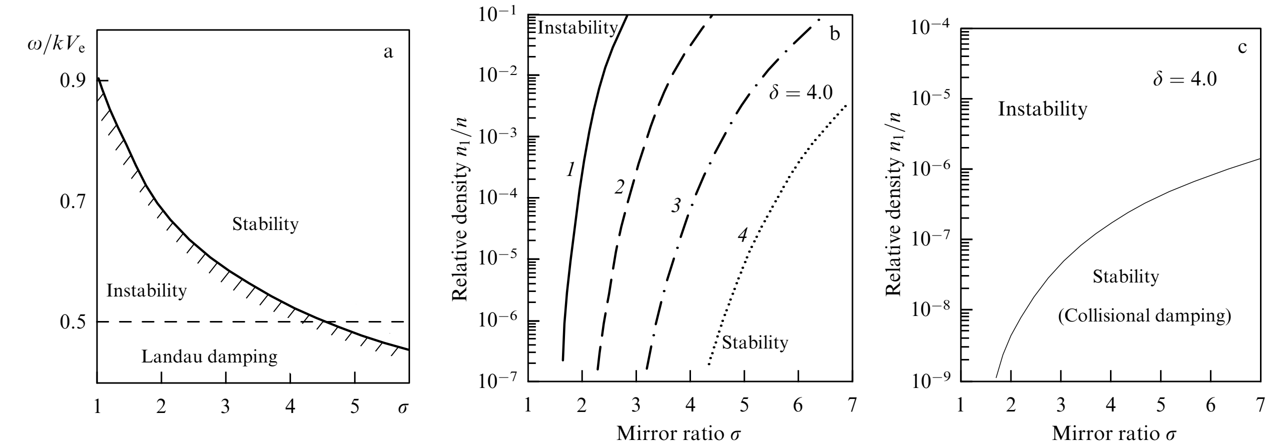

Figure 15. (a) The region of instability of plasma waves for the distribution (6.1) of high-energy particles for $T = 10^7$ K, and $V_e = a/m \approx 10^{10}$ cm s^{-1}. (b) The instability region for the distribution (6.14) at $T = 3 \times 10^7$ K (curve *1*), 1.2×10^7 K (curve *2*), 7×10^6 K (curve *3*), and 4.5×10^6 K (curve *4*). (c) The instability region for the distribution (6.14) for $n_0 = 3 \times 10^{10}$ cm^{-3} and plasma temperature $T < 3 \times 10^6$ K$/(\sigma - 1)$ in the case when collisional damping is stronger than the Landau damping.

Reference [175] dealing with plasma radio emission of the continuum type from solar loops found plasma wave instability regions for a power-law velocity distribution of electrons with energy $E \geqslant 10$ keV and a loss cone which instead of sharp boundary (6.2) has a boundary depending on the energy:

$$f_1(v_\parallel, v_\perp) \propto \frac{n_1}{(v_\parallel^2 + v_\perp^2)^\delta} \left[1 - \exp(-y)\right], \quad y = (\sigma - 1)\, \frac{v_\perp^2}{v_\parallel^2}\,. \tag{6.14}$$

On substituting distribution function (6.14) into formula (6.11), the instability regions with respect to the density of high-energy electrons were found taking into account both Landau damping (Fig. 16b) and damping due to particle collisions (Fig. 16c).

The excited plasma waves are transformed into electromagnetic waves via scattering on particles of thermal plasma (Rayleigh scattering). The conservation laws in this process are as follows:

$$\omega_t - \omega = (\mathbf{k}_t - \mathbf{k})\, \mathbf{v}\,, \tag{6.15}$$

where ω_t and $\mathbf{k}_t$ are the frequency and wave vector of electromagnetic waves, and $\mathbf{v}$ is the velocity of scattering particles. The Rayleigh scattering on plasma ions is the most efficient in producing radio emission in the fundamental tone: $\omega_t \approx \omega_p$. The dispersion relations for plasma and electromagnetic waves in the limit of $\omega_p^2/\omega_c^2 \gg 1$ assume the form

$$\omega^2 = \omega_p^2 + 3v_T^2 k^2\,, \quad \omega_t^2 = \omega_p^2 + k_t^2 c^2\,. \tag{6.16}$$

Dispersion relations (6.16) and energy conservation law (6.15) define the region of nonlinear interaction between the waves:

$$L_N = 3L_n\, \frac{v_T^2}{\omega_p^2}\, (k_{\max}^2 - k_{\min}^2) \approx 3L_n\, \frac{v_T^2}{v^2}\,, \tag{6.17}$$

where L_n is the scale of particle concentration inhomogeneity for the source located in a stellar coronal magnetic loop, $L_n = n_0/|\nabla n_0|$, v_T and v are the velocities of thermal plasma particles and energetic particles, respectively, and $k_{\max}$ and $k_{\min}$ bound the spectrum of excited plasma waves.

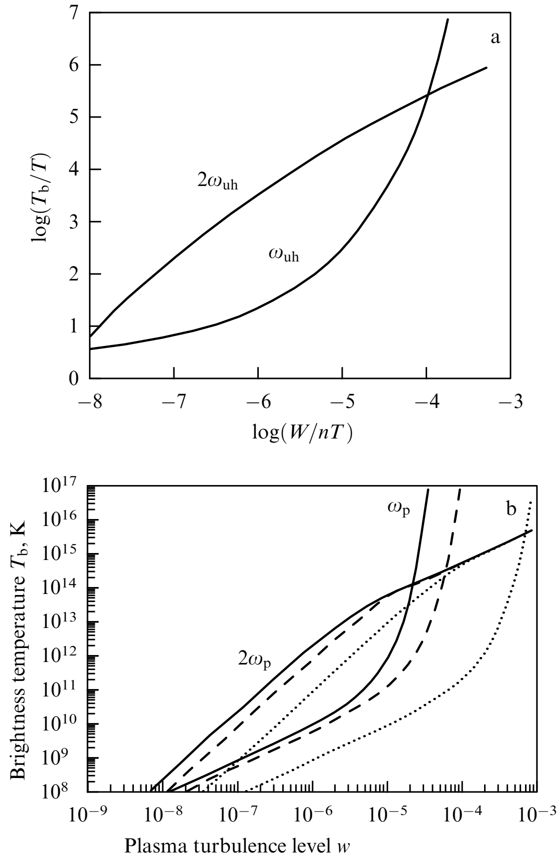

Figure 16. Dependence of the brightness temperature T_b of radio emission on the plasma turbulence level $w = W/nT$: (a) for a dense flare loop on the Sun at $T = 3 \times 10^6$ K, when the fundamental tone is observed at a frequency of 10 GHz [174]; (b) for a loop on the red dwarf AD Leo at $T = 10^7$ K and energy of accelerated electrons $E = 30$ keV, when the fundamental tone corresponds to a frequency of 1.4 GHz. The solid, dashed, and dotted lines correspond to $L_n = 3 \times 10^9$ cm, $L_n = 10^9$ cm, and $L_n = 10^8$ cm, respectively [176].

The transfer equation for the brightness temperature of emission is written out in the form [168]

$$\frac{dT_b}{dl} = a - (\mu_N + \mu_c)\, T_b\,, \tag{6.18}$$

where a is the radiating capacity, $\mu_{\rm N}$ is the coefficient of absorption (amplification) due to nonlinear processes, and $\mu_{\rm c}$ is the collisional absorption coefficient.

The solution of the transfer equation (6.18) is given by

$$T_{\rm b} = \frac{a}{\mu_{\rm c} + \mu_{\rm N}} \left[1 - \exp\left(- \int_0^{L_{\rm N}} (\mu_{\rm c} + \mu_{\rm N})\,{\rm d}l \right) \right], \quad (6.19)$$

where $L_{\rm N}$ is expressed by formula (6.17). For Rayleigh scattering, the coefficients of emission and absorption are written out as follows [168, 174]:

$$a_1 \approx \frac{\pi}{36} \frac{\omega_{\rm p}}{v_{\rm g}} m v^2 w, \quad \mu_{\rm N1} \approx -\frac{\pi}{108} \frac{m}{m_{\rm i}} \frac{\omega_{\rm p}}{v_{\rm g}} \frac{v^2}{v_{\rm T}^2} w,$$

$$\mu_{\rm c} = \frac{\omega_{\rm p}^2}{\omega_{\rm t}^2} \frac{\nu_{\rm ei}}{v_{\rm g}} \approx \frac{\nu_{\rm ei}}{v_{\rm g}}, \quad (6.20)$$

where $v_{\rm g}$ is the group velocity of electromagnetic waves, and $w = W/n_0 T$ is the plasma turbulence level. Since $\mu_{\rm N1}$ is negative, for $|\mu_{\rm N1}| > \mu_{\rm c}$, i.e., provided the plasma turbulence level is sufficiently high, an exponential growth in emission brightness temperature is possible, which yields a maser-effect.

Radio emission at a doubled plasma frequency is generated as the result of Raman scattering of plasma waves. The energy and momentum conservation laws take the form:

$$\omega_1 + \omega_2 = \omega_{\rm t}, \quad \mathbf{k}_1 + \mathbf{k}_2 = \mathbf{k}_{\rm t}, \quad (6.21)$$

where ω_1 and $\mathbf{k}_1$, and ω_2 and $\mathbf{k}_2$ are the frequencies and wave vectors of interacting plasma waves. The emissivity and absorption coefficient have the form [168, 174]

$$a_2 \approx \frac{(2\pi)^5}{15\sqrt{3}} \frac{\omega_{\rm p}^4 n_0 T}{v c^3 \Delta^2} w^2, \quad \mu_{\rm N2} \approx \frac{(2\pi)^2}{15\sqrt{3}} \frac{\omega_{\rm p}^4}{v c^3 \Delta} w,$$

$$\mu_{\rm c2} \approx \frac{\nu_{\rm ei}}{2\sqrt{3}\,c}. \quad (6.22)$$

Here, $\Delta = (4\pi/3)(k_{\rm max}^3 - k_{\rm min}^3)$ is the phase volume of the plasma waves. Examples of the behavior of the radiation brightness temperature at the fundamental tone and the second harmonic as a function of the plasma wave turbulence level w are given in Fig. 16 for the Sun and AD Leo. The radio emission at the fundamental tone prevails when the plasma wave turbulence level is relatively high ($w \approx 10^{-5} - 10^{-3}$ in Fig. 16). For lower levels of plasma turbulence, the emission at the doubled plasma frequency dominates, reaching values of $T_{\rm b} \approx 10^{13} - 10^{14}$ K on AD Leo for $w \approx 10^{-5}$, whereas the radiation brightness temperature in the fundamental tone is $T_{\rm b} \approx 10^{10} - 10^{12}$ K. The value of w that marks the exponential amplification of the fundamental tone emission (the maser-effect) depends on loop parameters and is confined to the range $w \approx 4 \times 10^{-6} - 10^{-4}$.

According to Eqns (6.17) and (6.19), hot ($T \geqslant 10^7$ K) stellar coronae foster a higher efficiency of the plasma radio emission mechanism compared to that in the solar corona because of the essentially increased transformation length $L_{\rm N} = 3L_n(T/E)$. Moreover, the high temperature of stellar coronal loops leads to reducing the phase volume Δ of plasma waves and thus favors the growth of radio emission brightness temperature of the harmonic. Relatedly, collisional wave damping is also reduced. This answers the question of Abada-Simon et al. [54] as to why the plasma mechanism of radio emission is more efficient on stars than on the Sun.

The radio emission flux from a star is expressed as

$$S_f = \frac{2T_{\rm b} f^2}{c^2} \frac{A}{d^2}, \quad (6.23)$$

where A is the source area, and d is the distance to the star. Assuming the value of brightness temperature to be $T_{\rm b} \approx 10^{14}$ K, and $L_n = \sqrt{A} = 3 \times 10^9$ cm, for AD Leo ($d = 4.85$ pc $\approx 1.55 \times 10^{19}$ cm) we find $S_f \approx 3$ Jy at a frequency $f = 4.85$ GHz. Such fluxes accompany energetic flares on red dwarfs. For a close binary system, exemplified by AR Lac, for $T_{\rm b} = 10^{14}$ K, $A = 9 \times 10^{20}$ cm^2, $d = 50$ pc $= 1.5 \times 10^{20}$ cm, and $f = 1$ GHz from formula (6.23) it follows that $S_f \approx 120$ mJy, which also agrees with observed radio emission fluxes from close binary systems.

Above we were in fact limited to the case of isotropic plasma in which the directivity patterns for the radiation in the fundamental tone and harmonic have dipole and quadrupole shapes, respectively [168, 177]. The directivity patterns for the plasma emission mechanism in a magnetic field were computed in Refs [165, 178]. In a magnetoactive plasma, the directivity pattern for Rayleigh scattering of a plasma wave incident on the scattering volume perpendicular to the magnetic field is expressed as follows [179]:

$$D(\theta) = N^3 \left[\left(\varepsilon_1 - 1 + \frac{\varepsilon_2^2}{N^2 - \varepsilon_1} \right)^2 + \varepsilon_2^2 \left(\frac{N^2 - 1}{N^2 - \varepsilon_1} \right)^2 \right]$$
$$\times \left[\varepsilon_1 + \varepsilon_1 \frac{\varepsilon_2^2}{(N^2 - \varepsilon_1)^2} + 2\frac{\varepsilon_2^2}{N^2 - \varepsilon_1} + \varepsilon_3 \left(\frac{N^2 \sin\theta\cos\theta}{N^2 \sin^2\theta - \varepsilon_3} \right)^2 \right]^{-1}. \quad (6.24)$$

Here, θ is the angle between the wave vector $\mathbf{k}_{\rm t}$ of a scattered electromagnetic wave and the vector $\mathbf{B}_0$ of external magnetic field in the scattering volume, and N is the refractive index for electromagnetic waves [168]:

$$N_{\rm x,o}^2 = 1 - \frac{2v(1-v)}{2(1-v) - u\sin^2\theta \mp \left(u^2 \sin^4\theta + 4u(1-v)^2 \cos^2\theta\right)^{1/2}}, \quad (6.25)$$

where the subscript x (and the upper sign) correspond to the extraordinary wave, $v = \omega_{\rm p}^2/\omega^2$, and $u = \omega_{\rm c}^2/\omega^2$. The components of the permittivity tensor are as follows: $\varepsilon_1 = 1 - v/(1-u)$, $\varepsilon_2 = \sqrt{u}\,v/(1-u)$, and $\varepsilon_3 = 1 - v$. Only an ordinary wave with a frequency close to $\omega_{\rm uh}$ leaves the source, since $N_{\rm x}^2 < 0$ for extraordinary waves. If the observed radio emission at 1.4 GHz corresponds to the fundamental tone $\omega_{\rm uh} = (\omega_{\rm p}^2 + \omega_{\rm c}^2)^{1/2}$, then, for instance, at $\omega_{\rm p}^2/\omega_{\rm c}^2 = 3$, the plasma density and magnetic field induction in the source are, respectively, $n_0 \approx 2 \times 10^{10}$ cm^{-3} and $B = 250$ G. The pattern $D(\theta)$ normalized so that $D(0) = 1$ is displayed in Fig. 17. In isotropic plasma it corresponds to a dipole emission $D(\theta) \propto \cos^2\theta$. The magnetic field influence is manifested in narrowing the fundamental tone directivity pattern.

Narrowing the emission directivity pattern is also facilitated by a high level of plasma wave turbulence, at which the scattering of the waves on particles, governed by relationship (6.15), acquires an induced character and the intensity of radio emission varies as $\propto \exp(\tau\cos^2\theta)$, where τ is the optical thickness of the process (6.15). This issue was first pointed out

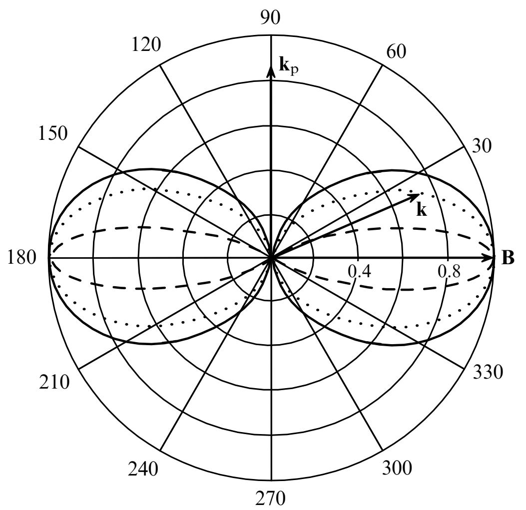

Figure 17. Directivity pattern of plasma radio emission at the fundamental tone (ordinary wave), when the initial spectrum of plasma waves is directed transverse to the magnetic field. The solid line corresponds to isotropic plasma, the dotted one to the case of $\omega_p^2/\omega_c^2 = 3$, and the dashed line describes the diagram of induced emission $\propto \exp(\tau \cos^2\theta)$ at $\tau = 10$ [179]; $\mathbf{k}_p$ is the wave vector of plasma waves, and $\mathbf{k}$ is the wave vector of the ordinary mode.

by Ginzburg et al. [180, 181] when interpreting radio emissions from pulsars. A regular refraction of radio waves in a corona with plasma density decreasing with height is also conducive to narrowing of the emission directivity pattern [168]. Both these circumstances made it possible to explain the very confined radio emission with the angular width $\sim 5°$ from the magnetic, chemically peculiar star CU Virginis (HD 124224), observed with VLA [182], by invoking the plasma mechanism [178].

Thus, the most favorable conditions for the escape of emission from stellar coronal loops are inherent in the plasma radio emission mechanism for which, in particular, the fundamental tone directivity pattern possesses a maximum along the magnetic field. The directivity pattern of emission at the harmonic preserves its quadrupole character in the magnetic field [165] so that it needs additional scattering over angles to escape through the transparency windows, similar to the case with the ECM.

6.5 Instabilities of whistlers and Alfvén waves

In addition to the waves mentioned above, coronal loops host other modes too, in particular, whistlers and Alfvén waves which, as shown in Section 5, affect to a large degree the dynamics and propagation of high-energy particles through wave – particle interactions. From the dispersion relation for whistlers, namely

$$\omega = \omega_c \frac{k^2 c^2 |\cos\vartheta|}{\omega_p^2 + k^2 c^2}\,, \tag{6.26}$$

and cyclotron resonance condition (6.2), the velocity of high-energy electrons that are at resonance with the waves is determined as follows:

$$|v_{||}| = c\,\frac{\omega_c - \omega}{\omega_p}\sqrt{\frac{\omega_c|\cos\vartheta| - \omega}{\omega}}\,. \tag{6.27}$$

For the distribution function (6.2) of high-energy electrons, the instability growth rate is given by [183]

$$\gamma_w = 2\pi^2 \omega_c \cos\theta_0 C\,\frac{n_1}{n_0}\,E_r^{-\delta+1}\left(\tan^2\theta_0 - \frac{2}{2\delta-1}\,\frac{\omega}{\omega_c - \omega}\right), \tag{6.28}$$

where

$$C = (\delta - 1)\,\frac{E_{\min}^{\delta-1}}{4\pi\cos\theta_0}\,,$$

$$E_r = \frac{m_e}{2}\left(\frac{\omega_c - \omega}{k\cos\vartheta\cos\theta_0}\right)^2,$$

and $E_{\min}$ is the lower energy bound for high-energy particles. Formula (6.28) allows one to obtain the necessary instability condition, $\omega < \omega_c(\delta - 0.5)/(\sigma + \delta - 1.5)$, which, for instance, at $\delta = 3$ and $\sigma = 10$ gives $\omega < 0.22\omega_c$. Combining the latter inequality with formula (6.27), one obtains a threshold energy for fast electrons [184]:

$$E > E_{cr} = 5.26\xi\left(\frac{V_A}{10^8}\right)^2 \ [\mathrm{keV}]\,, \tag{6.29}$$

where $\xi = (\sigma - 1)^3/(\delta - 0.5)(\sigma + \delta - 1.5)^2$. For $\delta = 3$, $\sigma = 10$, and $V_A = 10^8$ cm s^{-1}, formula (6.29) gives $E_{cr} = 11.6$ keV. Expression (6.29) differs from that obtained by Melrose and Brown [185] by the presence of coefficient ξ. To estimate the growth rate, it is possible to use the relationship [186]

$$\frac{\gamma_w}{\omega_c} \approx \pi A \delta\,\frac{n_1}{2n_0}\,, \tag{6.30}$$

where $A \approx (\sigma - 1)^{-1}$ is the degree of anisotropy. An analysis made in Refs [184, 186] indicates that Landau damping is most significant for whistlers in solar coronal loops. It exceeds by several orders of magnitude cyclotron damping and damping pertaining to Coulomb collisions. Indeed, when whistlers are propagating along the magnetic field Landau damping is absent because the longitudinal component of the wave electric field is zero. However, this component is gained for whistlers propagating in curved magnetic fields in the loops, so that Landau damping arises with the relative decrement [187]

$$\frac{\nu_L}{\omega} = \frac{\sqrt{\pi}}{4}\,\frac{\sin^2\vartheta}{\cos\vartheta}\,\frac{\omega}{\omega_c}\,\Phi(x)\,, \quad x = \frac{\omega}{\sqrt{2}\,kV_T\cos\vartheta}\,. \tag{6.31}$$

The function $\Phi(x)$ was tabulated in Ref. [187], its values being $\Phi(x \ll 1) \approx 1/x$ and $\Phi(1) \approx 1$. Landau damping limits energy growth in excited waves, especially in flare loops with plasma temperature $\geqslant 10^7$ K, so that a regime of strong diffusion of particles in whistlers is not necessarily realized [184]. Nevertheless, for propagation in a filamented loop composed of multiple thin filaments, or in plasma compaction along the loop axis — the duct — the amplification of whistler amplitude can be significant [147, 188]. In such cases, the instability threshold with respect to density of high-energy electrons is determined by Coulomb collisions with $\nu_{coll} \approx \nu_{ei}\omega/\omega_c$, which, with account for formula (6.30) and for $\delta = 3$, $\sigma = 10$, $n_0 = 10^{11}$ cm^{-3}, $B = 100$ G, and $T = 10^7$ K, gives the fairly low threshold: $n_1/n_0 > 10^{-7}$.

In contrast to accelerated electrons, which are preferentially exciting high-frequency waves (electromagnetic waves at harmonics of the electron gyrofrequency, Langmuir waves, whistlers, and Bernstein modes), anisotropic high-energy ions in coronal loops are responsible for the generation of low-frequency ($\omega \ll \omega_i$) Alfvén waves [186, 189–191] (here, ω_i is the ion gyrofrequency). The Alfvén waves generated in the Galaxy by cosmic rays with an energy of 1–100 GeV can have a significant impact on the character of cosmic ray propagation in the interstellar gas [192]. Expressions for instability growth rates of small-scale ($\lambda \approx 2\pi v/\omega_i \leqslant 10^7$ cm) Alfvén waves for various types of anisotropy of high-energy ions are given in Ref. [190]. As an illustration, for the momentum distribution of type (6.4) the instability growth rate at ion cyclotron resonance is expressed as

$$\gamma_A = \sqrt{\frac{\pi}{8}}\,\frac{n_1}{n_0}\,\omega_i\left[\frac{\omega_i}{\omega}\,\frac{\eta}{\sqrt{1+k_\perp^4/k_0^4}} - (\eta-1)\right] y \exp\left(-\frac{y^2}{2}\right), \tag{6.32}$$

where $k_0^2 = 2(\omega/\omega_i)\,k_{||}^2$, and $y = \omega_i/k_{||}(T/m_i)^{1/2}$. In the case of propagation along the magnetic field ($k_\perp = 0$), formula (6.32) coincides with the known expression of Kennel and Petscheck [193]. Maximum value of growth rate (6.32) can be represented as

$$\gamma_A^{\max} \approx 0.4\omega\eta\beta_p\,, \tag{6.33}$$

where $\beta_p = 8\pi p_p/B^2$, and p_p is the pressure exerted by high-energy protons.

Alfvén waves refract, propagating in the curved magnetic field of a loop. As a result, similar to whistlers, they may get out of the quasiparallel propagation regime, $k_\perp > k_{||}\sqrt{\omega/\omega_i}$, and experience Landau damping, which will limit the growth of their amplitudes [189]. However, the dispersion of Alfvén waves stemming from plasma gyrotropy, $\omega/\omega_i \ll 1$, allows them, nevertheless, to preserve quasilongitudinal propagation, since the loop makes up a wave duct for Alfvén waves [190].

6.6 Fine structure of radio emission from loops

At the inception of radioastronomy, emission from solar coronal loops was attributed to broadband bursts of type IV and type V in meter and decimeter wave ranges. With growing frequency and time resolutions of radio telescopes, the true richness of the fine structure in radio emissions from the Sun and stars has become apparent. One type of fine structure in loop emissions — quasiperiodic pulsations — was considered in Sections 2 and 3. Pulsations do not exhaust, however, the full diversity of the mature fine structure pertaining to radio emission of solar and stellar flares. There are also sudden reductions, zebra patterns, fiber bursts, and spike-bursts. Clarification of the mechanisms responsible for generating the fine structure of radio emission is important for diagnosing flare plasma and understanding the origin of flares on stars.

6.6.1 Sudden reductions. Such reductions were observed against the background of broadband continuum radio emission from the Sun [194, 195] and red dwarfs AD Leo and YZ CMi [7]. The authors of this review conjectured that a rapidly drifting sudden reduction comes from streams of high-energy electrons entering the loop and filling the loss cone [196]. This leads to a breakdown of loss cone instability — the cause of continuum radio emission. To this effect, the relative concentration of a new portion of energetic particles invading the loss cone may remain relatively low, $n_2/n_1 \geqslant 0.2$ [196]. A similar idea on the origin of the sudden reductions was formulated later in Ref. [197]. This mechanism explains sudden reductions in a natural way (Fig. 18) and serves as a clear confirmation of the existence of stellar coronal loops — magnetic traps for high-energy particles.

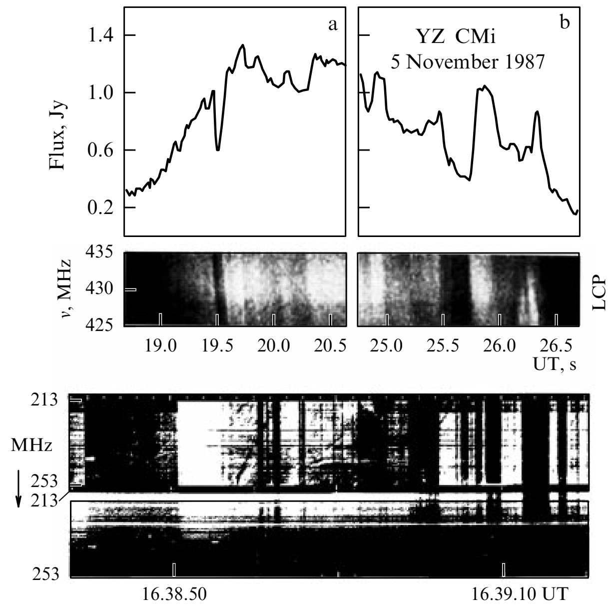

Figure 18. Dynamic spectrum (intensity of emission as a function of frequency and time) of fast drifting sudden reductions in radio emission of the star YZ Cmi (425–435 MHz) [7] and the Sun (213–253 MHz) [197].

6.6.2 Zebra pattern. Against the background of broadband radio emission of solar flares at meter and decimeter wavelengths, quasi-equidistant (in frequency) bands in emission are often observed. Their number can exceed ten (Fig. 19a, b).

The most elaborated to date is the model of the distributed source of the zebra pattern [168, 199], which assumes that the emission bands arise on fulfilling the condition of double plasma resonance in a coronal loop, $s\omega_c = (\omega_p^2 + \omega_c^2)^{1/2}$, which ensures a maximum instability growth rate for plasma waves. An example of the along-loop distribution of hybrid frequency $\omega_{uh} = (\omega_p^2 + \omega_c^2)^{1/2}$ and the harmonics $s\omega_c$ of gyrofrequency is presented in Fig. 19c, d [199]. The points of curve intersection define the regions of double plasma resonance, at which enhanced generation of longitudinal waves takes place. The interval between bands of zebra patterns, in which radio emission arises at a double plasma frequency, is expressed as

$$\Delta\omega \approx \frac{2(s-1)\,\omega_c L_B}{|(s-1)\,L_B - sL_n|} \tag{6.34}$$

and, depending on the ratio L_n/L_B, varies from $2\omega_c$ (if $L_B/L_n \gg 1$) to $2\omega_c L_B/L_n$ (if $L_B/L_n \ll 1$). Interval (6.34) decreases twofold for the fundamental tone emission.

A recent study of the instability of high-energy electrons at the double plasma resonance [200] demonstrated that the observed uncommonly large number of bands ($\geqslant 40$) in the centimeter wave range (Fig. 20b) stems from the specifics of

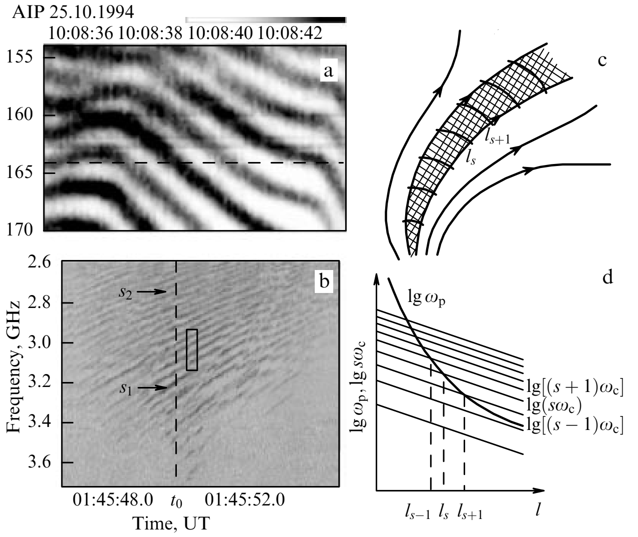

Figure 19. (a,b) Examples of dynamic spectra of the zebra pattern in solar radio emission: (a) the event on 25 October 1994 in the frequency range 155 – 170 MHz [134] (AIP — Astrophysikalisches Institut Potsdam, Germany); (b) the event on 21 April 2002 in the frequency range 2.6 – 3.6 GHz [198]; (c) the distributed source model, and (d) levels of double plasma resonance [199].

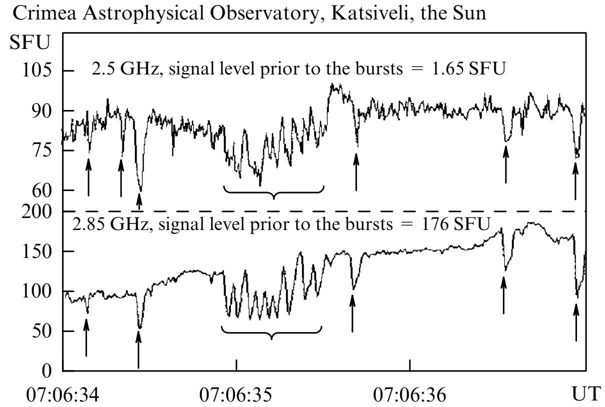

Figure 20. An example of a millisecond pulsating structure with separate sudden reductions (marked with arrows) at frequencies of 2.5 and 2.85 GHz [201]. The specifics of the event are the presence of pulsations at a lowered emission level, which stems from the reduction in the anisotropy of high-energy electrons upon injection of a new portion of particles into the coronal loop.

fast electron distribution. For a power-law distribution function with a loss cone, the number of emission bands in a zebra pattern grows with the spectral index δ, reaching 40 – 50 for $\delta = 5$. Additionally, in this study it was possible to determine plasma parameters in the source of the zebra pattern: $n_0 \approx 10^{11}$ cm^{-3}, $B \approx 40$ G, $T = (1-5) \times 10^6$ K, and $\beta \approx 0.2-1.0$ for the event on 21 April 2002 (Fig. 19b).

6.6.3 Diagnosing coronal plasma by the fine structure of radio emission. An example of diagnosing parameters of loops and energetic particles by the fine structure of radio emissions is furnished by a study of the solar event on 17 November 1991, performed in Ref. [201] on the basis of the plasma mechanism of radio emission with frequency $\omega = 2\omega_{\rm uh}$. Drifting sudden reductions at frequencies 2.5 and 2.85 GHz were observed against the background of the pulsating structure with a characteristic period $\tau_{\rm puls} \approx 60$ ms (Fig. 20), which can hardly be explained by MHD loop oscillations.

Pulsations with such a small period are interpreted as a result of nonlinear transfer of plasma waves through scattering on ions into a nonresonance domain (the decay domain) and are described in terms of the Lotka – Volterra equation [202]:

$$\frac{\mathrm{d}w}{\mathrm{d}t} = \gamma w - \zeta w w^*, \quad \frac{\mathrm{d}w^*}{\mathrm{d}t} = -\nu w^* + \zeta w w^*, \tag{6.35}$$

where w and w^* are the relative energy density of plasma waves in resonance (unstable) and nonresonance domains, $\zeta \approx \omega_{\rm p}/40$ is the coefficient of induced scattering, and $\nu = \nu_{\rm ei}$ is the damping decrement. Equation (6.35) allows periodic solutions corresponding to closed trajectories around a center type point $w_0 = \nu/\zeta$ and $w_0^* = \gamma/\zeta$. The period of pulsations around this point is given by

$$\tau_{\rm puls} = 2\pi(\gamma\nu)^{-1/2}. \tag{6.36}$$

Based on the emission frequency for the event on 17 November 1991, the plasma density was found to be $n_0 = 2.5 \times 10^{10}$ cm^{-3}, and the energy of electrons injected into the loss cone was estimated as 50 – 400 keV, based on the rate of sudden reduction frequency drift. The values of the growth rate of plasma waves, $\gamma \approx 10^{-2}\,(n_1/n_0)\,\omega_{\rm p}$, were used to infer the density of high-energy particles trapped by the loop and providing the generation of plasma waves, $n_1 \approx 2.5 \times 10^4$ cm^{-3}, and the density of particles causing disruption of loss cone instability, $n_2 > 5 \times 10^3$ cm^{-3}. Close to the instability threshold, one has $\gamma \approx \nu_{\rm ei}$, hence the kinetic temperature of plasma in the loop is found to be $T \approx 10^7$ K. The condition $\beta < 1$ translates into an estimate of the magnetic field induction in the emission source, $B > 30$ G.

6.6.4 Fiber bursts. Whistlers play an important role not only in the dynamics of energetic electrons in loops, but also in the fine structure of flare radio emission. An example is provided by drifting over frequency, narrow-band (1 – 5 MHz) bursts — the fibers, observed on the Sun over a wide range of wavelengths (from several meters to several centimeters), with a duration of 5 – 10 s. Kuijpers [203] conjectured that fibers can arise through merging whistlers with Langmuir waves ($w + l \to t$) generated in a loop by the same population of accelerated electrons. Later on, the model of fiber generation was further elaborated in works by Chernov (see the review [195]). On this route it was possible not only to explain the main features of fibers (low rate of frequency drift as compared to that of type III bursts, and bands in emission and absorption) but also to adapt this phenomenon to diagnosing the plasma of coronal loops. Indeed, based on the radiation frequency corresponding to the fundamental tone ($\approx \omega_{\rm p}$), the plasma density can be evaluated, while the frequency interval between the emission and absorption, $\Delta\omega \approx \omega_w \approx 0.1\omega_{\rm c}$, can be utilized to estimate the magnetic field induction which can independently be determined also by the velocity of fiber frequency drift. From the analysis of solar observational data a conclusion is drawn that on the level where the Langmuir frequency equals 250 MHz ($n_0 \approx 8 \times 10^8$ cm^{-3}), the magnitude of magnetic field $B \approx 5$ G (i.e., $\omega_{\rm c}/2\pi \approx 14$ MHz). For plasma frequencies of 3 and 5 GHz, the magnitudes of the magnetic field are found to be 160 and 250 G [195].

6.6.5 Spike bursts. Radio emissions from the Sun and red dwarfs frequently exhibit short-lived (several milliseconds), narrow-band ($\Delta\omega/\omega \approx 1\%$), strongly polarized bursts called spike bursts. Such bursts, which are recorded over a wide wavelength range, from several centimeters to several meters, ordinarily arise in groups comprising several thousand bursts. A detailed review of solar spike bursts can be found in Ref. [153]. A short lifetime and narrow emission band point to high brightness temperature of spike bursts, in excess of approximately $10^{14} - 10^{15}$ K. This suggests that the mechanism of spike emission is a coherent one. In this respect, two mechanisms of radio emission are discussed: ECM [153, 204], and plasma radiator [205]. The prevalence of one mechanism over the other one depends, as was shown, on the ratio ω_p/ω_c. The cyclotron maser mechanism is more efficient than the plasma one for a sufficiently strong magnetic field, $\omega_p/\omega_c \leqslant 1$.

Such a hyperfine structure of flare emissions can be interpreted as a result of fragmented energy release. Other approaches to explaining spike bursts, not linked to the fragmentation of primary flare energy release, exist as well. The fragmentation can, for instance, be intrinsic in the radio emission mechanism as such, being a consequence of the fragmented structure of the emission source. For example, in the framework of the plasma mechanism, to explain spike bursts with a duration of 100 ms in a flare on UV Ceti observed with the 100-meter Bonn radio telescope on 31 December 1991 [205], the idea of Genkin et al. [206] on the possibility of an irregular emission character in the fundamental tone of the plasma frequency was exploited. In this case, scattering of plasma waves followed by transformation into electromagnetic emission occurs on irregularities of plasma density induced by plasma turbulence proper and thermal diffusion. Stratification changes the character of the density fluctuations and, consequently, the characteristics of radio emission. Estimates made in Ref. [205] show that the characteristic existence time of such a structure (the correlation time) on the order of $(v/v_T)^2 \nu_{ei}^{-1} \approx 0.1$ s coincides with the observed duration of spike bursts on UV Ceti.

7. Conclusions

We have considered the main physical processes in coronal loops — fundamental magnetic structures in atmospheres of the Sun and flaring stars. Different representations of coronal loops have been invoked: as an equivalent electric circuit, a resonator for MHD oscillations, or a trap with magnetic mirrors. Based on these approaches, we succeeded in describing the processes of plasma heating in coronal magnetic loops, as well as flare energy release, the acceleration of charged particles, the origin of flare emission and its modulation, and also in determining the parameters of the plasma and magnetic field in coronal loops, together with the characteristics of accelerated particles. The fruitfulness of adopting solar-stellar analogies is shown, residing in the fact that multiple processes on the Sun and stars are not only phenomenologically similar, but also have a common physical nature.

Electric currents near sunspots ($\geqslant 10^{11}$ A) were first computed by Severny [35] based on measurements of magnetic fields. In this review, a method of determining electric currents in the solar atmosphere is described, which rests on representing a coronal loop as an equivalent electric circuit (Section 2). Relying on this method, it was possible to detect the accumulation of electric current energy prior to flares, current dissipation during flare, and post-flare current increase in an active region using the variability of the pulsation frequency of the radio emission from solar flares [49]. Methods of diagnosing currents in stellar coronae continue to evolve and gain in sophistication as they provide an important insight into the origin of charged particle acceleration and stellar corona heating. Recently, an approach was proposed to measure electric currents in solar and stellar coronae based on differential Faraday rotation of radio emission [207]. The efficiency of the method was illustrated by applying it to observations of radio source 3C 228, carried out with the help of the radio telescope VLA, and showing that the current amplitude in the corona of 3C 228 varied from 2.3×10^8 A to 2.5×10^9 A in various events.

As mentioned in Section 5, one of the main problems in astrophysics is explaining the large numbers of accelerated particles in flares. Indeed, the capacity of accelerating processes on the Sun is such that accelerated electrons entering the footpoints of a coronal loop can cause seismic perturbations in the solar photosphere [208]. Modern data on the acceleration of particles in solar flares, obtained with space instruments, favor a diversity of accelerating processes. They cannot be reduced to a 'standard' flare model assuming acceleration in an extended current sheet of a helmetlike structure of magnetic fields [209]. Moreover, data from the space observatories RHESSI and TRACE indicate that the acceleration of the main portion of particles happens before the formation of a cusp (a peak at the loop top) in the loop magnetic structure, i.e., prior to extended current sheet formation [210]. Currently, not only 'traditional' acceleration mechanisms are being discussed (in quasistationary electric fields, shock waves, or stochastic mechanisms), but also those specific to loop structures, for instance, the acceleration of charged particles by large-scale torsional Alfvén waves [211].

It should be noted that interpreting observational manifestations of flare energy release in loops on the Sun relies on the existence of a loop fine structure — the filaments, i.e., it is assumed that loops with a cross-section size of $10^3 - 10^4$ km are filled with thin magnetic filaments $\sim 1 - 10$ km thick. This concept furnishes an explanation for both turbulent propagation of high-energy particles and coronal loop plasma heating by diamagnetic currents. Hints at the existence of filamented loop structures follow from data gathered from solar space observatories. However, for a number of physical models of coronal loops, as shown, for example, in Sections 2 and 3, it suffices to consider the loops without their fine structures.

The role of photospheric convection in heating stellar coronae and filling them with fast particles remains less investigated. It is known that the coronae of stars belonging to late spectral classes are hotter than the solar corona, as indicated by their X-ray emission. Additionally, a large number of relativistic particles are persistently present in these coronae as implied by the brightness temperature of their 'quiet' radio emission reaching 10^9 K. It cannot be excluded that the cause of these features is the augmented velocity of photospheric convection on late type stars, since in this case, as demonstrated in Sections 2 and 5, the densities of electric currents in coronal magnetic loops are increased together with electrostatic charge separation fields in footpoints of the loops.

Considering preferentially processes in single coronal loops, which take place, for example, in single loop flares, we did not embrace all the diversity of processes pertaining to the interaction of magnetic loops and the behavior of complex loop structures observed in most solar flares. The interaction of extended magnetic loops in the coronae of rotating components of binary stars can lead to a powerful energy release. A mechanism of this type was proposed for interpreting periodic radio bursts in the binary system V733 Tau A [212]. The parameters of magnetic loops in binary stellar systems and accretion disks are most likely very different from those considered in this review. Nevertheless, the approaches proposed here can also prove useful in studying processes of energy release in a wider class of astrophysical objects, such as close binary systems, young stellar objects, or planetary systems similar to Jupiter – Io.

This work was supported by the Programs "Stars and galaxies" and "Solar activity and physical processes in the Sun – Earth system" of the Presidium of RAS, by the OFN-16 Program "Plasma processes in the solar system", RFBR grants Nos 06-02-16859a, 07-02-00157a, 08-02-00119a, and by Programs of Support for Leading Scientific Schools NSh-4485.2008.2 and NSh-6110.2008.2.

References

1. Bray R J et al. *Plasma Loops in the Solar Corona* (Cambridge: Cambridge Univ. Press, 1991)
2. Schrijver C J et al. *Solar Phys.* **187** 261 (1999)
3. Benz A O, Conway J, Güdel M *Astron. Astrophys.* **331** 596 (1998)
4. Aschwanden M J, Poland A I, Rabin D M *Annu. Rev. Astron. Astrophys.* **39** 175 (2001)
5. Sakai J-I, de Jager C *Space Sci . Rev.* **77** 1 (1996)
6. Plunkett S P et al. *Solar Phys.* **194** 371 (2000)
7. Bastian T S et al. *Astrophys. J.* **353** 265 (1990)
8. Lestrade J-F et al. *Astrophys. J.* **328** 232 (1988)
9. Kuijpers J *Lecture Notes Phys.* **444** 135 (1995)
10. Feigelson E D, Montmerle T *Annu. Rev. Astron. Astrophys.* **37** 363 (1999)
11. Priest E R *Solar Magnetohydrodynamics* (Dordrecht: D. Reidel, 1982) [Translated into Russian (Moscow: Mir, 1985)]
12. Haisch B M, in *Activity in Red-Dwarf Stars* (Eds P B Byrne, M Rodonò) (Dordrecht: D. Reidel, 1983) p. 255
13. Mullan D J et al. *Astrophys. J. Suppl.* **164** 173 (2006)
14. Schmitt J H M M et al. *Astrophys. J.* **365** 704 (1990)
15. Stepanov A V et al. *Astron. Astrophys.* **374** 1072 (2001)
16. Zaitsev V V et al. *Pis'ma Astron. Zh.* **30** 362 (2004) [*Astron. Lett.* **30** 319 (2004)]
17. Güdel M, Benz A O *Astrophys. J.* **405** L63 (1993)
18. Kan J R, Akasofu S-I, Lee L C *Solar Phys.* **84** 153 (1983)
19. Henoux J C, Somov B V *Astron. Astrophys.* **241** 613 (1991)
20. Henoux J C, Somov B V *Astron. Astrophys.* **185** 306 (1987)
21. Zajtsev V V, Khodachenko M L *Izv. Vyssh. Uchebn. Zaved. Radiofiz.* **40** 176 (1997) [*Radiophys. Quantum Electron.* **40** 114 (1997)]
22. Khodachenko M L, Zaitsev V V *Astrophys. Space Sci.* **279** 389 (2002)
23. Priest E R, in *Solar Flare Magnetohydrodynamics* (Ed. E R Priest) (New York: Gordon and Breach, 1980)
24. Zaitsev V V et al. *Astron. Zh.* **75** 455 (1998) [*Astron. Rep.* **42** 400 (1998)]
25. Khodachenko M L et al. *Astron. Astrophys.* **433** 691 (2005)
26. Alfvén H, Carlquist P *Solar Phys.* **1** 220 (1967)
27. Sen H K, White M L *Solar Phys.* **23** 146 (1972)
28. Klimchuk J A et al. *Publ. Astron. Soc. Jpn.* **44** L181 (1992)
29. Hagyard M J *Solar Phys.* **115** 107 (1988)
30. Leka K D et al. *Astrophys. J.* **411** 370 (1993)
31. Hudson H S *Solar Phys.* **113** 315 (1987)
32. Melrose D B *Astrophys. J.* **381** 306 (1991)
33. Melrose D B *Astrophys. J.* **451** 391 (1995)
34. Stenflo J O *Solar Phys.* **8** 115 (1969)
35. Severny A *Space Sci. Rev.* **3** 451 (1964)
36. Cowling T G *Magnetohydrodynamics* (London: Interscience Publ., 1957) [Translated into Russian (Moscow: IL, 1959)]
37. Zaitsev V V, Stepanov A V *Astron. Zh.* **68** 384 (1991) [*Sov. Astron.* **35** 189 (1991)]
38. Zaitsev V V, Stepanov A V *Solar Phys.* **139** 343 (1992)
39. Khodachenko M L, Zaitsev V V *Astrophys. Space. Sci.* **279** 389 (2002)
40. Kadomtsev B B, in *Nelineinye Volny* (Nonlinear Waves) (Ed. A V Gaponov-Grekhov) (Moscow: Nauka, 1978) p. 141
41. Vernazza J E, Avrett E H, Loeser R *Astrophys. J. Suppl.* **45** 635 (1981)
42. Conti P S, Underhill A B (Eds) *O Stars and Wolf-Rayet Stars* (Washington, DC: NASA, 1988)
43. Miller M C, Lamb F K, Hamilton R J *Astrophys. J. Suppl.* **90** 833 (1994)
44. Ionson J A *Astrophys. J.* **254** 318 (1982)
45. Zaitsev V V et al. *Astron. Astrophys.* **337** 887 (1998)
46. Landau L D, Lifshitz E M *Elektrodinamika Sploshnykh Sred* (Electrodynamics of Continuous Media) (Moscow: Nauka, 1982) [Translated into English (Oxford: Pergamon Press, 1984)]
47. Urpo S et al. *Solar Phys.* **154** 317 (1994)
48. Zaitsev V V et al. *Izv. Vyssh. Uchebn. Zaved. Radiofiz.* **44** 756 (2001) [*Radiophys. Quantum Electron.* **44** 697 (2001)]
49. Zaitsev V V et al. *Astron. Zh.* **80** 945 (2003) [*Astron. Rep.* **47** 873 (2003)]
50. Wigner E *Phys. Rev.* **40** 749 (1932)
51. Ville J *Cables Transmission* **2A** 61 (1948)
52. Cohen L *Proc. IEEE* **77** 941 (1989)
53. Güdel M et al. *Astron. Astrophys.* **220** L5 (1989)
54. Abada-Simon M et al. *Astron. Astrophys.* **321** 841 (1997)
55. Schlüter A, Biermann L *Z. Naturforsch. A* **5** 237 (1950)
56. Pikel'ner S B *Osnovy Kosmicheskoi Elektrodinamiki* (Moscow: Nauka, 1966); *Fundamentals of Cosmic Electrodynamics* (Washington, DC: NASA, 1964)
57. Zaitsev V V, Urpo S, Stepanov A V *Astron. Astrophys.* **357** 1105 (2000)
58. Pustil'nik L A *Astron. Zh.* **50** 1211 (1973) [*Sov. Astron.* **17** 763 (1974)]
59. Wheatland M S, Melrose D B *Solar Phys.* **159** 137 (1995)
60. Melrose D B *Astrophys. J.* **486** 521 (1997)
61. Aschwanden M J et al. *Astrophys. J.* **520** 880 (1999)
62. Kurtz D W *Solar Phys.* **220** 123 (2004)
63. Schrijver C J, Aschwanden M J, Title A *Solar Phys.* **206** 69 (2002)
64. Rosenberg H *Astron. Astrophys.* **9** 159 (1970)
65. Aschwanden M J *Solar Phys.* **111** 113 (1987)
66. Aschwanden M J, in *Turbulence, Waves, and Instabilities in the Solar Plasma* (NATO Sci. Ser. II, Vol. 124, Eds R Erdélyi et al.) (Dordrecht: Kluwer Acad. Publ., 2003)
67. Roberts B, in *Advances in Solar System Magnetohydrodynamics* (Eds E R Priest, A Hood) (Cambridge: Cambridge Univ. Press, 1991) [Translated into Russian (Moscow: Mir, 1995) p. 112]
68. Rodono M *Astron. Astrophys.* **32** 337 (1974)
69. Mullan D J, Herr R B, Bhattacharyya S *Astrophys. J.* **391** 265 (1992)
70. Mathioudakis M *Astron. Astrophys.* **403** 1101 (2003)
71. Tsiklauri D et al. *Astron. Astrophys.* **422** 351 (2004)
72. McLean D J, Sheridan K V *Solar Phys.* **32** 485 (1973)
73. Zaitsev V V, Stepanov A V *Issled. Geomagn., Aeron. Fiz. Solntsa* **37** 3 (1975)
74. Edwin P M, Roberts B *Solar Phys.* **88** 179 (1983)
75. Meerson B I, Sasorov P V, Stepanov A V *Solar Phys.* **58** 165 (1978)
76. Nakariakov V M, Melnikov V F, Reznikova V E *Astron. Astrophys.* **412** L7 (2003)
77. Nakariakov V M et al. *Science* **285** 862 (1999)
78. Uralov A M *Pis'ma Astron. Zh.* **29** 552 (2003) [*Astron. Lett.* **29** 486 (2003)]
79. Terradas J, Oliver R, Ballester J L *Astrophys. J.* **618** L149 (2005)
80. Arregui I et al. *Astron. Astrophys.* **463** 333 (2007)
81. Chen J, Schuck P W *Solar Phys.* **246** 145 (2007)
82. Mikhailovskii A B *Theory of Plasma Instabilities* Vol. 2 *Instabilities of an Inhomogeneous Plasma* (New York: Consultants Bureau, 1974); *Teoriya Plazmennykh Neustoichivostei* (Theory of Plasma Instabilities) Vol. 2 *Neustoichivosti Neodnorodnoi Plazmy* (Instabilities of an Inhomogeneous Plasma) (Moscow: Atomizdat, 1975)
83. Nakariakov V M et al. *Astron. Astrophys.* **452** 343 (2006)

84. Zaitsev V V, Stepanov A V *Pis'ma Astron. Zh.* **8** 248 (1982) [*Sov. Astron. Lett.* **8** 132 (1982)]
85. Taroyan Y et al. *Astrophys. J.* **659** L173 (2007)
86. Kislyakov A G et al. *Solar Phys.* **233** 89 (2006)
87. Zaitsev V V, Kislyakov A G *Astron. Zh.* **83** 921 (2006) [*Astron. Rep.* **50** 823 (2006)]
88. Hindman B W, Jain R *Astrophys. J.* **677** 769 (2008)
89. Stepanov A V et al. *Pis'ma Astron Zh.* **30** 530 (2004) [*Astron. Lett.* **30** 480 (2004)]
90. Zhilyaev B E et al. *Astron. Astrophys.* **364** 641 (2000)
91. Stepanov A V et al. *Pis'ma Astron. Zh.* **31** 648 (2005) [*Astron. Lett.* **31** 612 (2005)]
92. Reale F *ASP Conf. Ser.* **277** 103 (2002)
93. Mitra-Kraev U et al. *Astron. Astrophys.* **436** 1041 (2005)
94. Raassen A J J et al. *Astron. Astrophys.* **411** 509 (2003)
95. Stepanov A V, Tsap Yu T, Kopylova Yu G *Pis'ma Astron. Zh.* **32** 631 (2006) [*Astron. Lett.* **32** 569 (2006)]
96. Priest E R *ASP Conf. Ser.* **158** 321 (1999)
97. Linsky J L *Lecture Notes Phys.* **380** 452 (1991)
98. Linsky J L *ASP Conf. Ser.* **158** 401 (1999)
99. Walsh R W, Ireland J *Astron. Astrophys. Rev.* **12** 1 (2003)
100. Spicer D S, in *Mechanisms of Chromospheric and Coronal Heating* (Eds P Ulmschneider, E R Priest, R Rosner) (Berlin: Springer-Verlag, 1991) p. 547
101. Galeev A A et al. *Astrophys. J.* **243** 301 (1981)
102. Parker E N *Astrophys. J.* **330** 474 (1988)
103. Antonucci E, in *The Many Faces of the Sun: A Summary of the Results from NASA's Solar Maximum Mission* (Eds K T Strong et al.) (Berlin: Springer-Verlag, 1998) p. 331
104. Ionson J A *Astrophys. J.* **276** 357 (1984)
105. Ofman L, Davila J M, Steinolfson R S *Astrophys. J.* **421** 360 (1994)
106. Melrose D B, Dulk G A *Astrophys. J.* **282** 308 (1984)
107. Aschwanden M J et al. *Astrophys. J.* **531** 1129 (2000)
108. Reale F, Peres G *Astrophys. J.* **528** L45 (2000)
109. Zaitsev V V, Shibasaki K *Astron. Zh.* **82** 1127 (2005) [*Astron. Rep.* **49** 1009 (2005)]
110. Bakhareva N M, Zaitsev V V, Khodachenko M L *Solar Phys.* **139** 299 (1992)
111. Suzuki M, Sakai J I *Astrophys. J.* **487** 921 (1997)
112. Ryutova M et al. *Astrophys. J.* **492** 402 (1998)
113. Furusawa K, Sakai J I *Astrophys. J.* **540** 1156 (2000)
114. Gold T, Hoyle F *Mon. Not. R. Astron. Soc.* **120** 89 (1960)
115. Aschwanden M J et al. *Astrophys. J.* **515** 842 (1999)
116. Golant V E, Zhilinsky A P, Sakharov I E *Osnovy Fiziki Plasmy* (Fundamentals of Plasma Physics) (Moscow.: Atomizdat, 1977) [Translated into English (New York: Wiley, 1980)]
117. Burgess A *Astrophys. J.* **139** 766 (1964)
118. Zirin H *Astrophysics of the Sun* (Cambridge: Cambridge Univ. Press, 1988)
119. Huba J D *NRL Plasma Formulary* Vol. 54 (Washington: NRL, 1994)
120. Jain N K, Narain U *Solar Phys.* **50** 361(1976)
121. Raymond J C, Cox D P, Smith B W *Astrophys. J.* **204** 290 (1976)
122. Shibasaki K *Astrophys. J.* **557** 326 (2001)
123. Fontenla J M, Avrett E N, Loeser R *Astrophys. J.* **355** 700 (1990)
124. Litwin C, Rosner R *Astrophys. J.* **412** 375 (1993)
125. Miller J A et al. *J. Geophys. Res.* **102** 14631 (1997)
126. Emslie A G, Brown J C, Machado M E *Astrophys. J.* **246** 337 (1981)
127. Holman G D, Benka S G *Astrophys. J.* **400** L79 (1992)
128. Somov B V, Kosugi T *Astrophys. J.* **485** 859 (1997)
129. Karlický M, Kosugi T *Astron. Astrophys.* **419** 1159 (2004)
130. Alfvén H, Fälthammar C-G *Cosmical Electrodynamics: Fundamental Principles* (Oxford: Clarendon Press, 1963) [Translated into Russian (Moscow: Mir, 1967)]
131. Knoepfel H, Spong D A *Nucl. Fusion* **19** 785 (1979)
132. Hurford G J et al. *Astrophys. J.* **595** L77 (2003)
133. Litvinenko Yu E *Astrophys. J.* **462** 997 (1996)
134. Aurass H et al. *Astron. Astrophys.* **410** 1001 (2003)
135. Zaitsev V V, Zlotnik E Ya, Aurass H *Pis'ma Astron. Zh.* **31** 315 (2005) [*Astron. Lett.* **31** 285 (2005)]
136. Zlotnik E Ya et al. *Astron. Astrophys.* **410** 1011 (2003)
137. Holman G D *Astrophys. J.* **293** 584 (1985)
138. van der Oord G H *J. Astron. Astrophys.* **234** 496 (1990)
139. Fadeev A A, Kvartskhava I F, Komarov N N *Nucl. Fusion* **5** 202 (1965)
140. Hammer D A, Rostoker N *Phys. Fluids* **13** 1831 (1970)
141. Cox J L (Jr), Bennett W H *Phys. Fluids* **13** 182 (1970)
142. Lee R, Sudan R N *Phys. Fluids* **14** 1213 (1971)
143. Lovelace R V, Sudan R N *Phys. Rev. Lett.* **27** 1256 (1971)
144. Yokoyama T et al. *Astrophys. J.* **576** L87 (2002)
145. Bespalov P A, Trakhtengerts V Yu, in *Voprosy Teorii Plasmy* Iss. 10 (Ed. M A Leontovich) (Moscow: Atomizdat, 1980) p. 88 [Translated into English as *Reviews of Plasma Physics* Vol. 10 (New York: Plenum Press, 1986) p. 155]
146. Bespalov P A, Trakhtengerts V Yu *Al'fvenovskie Mazery* (Alfén Masers) (Gor'kii: Izd. IPF AN SSSR, 1986)
147. Stepanov A V et al. *Astron. Astrophys.* **465** 613 (2007)
148. Bianda M et al. *Astron. Astrophys.* **434** 1183 (2005)
149. Tsap Yu T, Stepanov A V *Pis'ma Astron Zh.* **34** 58 (2008) [*Astron. Lett.* **34** 52 (2008)]
150. Bespalov P A, Zaitsev V V, Stepanov A V *Astrophys. J.* **374** 369 (1991)
151. Dory R A, Guest G E, Harris E G *Phys. Rev. Lett.* **14** 131 (1965)
152. Mikhailovskii A B *Teoriya Plazmennykh Neustoichivostei* (Theory of Plasma Instabilities) Vol. 1 *Neustoichivosti Odnorodnoi Plazmy* (Instabilities of a Homogeneous Plasma) (Moscow: Atomizdat, 1975); *Theory of Plasma Instabilities* Vol. 1 *Instabilities of a Homogeneous Plasma* (New York: Consultants Bureau, 1974)]
153. Fleishman G D, Mel'nikov V F *Usp. Fiz. Nauk* **168** 1265 (1998) [*Phys. Usp.* **41** 1157 (1998)]
154. Kuckes A F, Sudan R N *Solar Phys.* **17** 194 (1971)
155. Stepanov A V *Pis'ma Astron. Zh.* **4** 193 (1978) [*Sov. Astron. Lett.* **4** 103 (1978)]
156. Melrose D B, Dulk G A *Astrophys. J.* **259** 844 (1982)
157. Dulk G A *Ann. Rev. Astron. Astrophys.* **23** 169 (1985)
158. Louarn P, Le Queau D, Roux A *Astron. Astrophys.* **165** 211 (1986)
159. Vlahos L *Solar Phys.* **111** 155 (1987)
160. Aschwanden M J *Astron. Astrophys. Suppl.* **85** 1141 (1990)
161. Wu C S, Lee L C *Astrophys. J.* **230** 621 (1979)
162. Hewitt R G, Melrose D B, Rönnmark K G *Austral. J. Phys.* **35** 447 (1982)
163. Melrose D B *Plasma Astrophysics: Nonthermal Processes in Diffuse Magnetized Plasmas* Vol. 2 (New York: Gordon and Breach, 1980)
164. Stepanov A V et al. *ASP Conf. Ser.* **93** 333 (1996)
165. Stepanov A V et al. *Astrophys. J.* **524** 961 (1999)
166. Vlahos L, Sharma R R, Papadopoulos K *Astrophys. J.* **275** 374 (1983)
167. Robinson P A *Astrophys. J.* **341** L99 (1989)
168. Zheleznyakov V V *Izluchenie v Astrofizicheskoi Plazme* (Radiation in Astrophysical Plasmas) (Moscow: Yanus-K, 1997) [Translated into English (Dordrecht: Kluwer, 1996)]
169. Zaitsev V V, Shaposhnikov V E, Rucker H O *Astron. Zh.* **82** 368 (2005) [*Astron. Rep.* **49** 327 (2005)]
170. Kaplan S A, Tsytovich V N *Plazmennaya Astrofizika* (Plasma Astrophysics) (Moscow: Nauka, 1972) [Translated into English (Oxford: Pergamon Press, 1973)]
171. Ginzburg V L, Zheleznyakov V V *Astron. Zh.* **35** 694 (1958) [*Sov. Astron.* **2** 653 (1958)]
172. de Jager C *Solar Phys.* **64** 135 (1979)
173. Doshek G A, NRO Rep. No. 360 (1994) p. 173
174. Zaitsev V V, Stepanov A V *Solar Phys.* **88** 297 (1983)
175. Zaitsev V V et al. *Astron. Astrophys.* **328** 390 (1997)
176. Zaitsev V V, Kupriyanova E G, Stepanov A V *Pis'ma Astron. Zh.* **26** 855 (2000) [*Astron. Lett.* **26** 736 (2000)]
177. Zheleznyakov V V, Zaitsev V V *Astron. Zh.* **47** 308 (1970) [*Sov. Astron.* **14** 250 (1970)]
178. Kupriyanova E G, Stepanov A V *Izv. Vyssh. Uchebn. Zaved. Radiofizika* **44** 788 (2001) [*Radiophys. Quantum Electron.* **44** 726 (2001)]
179. Stepanov A V *Izv. Vyssh. Uchebn. Zaved. Radiofizika* **13** 1342 (1970) [*Radiophys. Quantum Electron.* **13** 1034 (1970)]
180. Ginzburg V L, Zaitsev V V *Nature* **222** 230 (1969)
181. Ginzburg V L, Zheleznyakov V V, Zaitsev V V *Usp. Fiz. Nauk* **98** 201 (1969); *Astrophys. Space Sci.* **4** 464 (1969)
182. Trigilio C et al. *Astron. Astrophys.* **362** 281 (2000)
183. Suzuki I, in *Proc. Hinitory Symp. on Solar Flares, Tokyo* (1982) p. 92

184. Stepanov A V, Tsap Y T *Solar Phys.* **211** 135 (2002)
185. Melrose D B, Brown J C *Mon. Not. R. Astron. Soc.* **176** 15 (1976)
186. Wentzel D G *Astrophys. J.* **208** 595 (1976)
187. Akhiezer A I et al. *Elektrodinamika Plazmy* (Plasma Electrodynamics) (Ed. A I Akhiezer) (Moscow: Nauka, 1974)
188. Mal'tseva O A, Chernov G P *Kinem. Fiz. Nebesnykh Tel* **5** (12) 32 (1989)
189. Meerson B I, Rogachevskii I V *Solar Phys.* **87** 337 (1983)
190. Mazur V A, Stepanov A V *Astron. Astrophys.* **139** 467 (1984)
191. Tamres D H, Melrose D B, Canfield R C *Astrophys. J.* **342** 576 (1989)
192. Wentzel D G *Annu. Rev. Astron. Astrophys.* **12** 71 (1974)
193. Kennel C F, Petscheck H E *J. Geophys. Res.* **71** 1 (1966)
194. Slottje C *Astron. Astrophys.* **32** 107 (1974)
195. Chernov G P *Space Sci. Rev.* **127** 195 (2006)
196. Zaitsev V V, Stepanov A V *Astron. Astrophys.* **45** 135 (1975)
197. Benz A O, Kuijpers J *Solar Phys.* **46** 275 (1976)
198. Fu Q et al. *Solar Phys.* **222** 167 (2004)
199. Zheleznyakov V V, Zlotnik E Ya *Solar Phys.* **44** 447 (1975)
200. Kuznetsov A A, Tsap Yu T *Solar Phys.* **241** 127 (2007)
201. Fleishman G D, Stepanov A V, Yurovsky Yu F *Space Sci. Rev.* **68** 205 (1994)
202. Zaitsev V V *Solar Phys.* **20** 95 (1971)
203. Kuijpers J *Solar Phys.* **44** 173 (1975)
204. Fleishman G D *Solar Phys.* **153** 367 (1994)
205. Stepanov A V et al. *Astron. Astrophys.* **299** 739 (1995)
206. Genkin L G, Erukhimov L M, Levin B N *Solar Phys.* **128** 423 (1990)
207. Spangler S R *Astrophys. J.* **670** 841 (2007)
208. Kosovichev A G *Astrophys. J.* **670** L65 (2007)
209. Aschwanden M J *Asian J. Phys.* (2008) (in press)
210. Sui L, Holman G D, Dennis B R *Adv. Space Res.* **41** 976 (2008)
211. Fletcher L, Hudson H S *Astrophys. J.* **675** 1645 (2008)
212. Massi M et al. *Astron. Astrophys.* **480** 489 (2008)